Theoretical studies on health and diseases that originate from the responses to external factors

原, 朱音

Theoretical studies on health and diseases that originate from the responses to external factors

Akane Hara

Submitted to the faculty of the Graduate School
in partial fulfillment of the requirements
for the degree
Doctor of Philosophy
in Science
Kyushu University
January 2021

Preface

Human body system maintains homeostasis while responding to various external stimuli such as pathogen infection, food intakes and day-night cycles. The dysregulation of the homeostasis may cause some disorders. For example, immune system is tolerant of harmless substances such as tree pollens, food and self-antigens. However, once the tolerance breaks down, the undesirable immune responses are induced, which are observed as allergy and autoimmunity. In the modern society, the daily activity patterns frequently change due to shift work, which may cause some chronic diseases related to circadian rhythm, such as metabolic syndromes (Wang et al., 2011).

To understand the mechanism of diseases development, it is necessary to examine the complicated interaction among the internal body systems. For example, some studies suggested that the several systems in the body such as immune system, nervous system, and intestinal microbiome have close association (Clarke et al., 2013; Sampson et al., 2016). The individual differences in the responses to external stimuli also makes it difficult to understand the disease development. Some people show severe allergic symptoms to a certain food and tree pollen, but others do not. The concepts of personalized and precision medicine are expected to provide accurate treatment methods by focusing on the individual conditions (Ho et al., 2020).

Mathematical modeling is a powerful tool to understand the complicated mechanisms of disease development. By developing mathematical models, we can integrate the findings in the fields of molecular biology and medicine. Modeling is also helpful to predict the time course of disease development in the conditions which are difficult to reproduce in animal experiments. The field of theoretical immunology has led to the discovery of the mechanism of immune responses by mathematical modeling. The required diversity of antigen receptors for regulation of immune responses was explained by mathematical modeling (De Boer and Perelson, 1993). De Boer and Perelson (1998) developed the mathematical model to describe the T cell dynamics in HIV infection. In terms of regulation of immune responses, regulatory T cells play a role as one of the important mechanisms to suppress the exaggerated immune responses (Sakaguchi et al., 2008). The importance of having localized suppression of regulatory T cells to realize

proper suppressive function and the optimal number of regulatory T cells were discussed in the previous theoretical studies (Saeki and Iwasa 2009; Saeki and Iwasa 2010).

This thesis proposed simple mathematical models to describe the mechanism of dynamic disease development. I aimed to build a theory to unravel the complicated interaction among the body internal systems in response to the external stimuli and to develop a framework for prediction of the dynamic disease development. I firstly discussed the mechanism of some immune disorders such as allergy and autoimmunity as results of responses to exposure to external substances and organisms, and secondly the relationship between meal timings and nutrient metabolism. I summarize the contents for each chapter as follows.

Chapter 1: When is allergen immunotherapy effective?

Allergen immunotherapy is a treatment method to suppress allergic symptoms by taking allergens little by little, which mechanism has not been fully understood (Pfaar et al., 2019). Moreover, the treatment takes several years, and its effect differ among the individuals, which may be harmful for some patients because of allergens used during the treatment. Thus, I developed the mathematical model describing the mechanism of the allergen immunotherapy to predict the condition of patients and treatment schedule for the successful therapy. In the model, the differentiation processes of two types of T cells: T helper cells, the trigger of allergy, and regulatory T cells, the moderator of exaggerated immune responses. I found that the treatment method would be successful in the patients with small decay rate and strong suppression effect of regulatory T cells. I also found that the gradually increasing dose amount would suppress the allergy risk.

Chapter 2: Coupled dynamics of intestinal microbiome and immune system

The intestinal microbiome and host immune have close association. Some microbes have been revealed to induce regulatory T cells by producing some metabolites (Furusawa et al., 2013). Thus, I aimed to find the novel treatment methods for allergy through intervention to intestinal microbiome. The mathematical model described the interaction among the microbes inducing regulatory T cells. There are two equilibria representing the “dysbiosis” state with small number of microbes accompanied by high

allergy risks and “non-dysbiosis” state with large number of microbes accompanied by low allergy risks. I derived a formula to make the “non-dysbiosis” equilibrium stable, which may suggest a treatment strategy of allergy by intervention on microbiome. I found that enhancing growth rate, carrying capacity of microbes and reducing the attack rate of T helper cells on microbes were useful to reduce allergy risks.

Chapter 3: Autoimmune diseases initiated by pathogen infection

Molecular mimicry has been assumed to be one of the triggers of autoimmunity development, in which the pathogens mimic the host protein to escape immune responses (Albert and Inman, 1999). I made a scenario in which the viruses mimicking host protein were eliminated by the immune system and the responses to self-antigens caused by cross immunity were remained after the infection. I developed a mathematical model describing dynamics of viruses and immune cells specific to either self-antigens or viruses. I considered the effect of cross immunity in the three steps of immune responses and found that the cross immunity on (1) removal of viruses and (2) activation of immune cells decreased the remained immune responses after the infection by eliminating viruses effectively, but (3) immune response downstream of T cell dynamics enhanced the immune responses after the infection.

Chapter 4: Why meals during resting time cause fat accumulation in mammals: Mathematical modeling of circadian control on glucose metabolism.

Irregular meal timings due to the shift work have been revealed to cause malfunction of metabolism such as obesity and diabetes (Shan et al., 2018; Wang et al., 2011). To understand the relationship between the timings of food intakes and glucose metabolism, I developed the mathematical model describing the glucose allocation process into glycogen and triglycerides. I considered the two schedules: food intakes during active phases or resting phases. I calculated the dynamics of glucose, glycogen, triglycerides and energy produced from glucose and fat. To quantify the homeostasis on the nutrient metabolism, I formulated two risks in metabolism: energy depletion and high blood glucose. I calculated the dynamics of the two risks changing the peak phases of glycogen and fat production. As a result, when the minimum risks of energy

depletion were achieved, more fat was accumulated from food intake during the resting phases than active phases. Thus, more fat accumulation from food intakes during the resting phases can be explained as the byproduct of preventing the energy depletion.

References

Albert, L. J., & Inman, R. D. (1999). Molecular Mimicry and Autoimmunity. *New England Journal of Medicine*, *341*(27), 2068–2074. https://doi.org/10.1056/NEJM199912303412707

Clarke, G., Grenham, S., Scully, P., Fitzgerald, P., Moloney, R. D., Shanahan, F., Dinan, T. G., & Cryan, J. F. (2013). The microbiome-gut-brain axis during early life regulates the hippocampal serotonergic system in a sex-dependent manner. *Molecular Psychiatry*, *18*(6), 666–673. https://doi.org/10.1038/mp.2012.77

De Boer, R. J., & Perelson, A. S. (1993). How diverse should the immune system be? *Proceedings. Biological Sciences*, *252*(1335), 171–175. https://doi.org/10.1098/rspb.1993.0062

De Boer, R. J., & Perelson, A. S. (1998). Target cell limited and immune control models of HIV infection: A comparison. *Journal of Theoretical Biology*, *190*(3), 201–214. https://doi.org/10.1006/jtbi.1997.0548

Furusawa, Y., Obata, Y., Fukuda, S., Endo, T. A., Nakato, G., Takahashi, D., Nakanishi, Y., Uetake, C., Kato, K., Kato, T., Takahashi, M., Fukuda, N. N., Murakami, S., Miyauchi, E., Hino, S., Atarashi, K., Onawa, S., Fujimura, Y., Lockett, T., … Ohno, H. (2013). Commensal microbe-derived butyrate induces the differentiation of colonic regulatory T cells. *Nature*, *504*(7480), 446–450. https://doi.org/10.1038/nature12721

Ho, D., Quake, S. R., McCabe, E. R. B., Chng, W. J., Chow, E. K., Ding, X., Gelb, B. D., Ginsburg, G. S., Hassenstab, J., Ho, C. M., Mobley, W. C., Nolan, G. P., Rosen, S. T., Tan, P., Yen, Y., & Zarrinpar, A. (2020). Enabling Technologies for Personalized and Precision Medicine. *Trends in Biotechnology*, *38*(5), 497–518. https://doi.org/10.1016/j.tibtech.2019.12.021

Pfaar, O., Agache, I., de Blay, F., Bonini, S., Chaker, A. M., Durham, S. R., Gawlik, R., Hellings, P. W., Jutel, M., Kleine-Tebbe, J., Klimek, L., Kopp, M. V., Nandy, A., Rabin, R. L., van Ree, R., Renz, H., Roberts, G., Salapatek, A. M., Schmidt-Weber, C. B., … Akdis, C. A. (2019). Perspectives in allergen immunotherapy: 2019 and beyond. *Allergy: European Journal of Allergy and Clinical Immunology*, *74*(S108), 3–25. https://doi.org/10.1111/all.14077

Saeki, K., & Iwasa, Y. (2009). Advantage of having regulatory T cells requires localized suppression of immune reactions. *Journal of Theoretical Biology*, *260*(3), 392–401. https://doi.org/10.1016/j.jtbi.2009.06.020

Saeki, K., & Iwasa, Y. (2010). Optimal number of regulatory T cells. *Journal of Theoretical Biology*, *263*(2), 210–218. https://doi.org/10.1016/j.jtbi.2009.11.012

Sakaguchi, S., Yamaguchi, T., Nomura, T., & Ono, M. (2008). Regulatory T Cells and Immune Tolerance. *Cell*, *133*(5), 775–787. https://doi.org/10.1016/j.cell.2008.05.009

Sampson, T. R., Debelius, J. W., Thron, T., Janssen, S., Shastri, G. G., Ilhan, Z. E., Challis, C., Schretter, C. E., Rocha, S., Gradinaru, V., Chesselet, M. F., Keshavarzian, A., Shannon, K. M., Krajmalnik-Brown, R., Wittung-Stafshede, P., Knight, R., & Mazmanian, S. K. (2016). Gut Microbiota Regulate Motor Deficits and Neuroinflammation in a Model of Parkinson's Disease. *Cell*, *167*(6), 1469-1480.e12. https://doi.org/10.1016/j.cell.2016.11.018

Shan, Z., Li, Y., Zong, G., Guo, Y., Li, J., Manson, J. E., Hu, F. B., Willett, W. C., Schernhammer, E. S., & Bhupathiraju, S. N. (2018). Rotating night shift work and adherence to unhealthy lifestyle in predicting risk of type 2 diabetes: Results from two large US cohorts of female nurses. *BMJ (Online)*, *363*, 17–19. https://doi.org/10.1136/bmj.k4641

Wang, X. S., Armstrong, M. E. G., Cairns, B. J., Key, T. J., & Travis, R. C. (2011). Shift work and chronic disease: The epidemiological evidence. *Occupational Medicine*, *61*(2), 78–89. https://doi.org/10.1093/occmed/kqr001

Acknowledgments

I would like to thank my supervisor Prof. Akiko Satake, for her great support on my research activities. I also thank her for giving me an opportunity to work on chronobiology. I am grateful to Prof. Yoh Iwasa, for his constant encouragement throughout my PhD program. He invited me to the world of mathematical biology when I was an undergraduate. I appreciate for helpful comments on my work given by Prof. Rob de Boer and all the members of Theoretical Biology and Bioinformatics Group in Utrecht University. During my stay in their laboratory, I was very motivated to continue my modeling research on theoretical immunology. I am thankful to the members and alumni of Mathematical Biology Laboratory at Kyushu University, for stimulating discussion from the points of view of their various interests. Especially, I am grateful to professors Shingo Iwami, Eriko Sasaki, Hiroshi Haeno, Joung-hun Lee and Koji Noshita for their advice on my research and also on my future carrier. I would like to thank the following people for their helpful comments and fruitful discussion on my study: Catherine Beauchemin, Camila Caldana, Benny Chain, Shinji Fukuda, Shingo Gibo, Natsuko Hamamura, Hiroshi Ito, Yoshiki Koizumi, Gen Kurosawa, Laura Liao, Shinji Nakaoka, Takayuki Ohara, Akira Sasaki, Koichi Saeki, Motohide Seki, and Kosuke Teshima. I am thankful to Prof. Masato Tsujii, Prof. Mitsuhiro Nakao, and Ms. Nami Masuda, who taught me the beauty of mathematics when I was a high school student and encouraged me to pursue my PhD until today. I thank to my family and friends; I could not have continued my research without their support. Finally, this work was financially supported by a Research Fellowship for Young Scientists (DC1) by Japan Society for the Promotion of Science.

Contents

Chapter 1 When is allergen immunotherapy effective?

The study in this chapter, done in collaboration with Dr. Yoh Iwasa, was published in Journal of Theoretical Biology 425: 23–42 in 2017.

Abstract

Allergen immunotherapy is used to treat allergic symptoms such as rhinitis and itchy eyes in Japanese patients with cedar pollen allergy (JCPA). Administration of small amounts of pollen over several years may suppress severe allergic symptoms when these patients are later exposed to large amounts of pollen in the environment. Herein, we developed a simple mathematical model to identify conditions in which allergen immunotherapy is effective. We considered the dynamics of type 2 T helper cells (Th2) and regulatory T cells (Treg), both of which differentiate from naive T cells. Therapy was considered successful under the following three conditions: (1) Without therapy patients develop allergic symptoms upon exposure to environmental pollen, (2) with therapy patients do not develop symptoms upon exposure, and (3) patients do not develop allergic symptoms to the therapy itself. We defined scores for therapeutic success and identified ranges of parameters in which allergen immunotherapy is likely to be successful. Treg cells have a longer lifespan than Th2 cells, allowing accumulation over many years. In accordance, therapy with linear dose increases (rather than constant doses) reduced the risk of allergies to the therapy itself, and led to stronger accumulation of resistance to pollen exposure.
key words: regulatory T cells; Th2 cells; dynamical model.

1. Introduction

Allergies are undesirable reactions that are caused by hypersensitivity to harmless materials, such as wheat, mites, and tree pollen. From February to March, many people in Japan suffer from inflammation of the eyes and nose due to Japanese cedar pollen allergies. Runny noses and itchy eyes cause physical and mental suffering and degrade quality of life (Shiomori et al.2007). To control allergic symptoms, otolaryngologists prescribe anti-allergic drugs according to the severity of symptoms (Yamada et al. 2014). However, anti-allergic drugs do not provide a permanent cure, and patients must visit the doctor every year.

Recently, *allergen immunotherapy* was introduced for the treatment of Japanese cedar pollen allergy (JCPA). During therapy, patients take an allergen (pollen extract) in multiple small doses for months, and subsequent allergic reactions to pollen-rich air are suppressed. This therapeutic approach was first documented in 1911 in a study of immunotherapy for allergy to gramineous plants using subcutaneous injections (Noon 1911 and Freeman 1911) and is now known as subcutaneous immunotherapy (SCIT). More recently, sublingual immunotherapy (SLIT) was developed to improve safety. In this approach, patients take drops of pollen extract via the sublingual route (Moingeon and Mascarell 2012). The effects of SLIT for JCPA were subsequently investigated and the therapy was shown to be effective for reducing symptoms (Okubo and Gotoh 2009). Moreover, Pfaar *et al*. (2015) recently discussed mechanisms of allergen immunotherapy and proposed corresponding therapeutic guidelines.

Allergy has been described in terms of the following chain of events: Firstly, antigen-presenting cells (APCs) receive antigens such as pollen and process these into peptides. APCs then present peptides to naive T cells (Th0 cells), which then differentiate into type 2 T helper cells (Th2 cells) in the presence of interleukin-4 (IL-4). Th2 cells then activate B cells by producing IL-4 and activated B cells produce IgE antibodies that bind receptors on the surfaces of mast cells and are cross-linked with each other via the antigen. Subsequently, mast cells degranulate and release molecules such as histamine, which induce inflammation and allergic symptoms.

Regulatory T cells (Treg cells) suppress exaggerated allergic responses (Sakaguchi et al. 2013). An experimental study suggested that after grass pollen

immunotherapy, the number of Treg cells increased and play an important role in suppressing recruitment and activation of Th2 cells (Radulovic et al. 2008). Immunotherapy using cow milk protein as allergen also induces Treg cells in mice (Smaldini et al. 2015). Moreover, observations of natural immunotherapy indicate that exposure to farm environments may prevent allergy and induction of Treg cells (Lluis et al. 2014), and maternal exposures have also been shown to be effective (Schaub et al. 2009). These examples have been explained using the hygiene hypothesis, which suggests that microbiome exposures prevent allergic symptoms and asthma, and has been investigated as a microbiome-based therapeutic approach (Liu, 2015).

Mechanisms of immune suppression by natural and allergen immunotherapy remain poorly understood, and several alternative theories have been proposed (Vignali et al. 2008). For example, Taylor *et al*. (2006) suggested that Treg cell cytokines such as IL-10, TGF-β, and various surface molecules play multiple roles in the suppression of immune responses. In addition, Wing *et al*. (2008) suggested that Treg cells suppress immune responses by preventing APCs from activating Th0 cells.

We considered two types of T cells: induced regulatory T cells (iTreg cells) and naturally occurring regulatory T cells (nTreg cells). Similar to Th2 cells, iTreg cells differentiate from Th0 cells in peripheral tissues. In contrast, nTreg cells are produced in the thymus via a different route. Accumulation of iTreg cells has been demonstrated in peripheral tissues, and corresponds with regulatory memories of localized areas of the human body (Burzyn et al. 2013).

Fishman and Segel (1996) developed the first mathematical model of allergen immunotherapy and emphasized the roles of cross regulation between Th1 and Th2 cells. The balance of Th1 and Th2 cells was also considered in models of melanoma therapy (Kogan et al. 2013), and for asthma development depending on quantities of air dust particles (Kim et al. 2013). Moreover, Gross *et al*. (2011) developed a mathematical model for allergen immunotherapy and included Th1/Th2 balance and the effects of Treg cells. In this study, allergen immunotherapy was administered in two phases. In the first phase, patients began by taking small amounts of pollen and gradually increased doses to a certain point, and in the latter phase patients took constant doses of pollen (maintenance phase). These investigators concluded that the

maintenance phase should be started as early as possible to facilitate growth of Treg cell populations and suppress Th2 cells.

In the present study, we investigated a simple dynamic model of Th2 and Treg cells. We adopted the number of Th2 cells as an index for the severity of allergic symptoms and expressed the dynamics of Th2 and Treg cell numbers using a system of ordinary differential equations. Subsequently, we defined explicit scores for successful therapy, and identified conditions in which therapy is likely to be successful. We conclude that, for this therapy to be effective, the longevity of Treg cells must be greater than that of Th2 cells so that Treg cells can accumulate and contribute to suppression of reactions to environmental pollen exposures. We also compared the efficacies of various treatment schedules.

2. Model

To examine suppressive effects of regulatory T cells in allergen immunotherapy, we used the model illustrated in Fig. 1. This model describes the stage in which naive T cells are differentiated into Th2s and Tregs. Following presentation of antigens such as pollen extracts to naive T cells (Th0) by antigen-presenting cells (APC), Th0 cells differentiate into regulatory T cells (Treg) or helper T cells (Th2) depending on the chemical environment (Luckheeram et al. 2012). Because Th2 cells trigger allergic reactions (Luckheeram et al. 2012), we assume that the magnitude of allergic symptoms is represented by Th2 cell numbers. We assumed that patients show allergic symptoms when the value of Th2 cell numbers (H) exceeds θ, which is the threshold for revealing symptoms. In contrast with Th2 cells, Treg cells suppress allergic responses by preventing activation of naive T cells and differentiation into Th2 cells (Wing et al. 2008).

We considered a therapy phase of two or three years, in which patients take drops of pollen extract, and a subsequent exposure phase, in which patients are exposed to large doses of pollen over several months. For simplicity, we did not consider exposure to environmental pollen during the therapy phase.

We denoted Treg cells numbers as R and Th2 cell numbers as H, and calculated dynamics using the following differential equations:

$$\frac{dR}{dt} = b \cdot P(t) \cdot \ (1 - c) - d_r \cdot R, \tag{1a}$$

$$\frac{dH}{dt} = \frac{b \cdot \ P(t) \cdot c}{1 + m \ (R + n)} - d_h \cdot H. \tag{1b}$$

The pollen dose $P(t)$ was calculated as follows:

$$P(t) = \begin{cases} a & for\ t < T \text{ (during therapy phase)} \\ A & for\ t > T \text{ (during exposure phase)} \end{cases}. \tag{2}$$

During a therapy phase of duration T, patients take small amounts of pollen every day, and the intensity of pollen dose is represented by a in Eq. (2). Subsequently, patients are exposed to large doses of environment pollen (exposure phase) and the pollen doses in this phase are denoted by A, as in Eq. (2).

In Eqs. (1a) and (1b), the first term of the right-hand side represents the supply of Treg or Th2 cells by differentiation from naive T cells. Pollen grains are given to the patient at rate $P(t)$, and stimulate mature T cell production at a rate that is proportional to the amount of pollen received $P(t)$, with proportionality coefficient b. Among newly differentiated T cells that are reactive to pollen antigens, fraction c ($0 < c < 1$) differentiate into helper T cells, and the remaining fraction $1 - c$ differentiate into regulatory T cells. In addition, Treg cells suppress differentiation into Th2 cells, as indicated by the denominator of the first term in the right-hand side of Eq. (2). The coefficient m is the strength of this effect, and we assume that nTreg cells are produced separately regardless of naive T cell differentiation, and their abundance is denoted by n.

The second term of Eq. (1) represents the decay of T cells. Specifically, d_r and d_h denote decay rates of Treg and Th2 cells, respectively. We assume that "memory Treg cells", which live long life in local nonlymphoid tissue (Burzyn et al. 2013), have the role of suppressing immunoreaction. Therefore, we set the decay rates to satisfy $d_r < d_h$, allowing relative accumulation of Treg cells in the local tissue.

Equations (1) and (2) have the following ten parameters θ, a, A, b, c, d_h, d_r, m, n, and T, and each of these parameters influence the success of therapy. Accordingly, we examined the model using simulations with 3^{10} combinations of parameters in which each parameter takes three different levels (Table 1). For each set of parameters, we considered conditions with therapy and without therapy. In Fig. 2, we illustrate four cases that differed in the presence of symptoms, and in therapy and exposure phases. Fig. 2A shows a case of successful therapy and Fig. 2B shows a case in which the therapy failed to suppress symptoms of pollen exposure. In Fig. 2C, the patient showed no symptoms without therapy, and in Fig. 2D the patient experienced allergic symptoms during the therapy phase.

2.1 *Therapeutic success scores*

To determine conditions in which allergen immunotherapy is effective, we evaluated the influences of various parameters on therapeutic successes and defined corresponding scores that can be used to identify patients in whom therapy would be effective. Therapy was regarded as successful when (1) without therapy the patient developed allergic symptoms upon exposure to the environmental pollen, (2) with therapy the patient did not develop symptoms upon exposure, and (3) the patient did not develop allergic symptoms due to the therapy itself. Scores were then calculated as the sum of the three components, and are expressed in terms of three peaks of $H(t)$ curves. Let $H_o(t)$ be the number of Th2 cells without therapy and $H_w(t)$ be the number of Th2 cells with therapy.

For example, $\max_{t>T} H_o(t)$ is the peak $H(t)$ without therapy. If this is larger than the threshold θ, the difference $(\max_{t>T} H_o(t) - \theta)$ indicates the severity of allergic symptoms that the patient experiences without therapy and $H(t)$ peaks that are smaller than θ indicate absence of detectable symptoms. Therefore, $(\max_{t>T} H_o(t) - \theta)$ should be positive for patients who have allergic symptoms.

The expression $\max_{t<T} H_w(t)$ is the $H(t)$ peak in the therapy and the expression $\max_{t>T} H_w(t)$ is the peak pollen exposure after the therapy. Therapy was regarded as failed if pollen administration itself caused allergic symptoms ($\max_{t<T} H_w(t) > \theta$) and if allergic symptoms to environmental pollen were not suppressed by the therapy ($\max_{t>T} H_w(t) > \theta$). For successful therapy, $\max_{t<T} H_w(t) < \theta$ and $\max_{t>T} H_w(t) < \theta$, and the differences between sides in these inequalities were regarded as margins of safety during or after therapy.

We introduced symbols for differences between peaks of $H(t)$ and the threshold θ, as follows:

$$S_0\ (relative\ peak\ height\ without\ therapy) = \max_{t>T} H_0(t) - \theta, \qquad (3a)$$

$$S_{\mathrm{T}}\ (relative\ peak\ height\ in\ Therapy) = \max_{t<T} H_w(t) - \theta\,, \qquad (3b)$$

$$S_{\mathrm{E}}\ (relative\ peak\ height\ in\ Exposure) = \max_{t>T} H_w(t) - \theta. \qquad (3c)$$

If these quantities are positive, allergic symptoms appear in respective situations, and magnitudes of symptoms are expected to increase with these quantities, as shown in Figs. 2A, 2B, and 2D. Therapy is successful if $S_0 > 0$, $S_{\mathrm{T}} \leq 0$, and $S_{\mathrm{E}} \leq 0$. Under these circumstances, a possible measure of therapeutic success is the severity of symptoms S_o.

To combine three aspects of therapeutic success, we used a simple sum of the three quantities, each indicating one requirement as follows:

$$score = \alpha + \beta + \gamma. \qquad (4)$$

The first component α is related to the symptoms experienced by a patient without therapy and is calculated from S_o. We consider symptoms as not detectable if $S_o \leq 0$,

and define the following quantity as the first component of the score using $[x]_+ = x\ if\ x \geq 0, [x]_+ = 0\ if\ x < 0$:

$$\alpha = ([S_0]_+)^{0.1}, \tag{5a}$$

where S_0 is the relative peak height without therapy (Eq. 3a). We adopted a power function of S_0 with a small positive power of 0.1 to avoid regarding runs with very large S_0 as successful cases when the other requirements were violated. Hence, using a small positive power, the impact of very large S_o is mitigated and the score becomes high only when all three conditions are satisfied.

If $S_\mathrm{T} > 0$ or $S_\mathrm{E} > 0$ or both hold, the case is not successful. Because evaluations of these cases are desirable, we introduce penalty terms. Specifically, if $S_T > 0$, symptoms appear during therapy and are greater if S_T is larger. Hence, we introduce a penalty term of the following value:

$$\beta = -([S_\mathrm{T}]_+)^{0.1}. \tag{5b}$$

Similarly, we introduced another penalty term when symptoms remained even under therapy ($S_\mathrm{E} > 0$) using the following function:

$$\gamma = -([S_\mathrm{E}]_+)^{0.1}\ . \tag{5c}$$

Eqs. (5b) and (5c) are second and the third components of the score given in Eq. (4).

In further computations, we examined combinations of parameters that are likely to be associated with successful therapy. Ten parameters were examined with three (high, intermediate, and low) values each, as listed in Table 1 (see also caption to the table). Scores for each run of 3^{10} parameter sets were calculated, and parameter sets that achieved scores in the top 10% of all runs were regarded as successful cases, although we do not have clear reason of why we choose 10% instead of other percentage for identifying runs achieving a high score.

3. Parameter sensitivity

Parameter sensitivity of the model was examined for each of the ten parameters using high, intermediate, and low values for the likelihood of successful therapy, and the influence of each parameter on therapeutic success was investigated. Our aim in the current study is to know the condition in which all of the three criteria of therapy success are satisfied ($S_0 > 0$, $S_T \leq 0$, and $S_E \leq 0$), using "score". In addition, parameter sensitivity of S_0, S_T and S_E are also important to know the effect of parameters on therapy results. First, we investigated parameter dependence of S_0, S_T and S_E and then we discuss parameter sensitivity of each parameter using "score".

We set parameter range in order to illustrate a range of the model's behavior as in Fig. 2; therapy success (Fig. 2A), having symptom after therapy (Fig. 2B), having no symptoms even without therapy (Fig. 2C) and having symptom in therapy (Fig. 2D). Since our main purpose of the current study is to develop the simplest mathematical model of allergen immunotherapy and to elucidate the logical basis of the system, rather than to develop realistic model, identifying the realistic parameter range should be done in future development of this paper.

In these computations, as shown in Table 1, θ = 10, 50 and 90 were set for threshold of the number of Th2 cells for having symptoms. a = 0.1, 0.5 and 0.9 were set as the intensity of pollen intake in the therapy phase and we set A = 10, 50 and 90 (i.e., 100 times a = 0.1, 0.5 and 0.9) as the environmental pollen exposure in the exposure phase. Numbers of naïve T cells produced in response to a unit of pollen were set as b = 10, 100, and 1000 for low, intermediate, and high, respectively. The fraction of naïve T cells that differentiated into Th2 cells was denoted by c, and c = 0.5 indicates that half of all naïve T cells differentiate into Th2 or Treg cells. Subsequently, c = 0.7 and c = 0.9 were set as intermediate and high values of c. Mortality of Th2 cells was denoted by d_h and d_h = 1.0 for the intermediate value and d_h = 0.5 and 1.5 for low and high mortality rates, respectively. We assumed that the turnover of Treg cells is much slower than that of Th2 cells. Hence, d_r was considered much smaller than d_h and the three values were set to d_r = 0.001, 0.01, and 0.1. Correspondingly, the strength of suppression m was set to 0.001, 0.01, and 0.1, and numbers of nTreg cells n were set to 2, 20, and 200. If both m and n are large, all runs will indicate that cases have no symptoms even without

therapy (Fig. 2C). However, if both *m* and *n* are small, cases will have strong symptoms during or after therapy (Fig. 2B and 2D), leading to failure of therapy. *T* is the duration of the therapy phase in days, and was set to $T = 900$ as the longest length (about two and a half years), and shorter phases were set to $T = 100$ and 500.

We chose these ranges of parameters (in Table 1) for the model to accommodate all four kinds of cases, as illustrated in Figs. 2A, 2B, 2C, and 2D. For example, although *c* can be smaller than 0.5 within the range of $0 < c < 1$, we chose $c = 0.5$, 0.7 and 0.9. With *c* smaller than 0.5, the cases having symptoms during or after therapy is less likely to appear and then we start with c = 0.5.

3.1 *Parameter sensitivity of relative peak height without therapy, in therapy and after therapy* ($S_0, S_\mathrm{T}, S_\mathrm{E}$)

We investigated the parameter sensitivity of three relative peak heights, S_o, S_T and S_E. The results are explained in detail in Appendix A. Larger *b* and *c* and smaller d_h, *m* and *n* are more likely to achieve a peak of $H(t)$. These are situations in which the patients are likely to have symptoms.

3.2 *Parameter sensitivity of the score*

Next, we aim to consider these three conditions simultaneously, using “score”. Fig. 3 shows the influences of each parameter on the realization of successful therapy. In Fig. 3A, the effect of *A* is represented. *A* is fixed as one of the three values on the horizontal axis (high, intermediate, and low), and the vertical axis indicates the number of runs achieving scores in the top 10% among all combinations of the other seven parameters ($3^{10} = 59049$ runs).

(i) *Threshold of having symptoms,* θ

Among the three values, the largest (90; Fig. 3A) is most likely to be included in runs with top 10% high score. A high threshold of having symptoms avoids having symptoms in the therapy and exposure phases.

(ii) *Intensity of pollen dose as therapy*, *a*

The largest (0.9; Fig. 3B) was the most likely to be included in runs with top 10% high score. This suggests that larger amount of pollen dose suppresses the symptoms in each

exposure phase more effectively. If the amount of dose is too small (a = 0.1), the therapy is not enough to suppress symptoms. Note that the largest and the intermediate are almost the same value. This suggests that too large amount of dose may lead side effects of therapy, symptoms caused by therapy itself.

(iii) *Intensity of pollen exposure*, A

Among the three A values, the largest (90; Fig. 3C) was the most likely to be included in runs with scores in the top 10%. This suggests that therapy is appropriate when the patient is exposed to a large amount of environmental pollen. If A is smaller, fewer patients have allergic symptoms and the therapy is increasingly redundant.

(iv) *Numbers of differentiating naive T cells per unit dose of pollen*, b

The largest b value (1000) was the most likely to be included in the top 10% of runs (Fig. 3D). To accumulate sufficient numbers of Treg cells for successful therapy, large numbers of naïve T cells need to be stimulated by APCs. In contrast, if b is too large, Th2 and Tregs are produced in response to small doses of pollen and cause allergic symptoms during therapy, leading to failure. We discuss this problem later.

(v) *Rate of differentiation into Th2 cells*, c

The smallest c value (0.5) appeared more frequently in the top 10% of runs than the other two values (Fig. 3E). If a smaller fraction of naive T cells differentiate into Th2 cells, symptoms become less likely, although more Treg cells are produced and enhance the therapeutic effect.

(vi) *Decay rates of Th2 cells*, d_h

The largest d_h value (1.5) was more often included in the top 10% of cases than the other two values (Fig. 3F). As d_h increases, Th2 cells decay more rapidly and the therapy becomes more likely to succeed.

(vii) *Decay rate of Treg cells*, d_r

The smallest d_r value was more likely to be included in the high score group than the larger d_r value (Fig. 3G). Hence, the therapy was more likely to succeed if Treg cells had a longer lifespan, presumably reflecting accumulation of Treg cells and enhanced suppressive effects.

(viii) *Suppression effect of Treg cells*, m

The largest *m* value (0.1) was more likely to be included in the top 10% of cases than the smaller values (Fig. 3H). Hence, stronger suppression prevented differentiation into Th2 cells and blocked allergic symptoms more effectively.

(ix) *Numbers of nTreg cells*, *n*

The smallest *n* value (2.0) was more likely to be included among the top 10% of cases than the larger values (Fig. 3I). Patients with small numbers of nTreg cells had symptoms and needed therapy. However, when *n* was large, high nTreg cell numbers made patients insensitive to pollen, resulting in no allergic symptoms. On the other hand, during the earliest stages of therapy when few iTreg cells had been produced, nTreg cells were crucial to suppress symptoms during therapy. If numbers of nTreg cells were very small, allergic symptoms appeared during therapy. We will discuss this problem later.

(x) *Length of therapy phase*, *T*

The longest therapy phase *T* (900) was more likely to be included in the top 10% of cases than shorter phases (Fig. 3J). If a patient received longer therapy, more Treg cells were accumulated, making the therapy more likely to be successful.

3.3 *Relative peak heights* (S_0, S_T *and* S_E) *and score when parameters are randomly sampled*

We performed parameter sensitivity analysis with random choice of parameters from uniform distribution. Relative peak heights (S_0, S_T *and* S_E) and score are examined. Detailed results are explained in Appendix C. Parameter dependence of desirable parameter values is qualitatively the same as in the analysis reported in section 3.2.

4. Alternative scoring for therapeutic success

In further computations, we examined several alternative methods for scoring the results. Specifically, we considered weighting of the three components (α, β, and γ), and various ways of measuring each component. In Appendix A, we explain these methods in more detail.

4.1 *Alternative weighting of various components for therapeutic success*

Although we changed the weights for α, β, and γ, only the relative values for these weights were consequential and the model remained the same if we multiplied all three weights by the same factor. Thus, we increased the weight for α by factors of 10 and 100 without changing those for β and γ. Using the score with modified weights, successful therapy was most likely for parameter values that were different from those obtained with the standard score from equal weights for all three components, as shown in Eq. 4. However, scores with enhanced weights for α were high for different parameter values. Specifically, larger c, smaller d_h, and smaller m were frequently included in the top 10% of successful cases when we adopted larger weights for α. These observations indicate that more naïve T cells differentiate into Th2 cells, that Th2 cells have a longer life span, and that the weaker suppressive effects of Treg cells increase the likelihood of allergic symptoms. Because a large α represents symptom severity without therapy, this result is quite plausible. In contrast, the results remained the same as those for the standard case even when weights for β or γ only were increased, and the recommended parameter values were the same as the original score. Hence, greater weight for one component over the other components corresponds with greater importance.

4.2 *Variations of scoring methods*

We examined various alternative functional forms for the three components of scores α, β, and γ, using the functions S_0, S_T, and S_E, respectively. The original method for calculating these three components (Eqs. 4, 5a, 5b, and 5c) only considers the value of $H(t)$ when it is greater than the threshold. Hence, these criteria do not distinguish cases with $H(t)$ values that are slightly smaller than the threshold, and in these cases, the peak is much lower than the threshold. This is justified because no symptoms appear if $H(t)$ is below the threshold θ. Accordingly, we considered the following three variations, which are explained in more detail in Appendix A.

Variation 1: We considered contributions of the $H(t)$ peak when it was lower or higher than the threshold. Using this score, we considered a penalty for choosing patients with no symptoms without therapy, and gave a larger score to those with larger margins of symptoms following therapy.

Variation 2: We only considered positive parts of each component of variation 1. In comparisons these with the standard score, this variation differed in β and γ, and a positive score for a larger margin was considered instead of a penalty for failure to satisfy the corresponding conditions for successful therapy.

Variation 3: We considered the functions of power at 0.5 instead of at 0.1. Accordingly, we allowed one component of the score to be very much larger than the other components. For each method, we changed weights for α, β, and γ, as in section 4.1.

Formulas for these variables and the results of analyses using these variations are explained in Appendix A. Generally speaking, these variations provided almost the same results as the standard scoring method (Eqs. 4, 5a, 5b, and 5c). However, in some parameters, the desirable level for successful therapy change with weights of α, β, and γ (Table 2). Variations 1 and 2 consider $H(t)$ values below the threshold θ and assume that numbers of Th2 cells can be measured irrespective of the presence of symptoms.

If a very large weight is given to one component and the power is not very small, other conditions for therapeutic success may be violated in high-score cases (Variation 3). See Appendix B for details.

5. Temporal Patterns of Administration

In Eq. (2), we consider cases in which the patient receives pollen at a constant daily rate during the therapy phase. Below, we consider various patterns of daily pollen intake as specified by different $P(t)$ ($t < T$) values, and examine the performance of therapy with other fixed parameters. Specifically, we studied the effects of (1) intervals between dates of pollen administration and the amount of pollen per dose, (2) gradual changes of pollen doses throughout the therapy, and (3) the total amount administered. To evaluate the performance of these temporal patterns of administration, we focused on peaks of $H(t)$ in the therapy phase ($\max_{t<T} H_w(t)$) and in the exposure phase ($\max_{t>T} H_w(t)$).

To fit the length of phase with symptoms into about 90 days, which is the length of a typical pollen season (Horiguchi et al. 2008), we set $d_h = 0.01$ and $m = 0.045$. For other parameters, we fixed parameters A, b, c, d_h, d_r, m, n, and T at 50.0, 10.0, 0.5, 0.01, 0.001, 0.045, 200.0, and 900.0, respectively.

5.1 *Intervals and amounts of pollen doses*

First, we varied the length of dose intervals and the amount of pollen in one dose, fixing total amount of pollen constant (Appendix E). We compare three methods with different length of intervals. Giving smaller amount of pollen at shorter dose intervals is the best in terms of avoiding symptoms in therapy.

5.2 *Constant, increasing, and decreasing doses*

Next, we examined variations of temporal pattern of administration. Details are explained in Appendix E.

(i) *Gradual changes in daily doses over time* (*constant, increasing, or decreasing*)

We examined three patterns of daily doses; constant, gradually increasing, and gradually decreasing with time. Among these, gradual increase was the most likely to suppress symptoms in therapy.

(ii) *Total doses of treatment schedules*

Next, for each of three patterns in (i), the total amount of pollen throughout therapy was varied and dynamics of the number of Th2 cells were calculated. The results were similar among three patterns: if the total amount of pollen was too small, the therapy was inefficient, and if it was too large, the therapy caused symptoms in the therapy phase.

(iii) *Therapeutic effects under conditions of symptom control*

Considering the result in (ii), we applied another criterion in which the risk of having symptoms in therapy is fixed and we compared therapy effect. We choose representative for each of three patterns and examined maximum A (the amount of environmental pollen) to which the therapy can suppress symptoms after the therapy. As a result, gradually increasing dose can cope with the largest A. If we control the risk of having symptoms, increasing dose with time is the most effective method among three patterns of administration.

5.3 *Conventional method of administration with induction and maintenance phases*

In current medical practice, the term *induction phase* refers to the period in which increasing amounts of pollen extract are administered (Horiguchi *et al*. 2008).

Accordingly, we examined dosing schedules during the induction phase in which the amounts of doses are gradually increased as $P(t) = st$, and in the maintenance phase, in which doses remained constant until the end of therapy. The total length of therapy T was fixed at 900, and the length of the induction phase T_i was varied. We set k as the sizes of maintenance doses.

(i) *Varying T_i with fixed maintenance doses* (k)

Initially, we varied the length of the induction phase T_i and changed the rate of increase s. The daily dose in the maintenance phase was fixed at $k = 20$ (Fig. 8A). In Fig. 4, (A) the therapy schedule and (B) dynamics of the number of Th2 cells ($H(t)$), and (C) dynamics of the number of iTreg cells($R(t)$) are shown. ($H(t)$) Thus, we have $s = k/T_i$. Dose increases during the entire therapy phase are shown as bold lines for $T_i = 900$, and those for the half therapy phase $T_i = 450$ are shown as broken lines. Dash-dotted lines show changes for the induction phase of $T_i = 150$ and dotted lines show that for no induction phase $T_i = 0$. These computations show that $H(t)$ peaks during therapy are decreased with longer induction phases (Fig. 4B). However, longer induction phases led to larger $H(t)$ peaks after therapy, reflecting reduced numbers of iTreg cells in the exposure phase (Fig. 4C).

(ii) *Varying T_i with fixed total doses*

Under conditions of fixed total doses with varying lengths of the induction phase T_i, daily doses in the maintenance phase changed with T_i (Fig. 4D). Computations were performed for $T_i = 900$ (bold lines), $T_i = 450$ (broken lines), $T_i = 150$ (dash-dotted lines) and $T_i = 0$ (dotted lines), and longer induction phases were associated with smaller $H(t)$ peaks (Fig. 4E). However, the peak $H(t)$ value in the exposure phase varied less between dosing schedules than the case of (i). This is because almost the same amount of iTreg accumulate until the exposure to environmental pollen (Fig. 4F).

For both (i) and (ii), increasing doses throughout the therapy phase were associated with low risks of symptoms during therapy. These circumstances differ from conventional treatments with induction and maintenance phases. However, continued increases in doses may be unrealistic because very large doses near the end of the

therapy would likely cause additional complications of digestion and in the formation of regulatory T cells.

Under the conditions of (ii), $H(t)$ peaks after therapy were barely affected by changes in T_i, compared with changes in $H(t)$ peaks during therapy. These results reflect the choice of parameters. In particular, a small d_r value was required for successful therapy, as indicated in the previous section. However, this implies that Treg cells are long lived, that almost all Treg cells accumulate, and that the total dose directly affects the number of Treg cells (Fig 8C and 8F).

6. Discussion

In this paper, we developed a very simple dynamic model of allergen immunotherapy to determine conditions in which therapy is most likely to be successful. To investigate relationships between treatments and each parameter, we defined scores for therapeutic success and calculated these for 3^8 sets of parameters, corresponding to a variety of physical traits and environmental conditions. According to the standard score (Eqs. (4) and (5)), we concluded that therapy would be more effective to patients with more differentiating naive T cells b, larger fraction of differentiating into Th2 cells c, smaller Treg decay rates d_r, large decay rates of Th2 cells d_h, stronger suppressive effects of Treg cells m, and fewer of nTreg cells n. Although the range of parameters (Table 1) was chosen to cover all plausible values, some of these were difficult to identify, warranting further quantitative studies.

We performed computations using several differing scoring methods and found that the most successful value for each parameter depended on the method. Hence, the qualities of participants likely depended on the evaluation method and should be carefully chosen according to intended purpose. For example, if we prioritize the evasion of allergic reactions to the therapy, the component β in the score needs to be strongly weighted, whereas increased weight for the component α is required for treatments of patients with severe symptoms. Hence, patient groups for these two therapies will likely include subjects with differing conditions.

The present computations indicate the need to accommodate multiple parameters simultaneously. Specifically, participants with severe allergic symptoms and very large

α values may show reactions to the therapy, leading to larger than threshold $H(t)$ peaks during therapy. In section 4.1, the weight of α was set at 10 and 100 and cases with $H(t)$ peaks that exceeded the threshold after therapy were included among those with scores in the top 10% (see Appendix B). This scenario represents a failure to choose appropriate participants and warrants moderate weighting of individual components.

In this paper, we investigated contributions of each parameter to the likelihood of therapeutic success and identified associated sets of parameters. Hence, the present computations will enable prospective selection of patients for whom therapy is likely to be successful.

Herein we show that the strength of symptom suppression in the pollen exposure phase depends on the total dose. To prevent symptoms during therapy, gradual dose increases are effective, and enable symptom free administration of greater total amounts of pollen than constant doses. These assertions are consistent with current use of induction and maintenance phases (Horiguchi et al. 2008) *and indicate* the significance of the *induction phase*.

In a previous study by Gross et al., shorter *induction phases* improved therapeutic success because longer *maintenance phase*s are good for increasing numbers of Treg cells, thus facilitating therapeutic success (Gross et al. 2011). In contrast, our analyses (section 5.3) showed that differences in therapeutic success were related to the lifespan of Treg cells. Accordingly, in our models we assumed that the lifespan of regulatory T cells is much longer than that of Th2 cells, because immunotherapy was most effective under these conditions. However, no reliable measurements of regulatory T cell longevity have been published to date. In the model by Gross *et al*., small doses at the beginning of the induction phase failed to produce sufficient numbers of Treg cells to suppress symptoms after therapy. They assumed the same decay constant for all the cell types including Th2s and Tregs, and therefore Treg accumulation was not observed in the induction phase when patients start from a little amount of pollen that is not enough to produce Treg cells which can be maintained until pollen exposure. In contrast, Treg cells accumulated and suppressed allergic symptoms in our model. Moreover, increasing doses over long time periods may be

effective for establishing sufficient numbers of regulatory T cells by the time of pollen exposure, and for avoiding allergic symptoms during therapy.

In the present model, small d_r values were important for therapeutic success. Previous studies of Treg cell longevity revealed that gamma chain cytokines from other cells prevent apoptosis and maintain Foxp3 and CD25 expression, which are important for Treg functions (Pandiyan and Lenardo, 2008). However, exact value of lifetime of Treg cells are not available and we consider that lifetime of iTreg cells are estimated by considering memory iTreg cells (Burzyn et al. 2013). Floess et al. (2007) reported that iTregs are unstable compared to nTregs, due to incomplete demethylation. Though decay rate of iTreg cells we set might be smaller than the actual decay rate, our study demonstrate that the therapy can be successful when decay of iTreg cells is very slow. This suggestion will be useful to explore new target of immunotherapy. For example, another recent study showed that treatments with the immunosuppressive drug rapamycin can enhance the half-lives of Treg cells (Singh et al. 2014). Rapamycin is commonly used in patients with organ transplants, and its effects may lead to smaller d_r values and facilitate success of allergen immunotherapy. Previously, Kanamori *et al*. (2016) suggested that demethylation of specific DNA regions in Treg is important for stabilization and induction of iTregs, and listed candidate drug targets for upregulation and stabilization of iTregs.

For simplicity of the present model, we considered single therapy exposure phases. However, patients usually experience several exposure phases over several years, warranting further development of a more realistic models in which therapy and exposure phases are multiple. Our model also fails to describe patients who are cured completely, because Tregs eventually run out after therapy. Further extensions of our model will be made to accommodate this shortcoming.

Although we included only two types of T cells, previous studies suggest other factors that play roles in the development of allergic symptoms. In particular, Otsuka and Kabashima (2015) showed that basophils facilitate differentiation of naïve T cells into Th2 cells, and Stein *et al*. (2016) showed that Amish people, who strictly follow traditional lifestyles, are less likely to have allergies and asthma than other farmers who have industrialized lifestyles. These observations likely correspond with increased

numbers of neutrophils and decreased numbers of eosinophils but not with significant differences in Treg cell numbers. Hence, the present model may be improved by inclusion of additional cell types.

As with the coefficient n for numbers of nTreg cells, a positive initial value of $H(t)$ might be necessary for our model. Accordingly, the initial $H(t)$ value of 0 may be unrealistic because Th2 cells trigger humoral immune reactions for other kinds of harmful antigens, regardless of allergies. Thus, to consider this value, a constant term indicating the initial $H(t)$ should be added to Eq. 1b. This will elevate the dynamics of $H(t)$, leading to increased chances of allergic symptoms in patients with very large initial $H(t)$ values. This is the same as lowering of the symptom threshold θ. Accordingly, because initial $H(t)$ values among individuals correspond with the threshold θ, the effects of threshold θ could be investigated in terms of initial $H(t)$ values.

Although the present model studied in this paper is very simple, it could be used to inform new methods of the therapy. However, the experimental values of each parameter and the mechanisms of differentiation of T cells remain unknown, warranting further experimental studies to develop more accurate and realistic models.

Acknowledgments

This work was supported by a Grant-in-Aid for General Scientific Research (B) (No. 15H04423) from the Japan Society for the Promotion of Science to Y.I. We would like to thank the following people for their helpful comments: M. P. Davenport, H. Haeno, R. Iritani, K. Ito, S. Iwami, S. Nakaoka, H. Ohtsuki, K. Saeki, A. Sasaki, S. Satoi, M. Seki, Y. Takeuchi, K. Uchinomiya, and R. Yamaguchi.

References

Burzyn, D., Benoist, C., Mathis, D., 2013. Regulatory T cells in nonlymphoid tissues. Nat Immunol. 14, 1007–13, doi:10.1038/ni.2683.

Fishman, M. A., Segel, L. A., 1996. Modeling immunotherapy for allergy. B Math Biol. 58, 1099–1121.

Floess, S., Freyer, J., Siewert, C., Baron, U., Olek, S., Polansky, J., Schlawe, K., Chang, H., Bopp, T., Schmitt, E., Klein-Hessling, S., Serfling, E., Hamann, A., Huehn, J., 2007. Epigenetic control of the foxp3 locus in regulatory T cells. Plos Biology 5, 169-178, doi:10.1371/journal.pbio.0050038.

Freeman, J., 1911. Further observations on the treatment of Hay fever by hypodermic inoculations of pollen vaccine. Lancet 2, 814–817.

Gross, F., Metzner, G., Behn, U., 2011. Mathematical modeling of allergy and specific immunotherapy: Th1-Th2-Treg interactions. J Theor Biol. 269, 70–78, doi: 10.1016/j.jtbi.2010.10.013.

Horiguchi, S., Okamoto, Y., Yonekura, S., et al, 2008. A randomized controlled trial of sublingual immunotherapy for Japanese cedar pollinosis. Int Arch Allergy Imm. 146, 76–84, doi:10.1159/000112506.

Kanamori, M., Nakatsukasa, H., Okada, M., et al, 2016. Induced Regulatory T Cells: Their Development, Stability, and Applications. Trends Immunol. doi:10.1016/j.it.2016.08.012.

Kim, Y., Lee, S., Kim, Y., et al, 2013. Regulation of th1/th2 cells in asthma development: a mathematical model. Math Biosci Eng. 10, 1095–1133, doi:10.3934/mbe.2013.10.1095.

Kogan, Y., Agur, Z., Elishmereni, M., 2013. A mathematical model for the immunotherapeutic control of the th1/th2 imbalance in melanoma. Discrete Cont Dyn-B. 18, 1017–1030, doi:10.3934/dcdsb.2013.18.1017.

Liu, A. H., 2015. Revisiting the hygiene hypothesis for allergy and asthma. J Allergy Clin Immunol. 136, 860–865, doi:10.1016/j.jaci.2015.08.012.

Lluis, A., Depner, M., Gaugler, B., et al. Increased regulatory T-cell numbers are associated with farm milk exposure and lower atopic sensitization and asthma in childhood. J Allergy Clin Immun. 133, 551-+, doi: 10.1016/j.jaci.2013.06.034.

Luckheeram, R., Zhou, R., Verma, A., Xia, B., 2012. CD4(+)T Cells: Differentiation and Functions. Clin Dev Immunol. doi:10.1155/2012/925135.

Moingeon, P., Mascarell, L., 2012. Induction of Tolerance via the Sublingual Route: Mechanisms and Applications. Clinical & Developmental Immunology, doi:10.1155/2012/623474.

Noon, L., 1911. Prophylactic inoculation against hay fever. *Lancet* 1, 1572–1573.

Okubo, K., Gotoh, M., 2009. Sublingual immunotherapy for Japanese cedar pollinosis. Allergol Int 58, 149–54, doi: 10.2332/allergolint.08-RAI-0072.

Otsuka, A., Kabashima, K., 2015. Contribution of basophils to cutaneous immune reactions and Th2-mediated allergic responses. Frontiers in Immunology. 6, doi:10.3389/fimmu.2015.00393.

Pandiyan, P., Lenardo, M. J., 2008. The control of CD4+CD25+Foxp3+ regulatory T cell survival. Biol Direct. 3, 6, doi:10.1186/1745-6150-3-6.

Pfaar, O., Bachert, C., Bufe, A., et al, 2015. Guideline on allergen-specific immunotherapy in IgE-mediated allergic diseases. Allergologie. 38, 431–470, doi:10.5414/ALX01762.

Radulovic, S., Jacobson, M. R., Durham, S. R., et al, 2008. Grass pollen immunotherapy induces Foxp3-expressing CD4+ CD25+ cells in the nasal mucosa. J Allergy Clin Immunol. 121, 1467–72, 1472.e1, doi: 10.1016/j.jaci.2008.03.013.

Sakaguchi, S., Yamaguchi, T., Nomura, T., et al., 2008. Regulatory T cells and immune tolerance. *Cell.* 133, 775–787, doi: 10.1016/j.cell.2008.05.009.

Schaub, B., Liu, J., Höppler, S., et al, 2009. Maternal farm exposure modulates neonatal immune mechanisms through regulatory T cells. J Allergy Clin Immunol. 123, 774–82.e5, doi: 10.1016/j.jaci.2009.01.056.

Shiomori, T., Udaka, T., Hashida, K., et al, 2007. Evaluation of quality of life in patients with allergic rhinitis. J Uoeh. 29, 159–67.

Singh, K., Stempora, L., Harvey, R., et al, 2014. Superiority of rapamycin over tacrolimus in preserving nonhuman primate treg half-life and phenotype after adoptive transfer. Am J Transplant. 14, 2691–2703, doi:10.1111/ajt.12934.

Smaldini, P., Delgado, M., Fossati, C., et al, 2015. Orally-induced intestinal cd4(+) cd25(+) foxp3(+) treg controlled undesired responses towards oral antigens and effectively dampened food allergic reactions. Plos One 10, doi: 10.1371/journal.pone.0141116.

Stein, M. M., Hrusch, C. L., Gozdz, J., et al, 2016. Innate Immunity and Asthma Risk in Amish and Hutterite Farm Children. N Engl J Med. 375, 411–421, doi:10.1056/NEJMoa1508749.

Taylor, A., Verhagen, J., Blaser, K., et al, 2006. Mechanisms of immune suppression by interleukin-10 and transforming growth factor-beta: the role of T regulatory cells. Immunology. 117, 433–442, doi:10.1111/j.1365-2567.2006.02321.x.

Vignali, D., Collison, L., Workman, C., 2008. How regulatory T cells work. Nat Rev Immunol. 8, 523–532, doi:10.1038/nri2343.

Wing, K., Onishi, Y., Prieto-Martin, P., et al, 2008. CTLA-4 control over Foxp3(+) regulatory T cell function. Science. 322, 271–275, doi:10.1126/science.1160062.

Yamada, T., Saito, H., Fujieda, S., 2014. Present state of Japanese cedar pollinosis: the national affliction. J Allergy Clin Immunol. 133, 632–639.e5, doi:10.1016/j.jaci.2013.11.002.

Appendix A

Parameter sensitivity of *relative peak height without therapy, in therapy phase and in exposure phase* (S_o, S_T, S_E)

We investigated the parameter sensitivity of three relative peak heights, S_o, S_T and S_E in Eq. (3a), (3b) and (3c), which determine score (Eq. (5a), (5b) and (5c)). In $3^{10} = 59049$ combinations of parameter, S_o, S_T and S_E was investigated and plotted in Fig. 5 against three level of 10 parameters. Larger b and c are likely to lead higher peak of $H(t)$. b represents sensitivity of naïve T cells to pollen and c represents the fraction of differentiation into Th2 cells. If these values are large, Th2 cells are more produced and allergic symptoms are more likely to developed. Smaller dh, m and n are likely to lead higher peak of $H(t)$. d_h, m and n represent decay rate of Th2 cells, the suppression effect of Treg cells and nTreg cells, respectively. If these values are small, Th2 cells are more produced and accumulated, and patients are likely to have symptoms. These are conditions that the patients are likely to have symptoms.

Appendix B.

Alternative scoring for therapeutic success

B.1 Weighting of components for therapeutic success

In the standard scoring system exemplified by Eqs. (4), (5), α, β, and γ have equal impact. Hence, we considered various scenarios with higher importance of one of the three components.

Initially, we investigated the effects of increasing the impact of component α, leading to new scores of $score = 10\alpha + \beta + \gamma$ and $score = 100\alpha + \beta + \gamma$, and a standard score of $score = \alpha + \beta + \gamma$.

The present computations changed with increased weight of α, (Table 2A), and at α values of 1, 10, 100, c = 0.5 was increased to c = 0.9, and d_h =1.5 and m = 0.1 were decreased to 0.5 and 0.001, respectively. Because α is an indicator of allergy without therapy, these changes increased the chances of allergic symptoms. In the result of $score = \alpha + \beta + \gamma$, all the parameter with top 10% high score achieved $\beta = 0$ and $\gamma = 0$, which implies that symptoms in and after therapy did not occur. On the other hand, enhancing the weight of alpha ($score = 10\alpha + \beta + \gamma$ and $score = 100\alpha + \beta + \gamma$), some cases achieved top 10% high score, even either or both of their β and γ are negative, due to very large effect of alpha. This caused change of the cases among the cases with different weight of alpha.

In a similar manner, we considered changes in the weight of β, and compared the results of $score = \alpha + 10\beta + \gamma$ and $score = \alpha + 100\beta + \gamma$ with those of the standard method $score = \alpha + \beta + \gamma$. We also considered changes in the weight of γ, in comparisons of the effects of $score = \alpha + \beta + 10\gamma$ and $score = \alpha + \beta + 100\gamma$ with the standard score. β and γ are penalties for having symptoms with therapy, and using the standard score, the top 10% of successful cases did not have symptoms with therapy ($\beta = 0$ and $\gamma = 0$). Therefore, increasing the weights of β and γ did not change the results from those with the standard score.

In conclusion, successful c, d_h, and m values changed depending on the weight of α (Table 2A). Specifically, increasing the weight of α corresponds with initial choices of participants with severe symptoms, which may lead to different selections of patients

for whom allergen immunotherapy is successful than when the 3 components are considered equally.

B.2 Variations of scoring methods

We considered the following 3 variations of scoring methods: (1) Application of $H(t)$ peaks that are smaller than θ to the score, (2) not considering scores with negative values, and (3) changing the power from 0.1 to 0.5. We also changed weights for α, β, and γ as in section A.1 (Eq. (3)).

Variation 1: Incorporation of H(t) values below the threshold into the score

To consider peaks of $H(t)$ that were below the threshold, we defined $\alpha, \beta,$ and γ as follows:

$$\alpha = \begin{cases} |S_o|^{0.1} & \text{if } S_o \geq 0 \\ -|S_o|^{0.1} & \text{if } S_o < 0 \end{cases}$$
$$\beta = \begin{cases} |S_T|^{0.1} & \text{if } S_T < 0 \\ -|S_T|^{0.1} & \text{if } S_T \geq 0 \end{cases} \quad \text{(A.1)}$$
$$\gamma = \begin{cases} |S_E|^{0.1} & \text{if } S_E < 0 \\ -|S_E|^{0.1} & \text{if } S_E \geq 0 \end{cases}.$$

We calculated scores as the sum of these components ($score = w_\alpha\alpha + w_\beta\beta + w_\gamma\gamma$) with w_α, w_β, and w_γ as weights of each component at 1, 10, and 100. We calculated the scores for 3^8 parameter sets according to this method.

In this method, $H(t)$ values that were smaller than the threshold for developing symptoms were included in the score, assuming that $H(t)$ values below the threshold can be detected. Using this method, the strength of therapeutic suppression of symptoms can be evaluated even if symptoms do not occur.

With increasing weights of α, c, d_h, and m tend to reflect allergic symptoms, as in section 4.1 (Table 2B(i)). However, increasing weights of β, a, b, and n result in changes of the main value included in the successful group (Table 2B(ii)). Finally, as the weight of γ gets larger, the most included value of A, b, and n changes (Table 2B(iii)), as described below.

Variation 2: Not considering reductions of scores depending on undesirable conditions for therapeutic success. We calculated scores for 3^{10} parameter sets according to following equations (A.2): $\alpha, \beta, and\ \gamma$ were defined using $[x]_- = x\ if\ x \leq 0, [x]_- = 0\ if\ x > 0$:

$$\alpha = ([S_o]_+)^{0.1},\ \beta = |[S_T]_-|^{0.1} and\ \gamma = |[S_E]_-|^{0.1} \qquad (A.2)$$

In this method, only the degree of appropriateness for therapy is evaluated, as shown in Table 2C (i), (ii), and (iii). These results are similar to those following (1) application of H values that are smaller than θ to the score. As the weight of α gets larger, the tendencies of c, d_h, and m change (Table 2C(i)), as the weight of β gets larger, tendencies of a, b and n change (Table 2C(ii)), and increases in the weight of γ lead to changes in the tendencies of A, b and n (Table 2C(iii)).

Variation 3: Using the power function of 0.5 in the score
Scores are calculated according to the following equations:

$$\alpha = ([S_o]_+)^{0.5}, \qquad \beta = -([S_T]_+)^{0.5}\ and\ \gamma = -([S_E]_+)^{0.5}. \qquad (A.3)$$

The effect of very large $H(t)$ peaks was smaller than the standard score. (Eq. (3); Table 2D). As the weight of α was increased, tendencies of c, d_h, and m changed, and as the weight of β increased, tendencies of a changed, whereas increased weights of γ had little effect.

Among three variations, with the weight of β increased, the small a (0.1) tends to be included in the successful group. Too large amount of pollen dose as therapy, large a, can be risky because it may cause symptoms, and thus small amount of pollen dose is desirable if weight for β is very large.

Results of variations 1 and 2 show similar tendencies (Table 2B and C). Specifically, in addition to the changes of c, d_h, and m with increased weights of α,

similar to the results of the standard method, changes in the weight of β resulted in changes of a, b and n and changes in the weight of γ resulted in changes of A, b and n.

If the weight for β is very large, small b (10) and large n (200) are more frequently included in the top 10% of successful cases. Since b represents the number of naïve T cells that differentiate per unit of pollen, when b is large, even mild therapy promotes differentiation of naïve T cells into Th2 cells, indicating negative control for β. Similarly, n represents the number of nTreg cells, which are produced regardless of differentiation of naïve T cells. Accordingly, nTreg cells prevent symptoms in the early stage of therapy when few iTreg cells have been produced.

With increased weight of γ, the small A (A = 10) tends to be included in the successful group. Because γ is an indicator of therapeutic effect during the exposure phase, greater importance of γ diminishes the preferred environmental pollen exposure. Thus, to prevent symptoms in the exposure phase, this approach may be used to treat patients who are unlikely to experience symptoms during years when pollen production is small.

Appendix C

Relative peak heights (S_0, S_T and S_E) and score when parameters are randomly sampled from uniform distribution

In addition to setting three levels of parameters in section 3, we derived parameters from uniform distribution to perform minute investigation of parameter dependence. We derived 1000 combinations of parameters and plotted the values of three relative peaks (S_0, S_T and S_E) (Fig. 6A) and score (Fig. 6B).

In Fig. 6A, the figures in the left row represent plots of S_0, relative peak of $H(t)$ without therapy. Larger A and b value are likely to lead higher S_0, and smaller m and n, are likely to lead higher S_0. The figures in the middle row represent plots of S_T, relative peak of $H(t)$ in therapy. The larger a and m parameter value are likely to lead higher S_T, and the smaller θ and m are likely to lead higher S_T. The figures in the right row represent plots of S_E, relative peak of $H(t)$ after therapy. In c, the larger parameter value is likely to lead higher S_E, and in a and m, the smaller parameter value is likely to lead higher S_E.

In Fig. 6B, the plots of score in Eq. (4), (5a), (5b) and (5c) are shown against each of 10 parameters. In each figure, three clusters can be seen; upper, middle and lower layer of plots. This structure derived from the definition of score; we consider the function of 0.1 power of relative peak heights (Eq. (5a), (5b) and (5c)) and α, β, or γ approaches a constant value if S_0, S_T or S_E is very large, respectively. In upper layer, successful cases with score by alpha and without penalties of beta and gamma are plotted. In middle layer, the cases with score of alpha and one penalty for either beta or gamma are plotted and lower layer includes the cases with both penalty of beta and gamma. The black dots represent the cases with top 10% score among 1000 trials. In section 3, we investigated the cases with top 10% high score among 59049 combinations of parameters. Similar tendency was observed between the black dots in Fig. B2 and the result of section 3 in Fig. 3; large value of θ, a, b and m, and small value of c, d_r and n are likely to be included in top 10% successful cases.

Appendix D

We defined therapy as successful if $S_0 > 0$, $S_T < 0$, and $S_E < 0$. Some of our scoring methods gave high scores even in unsuccessful cases, in which one or more of the three criteria were violated. Thus, for each scoring method (standard method, variation 1, 2 and 3), we calculated percentages of cases in which the criteria $S_0 > 0$, $S_T < 0$, and $S_E < 0$ are satisfied.

We represented weights of α, β, and γ as w_α, w_β, and w_γ, respectively. In these computations, α, β, and γ are functions of S_0, S_T, and S_E (see Eq. 5a, 5b, and 5c). Black bars indicate percentages of cases satisfying $S_0 > 0$, striped bars represent percentages of the cases satisfying $S_T < 0$, and white bars represent percentages of the cases satisfying $S_E < 0$. Bar graphs correspond with the weights w_α, w_β, and w_γ.

In the standard scoring method (Fig. 7A), percentages of successful cases in terms of S_T and S_E decreased with increasing w_α. Prioritization of S_0 may violate the conditions for S_T and S_E, leading to failure of therapy.

In the variations 1 and 2 (Fig. 7B, 7C), high priority of S_0 (w_α, w_β, w_γ = 10, 1, 1 or 100, 1, 1) and extremely large weights of S_T and S_E (w_α, w_β, w_γ = 1, 100, 1 or 1, 1, 100, respectively), may violate one or two criteria, and may lead to errors in choices of patients.

In the variation 3 (Fig. 7D), the three components were weighted equally (1, 1, 1) and could lead to failure to choose patients with sufficient margins of safety in therapy and exposure. Because the power was 0.5 (Eq. A.3), one component could be very large and achieve a high score even if the other two criteria are violated. Increasing weights of β and γ improves this situation, although power of 0.5 may be insufficient to weaken very large values of one component if the three components are weighted equally.

Appendix E

Temporal Patterns of Administration

5.1 *Intervals and amounts of pollen doses*

Frequency of treatments with pollen extract is an important aspect of therapeutic schedules. We set I as the dosing interval (time t between successful treatments with pollen extract). We also considered (A; $I = 10$) administration of pollen 90 times at 50 (Fig. 8A), (B; $I = 20$) 45 times at 100 (Fig. 8B), and (C; $I = 60$) 15 times at 300 (Fig. 8C). Under all three conditions the total amount of pollen taken by the patient is 4500, and the whole phase for the therapy is constant at $T = 900$ days. We examined the two peak values of $H(t)$ to indicate the magnitude of symptoms. If the total administered amount was the same, symptoms induced by therapy tended to be more severe when I was larger, reflecting larger doses given less frequently. In contrast, symptoms during the exposure phase did not vary with I.

5.2 *Constant, increasing, and decreasing doses*

(i) *Gradual changes in daily doses over time* (*constant, increasing, or decreasing*)

Fig. 9 illustrates comparisons of (A) fixed pollen doses of 50 (Fig. 9A), (B) increasing doses with time following $P(t) = 0.1099t$ (Fig. 9B), and (C) decreasing pollen doses with time following $P(t) = 98.91 - 0.1099t$ (Fig. 9C). Total doses were the same for each treatment regimen. Treatments with increasing doses (B) suppressed symptoms during therapy most successfully, whereas method (C) caused the most severe symptoms during therapy. During the exposure phase, symptoms were most severe with method (C). Hence, method (C) produces worse outcomes than methods (A) and (B). Moreover,

increasing doses (B) with time tended to gradually suppress $H(t)$ peaks during the exposure phase without causing symptoms during therapy.

(ii) *Total doses of treatment schedules*

Treatments with larger amounts of pollen before exposure to environmental pollen should lead to greater accumulation of Treg and enhanced resistance to pathogens. Therefore, total doses should correspond with therapeutic effects. However, administration of large amounts of pollen during the therapy phase increases the risk of symptoms during the therapy phase. Thus, we examined the effects of changing total doses in each of the treatment schedules (A), (B), and (C).

Initially, we adopted a constant dose and made observations at $P(t) = 0.1$, 0.5, 6.0, and 21.0 (Fig. 10A). Single doses need to be within a certain range to optimize effects and side effects. At $P(t) = 0.1$, the total dose was too small to suppress symptoms after therapy, whereas at $P(t) = 21.0$, single doses were too large and caused symptoms. At $P(t) = 0.5$ and 6.0, both peaks of $H(t)$ did not exceed the threshold θ and the therapy was successful.

Subsequently, we examined the effects of gradual dose increases following $P(t) = st$ (where s is speed $s > 0$) instead of a constant value, and observed changes in slope s (Fig. 10B). s was optimized for therapeutic efficacy with no side effects. When $s = 0.0002$, symptoms were not suppressed after therapy, whereas successful therapy was achieved with $s = 0.003$ and 0.02 and $s = 0.5$ caused symptoms.

In further computations, we examined the effects of gradual dose decreases in the shape of $P(t) = s\ (T - t)$ (where s is the speed of increase) and increased total amounts with s (Fig. 10C). The dose reached zero at T: $P(T) = 0$ and when $s = 0.00003$. Hence, the therapy was too weak to suppress symptoms during the exposure phase. When $s = 0.00018$ and 0.0008, H(t) peaks were low in both therapy and exposure phases. When s was 0.002, the peak in the exposure phase was the highest and the risk of symptoms during therapy was the largest.

(iii) *Therapeutic effects under conditions of symptom control*

Suppressive effects were compared between constant (Fig. 9A), increasing (Fig. 9B), and decreasing pollen doses (Fig. 9C) to determine which method suppresses symptoms at larger values of A (daily pollen dose during the exposure phase). We assumed that higher pollen dispersal would produce better therapeutic effects and represented the methods as $P(t) = 0.4705$, $0.000204t$, and $0.5202-0.0000578t$, respectively. All treatment schedules produced symptoms with degrees of 10.

Subsequently, we represented methods (a), (b), and (c) as $P(t) = 19.85$, $0.0397t$, and $0.5202-0.0000578t$, respectively, and compared symptom suppression with increasing pollen dispersal. Under gradual increases of released pollen (A), H reached the threshold θ (Fig. 11A), and at $P(t)=0.4705$, H reached the threshold θ at around $A = 124$. When $P(t) = 0.000204t$, H reached θ at around $A = 223$ (Fig. 11B) and when $P(t) = 0.5202-0.0000578t$, H reached θ at around $A = 76$ (Fig. 11C). Therefore, increasing doses with time suppressed symptoms during larger environmental pollen exposures than for the other treatment schedules. These computations indicate that increasing dose schedules has therapeutic effect on greater pollen dispersal than other methods.

Tables

Table 1 Values of the parameters

Three values are shown for each parameter, resulting in 3^{10} parameter combinations. We calculated $H(t)$ and $R(t)$ for each set of 3^{10} parameters and present units for parameters in which PU is the unit amount of pollen and CU is the unit number of cells.

	symbol	low	intermediate	high	unit
Threshold of having symptoms	θ	10	50	90	CU
Intensity of pollen dose as therapy	a	0.1	0.5	0.9	PU/day
Intensity of pollen exposure	A	10	50	90	PU/day
Numbers of differentiating naive T cells per unit dose of pollen	b	10	100	1000	CU/PU
Rate of differentiation into Th2 cells	c	0.5	0.7	0.9	1
Decay rates of Th2 cells	d_h	0.5	1.0	1.5	1/day
Decay rate of Treg cells	d_r	0.001	0.01	0.1	1/day
Suppression effect of Treg cells	m	0.001	0.01	0.1	1/CU
Numbers of nTreg cells	n	2	20	200	CU
Length of therapy phase	T	100	500	900	day

Table 2 Desirable levels of parameters changing with weights of α, β, and γ for each scoring method

Three values (large, intermediate, and low) were set for each of ten parameters and scores were calculated for all 3^{10} combinations. We then determined which of the three levels are most frequently included in successful parameter sets with scores in the top 10%. Scores were calculated as $score = w_\alpha \alpha + w_\beta \beta + w_\gamma \gamma$. We considered the scoring methods standard and variations 1, 2, and 3. Definitions of $\alpha, \beta,$ and γ differ among these methods (Eq. A.1, A.2 and A.3) and w_α, w_β, and w_γ were varied at 1, 10, and 100 to examined the influence of increasing weights of single components in comparisons of the cases as follows:

(i) $(w_\alpha, w_\beta, w_\gamma) = (1,1,1), (10,1,1),$ and $(100,1,1)$,

(ii) $(w_\alpha, w_\beta, w_\gamma) = (1,1,1), (1,10,1),$ and $(1,100,1)$, and

(iii) $(w_\alpha, w_\beta, w_\gamma) = (1,1,1), (1,1,10),$ and $(1,1,100)$. For each table, the leftmost column shows the values of w_α, w_β, or w_γ and other columns show the parameter values that were the most successful of the three alternatives. Large, intermediate and small values are shown in brackets, but only for parameters in which the most successful level was changed by increases in the weights of components $\alpha, \beta,$ or γ.

(A) As a standard method, we calculated components of the score (α, β and γ) using Eq. (4) and Eqs. (5a), (5b), and (5c), and considered different weights of α, β, and γ. Increasing the weight of α (w_α) influenced the results of c, d_h, and m.

(B) In variation 1, we calculated α, β, and γ using Eq. (A.1). In addition to the standard method, we evaluated $H(t)$ values that were below the threshold. (i) Increased w_α also changed the results of c, d_h, and m, whereas (ii) increasing w_β changed the results of b and n and (iii) increasing w_γ changed the result of A.

(C) In variation 2, we calculated α, β, and γ using Eq. (A.2). In this method, only the degree of success of each component was evaluated, and the results were similar to those of variation 1. Specifically, (i) increasing w_α changed the results of c, d_h, and m, (ii) increasing w_β changed the results of b and n, and (iii) increased w_γ changed the results of A.

(D) In variation 3, we calculated α, β, and γ using Eq. (A.3). The effects of extremely large components on the score were stronger than in the standard method. Specifically,

increasing w_α changed the results of c, d_h, and m.

(A) standard

w_a	c	d_h	m
1	0.5 (small)	1.5 (large)	0.1 (large)
10	0.9 (large)	1.0 (intermediate)	0.001 (small)
100	0.9 (large)	0.5 (small)	0.001 (small)

(B) variation 1

(i)

w_a	c	d_h	m
1	0.5 (small)	1.5 (large)	0.1 (large)
10	0.9 (large)	1.5 (large)	0.001 (small)
100	0.9 (large)	0.5 (small)	0.001 (small)

(ii)

w_β	a	b	n
1	0.9 (large)	1000 (large)	2 (small)
10	0.5 (intermediate)	100 (intermediate)	2 (small)
100	0.1 (small)	10 (small)	200 (large)

(iii)

w_γ	A	b	n
1	50 (intermediate)	1000 (large)	2 (small)
10	50 (intermediate)	1000 (large)	2 (small)
100	10(small)	10 (small)	200 (large)

(C) variation 2

(i)

w_a	c	d_h	m
1	0.5 (small)	1.5 (large)	0.1 (large)
10	0.9 (large)	0.5 (small)	0.001 (small)
100	0.9 (large)	0.5 (small)	0.001 (small)

(ii)

w_β	a	b	n
1	0.9 (large)	1000 (large)	2 (small)
10	0.1 (small)	100 (intermediate)	2 (small)
100	0.1 (small)	10(small)	200 (large)

(iii)

w_γ	A	b	n
1	50 (intermediate)	1000 (large)	2 (small)
10	10(small)	10 (small)	200 (large)
100	10(small)	10 (small)	200 (large)

(D) variation 3

(i)

w_a	c	d_h	m
1	0.7 (intermediate)	1.5 (large)	0.01 (intermediate)
10	0.9 (large)	0.5 (small)	0.001 (small)
100	0.9 (large)	0.5 (small)	0.001 (small)

(ii)

w_β	a
1	0.9 (large)
10	0.1 (small)
100	0.1 (small)

Figures

Figure 1 Scheme of the model

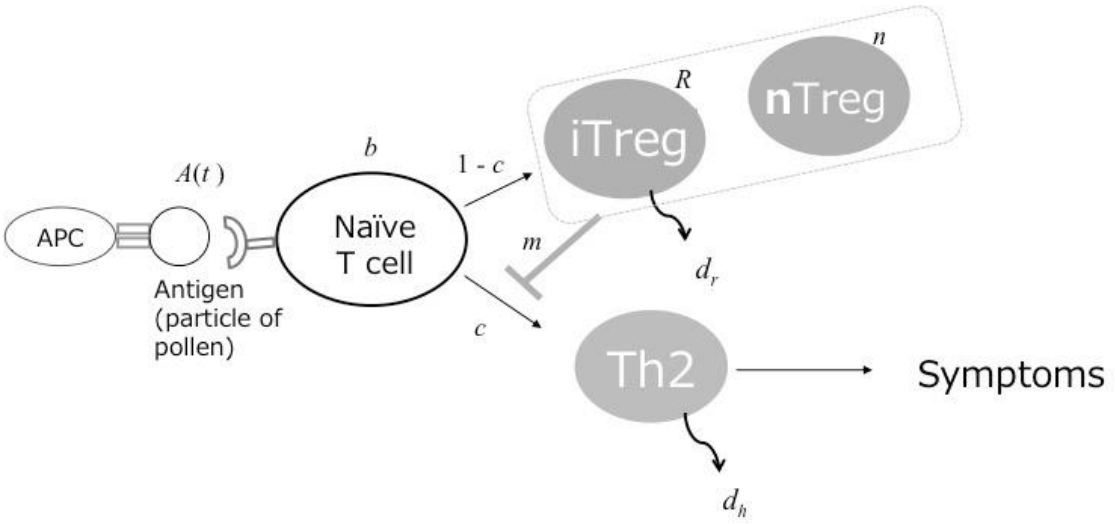

An antigen-presenting cell presents $P(t)$ pollen particles to naive T cells (Th0), which subsequently produce b differentiated T cells. Fraction c of Th0 cells differentiate into type-2 T helper cells (Th2 cells), and fraction 1-c of these differentiate into regulatory T cells (Treg cells). Th2 cells and Treg cells decay at rates of d_h and d_r, respectively; Numbers of naturally occurring regulatory T cells (nTregs) are indicated by n.

Figure 2 Results of Four therapeutic schedules

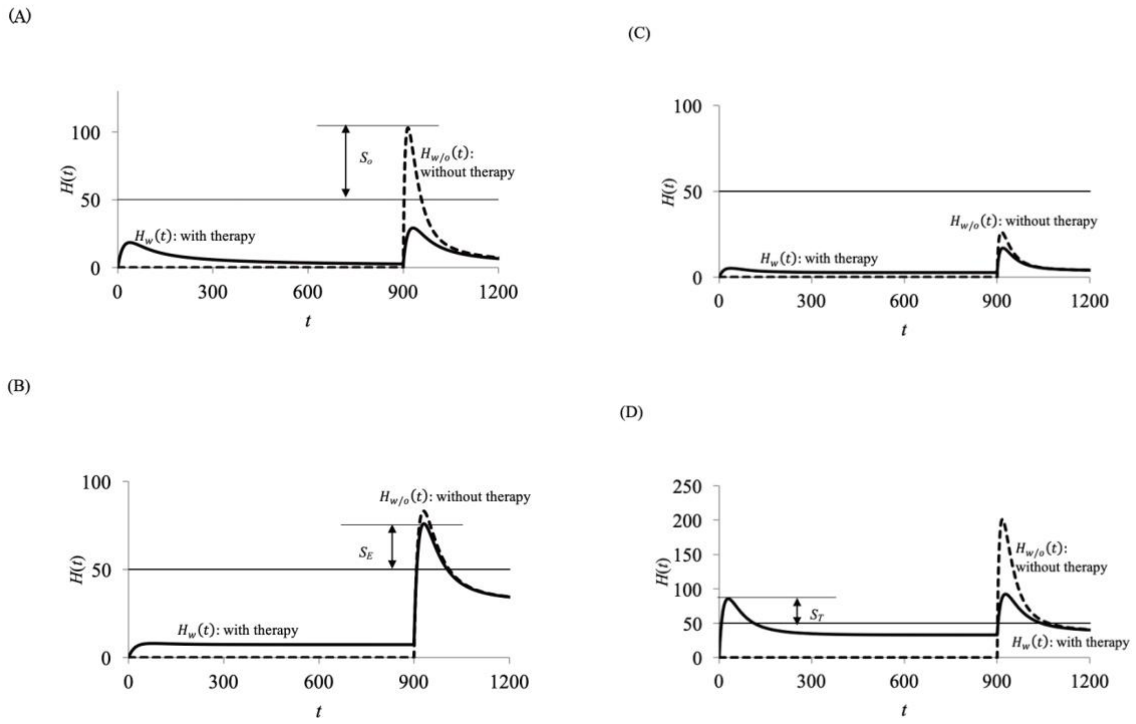

The vertical axis shows the number of Th2 cells $H(t)$, and the horizontal axis shows time t. Broken and solid lines represent without and with therapy, respectively. The phase for $t < T = 900$ is the therapy phase, and the phase for $t > T = 900$ is the environmental pollen exposure phase. (A) Therapy was successful ($\theta = 50$, $a = 0.5$, $A = 10.0$, $b = 10.0$, $c = 0.9$, $d_h = 0.05$, $d_r = 0.001$, $m = 0.1$, $n = 20.0$, $T = 900.0$). Without therapy, $H(t)$ exceeds the threshold for symptoms ($\theta = 50$) in the exposure phase. With therapy, $H(t)$ did not reach $\theta = 50$. We regard this condition as success of allergen immunotherapy. S_0, S_T, and S_E were used to calculate scores (see Eqs. 3a, 3b, and 3c). (B) Therapy fails to suppress symptoms in the exposure phase ($\theta = 50$, $a = 0.5$, $A = 10.0$, $b = 10.0$, $c = 0.9$, $d_h = 0.05$, $d_r = 0.01$, $m = 0.045$, $n = 200.0$, $T = 900.0$). Both without and with therapy, $H(t)$ exceeds the threshold $\theta = 50$ in the exposure phase. (C) Even without therapy, patients do not have symptoms ($\theta = 50$, $a = 0.5$, $A = 10.0$, $b = 10.0$, $c = 0.9$, $d_h = 0.05$, $d_r = 0.01$, $m = 0.45$, $n = 20$, $T = 900.0$); Therapy is unnecessary under these conditions. (D) In the therapy phase, $H(t)$ exceeds the threshold $\theta = 50$ and patients experience allergic symptoms ($\theta = 50$, $a = 2.0$, $A = 10.0$, $b = 10.0$, $c = 0.9$, $d_h = 0.05$, $d_r = 0.01$, $m = 0.045$, $n = 20$, $T = 900.0$).

Figure 3 Analysis of the influence of each parameter value

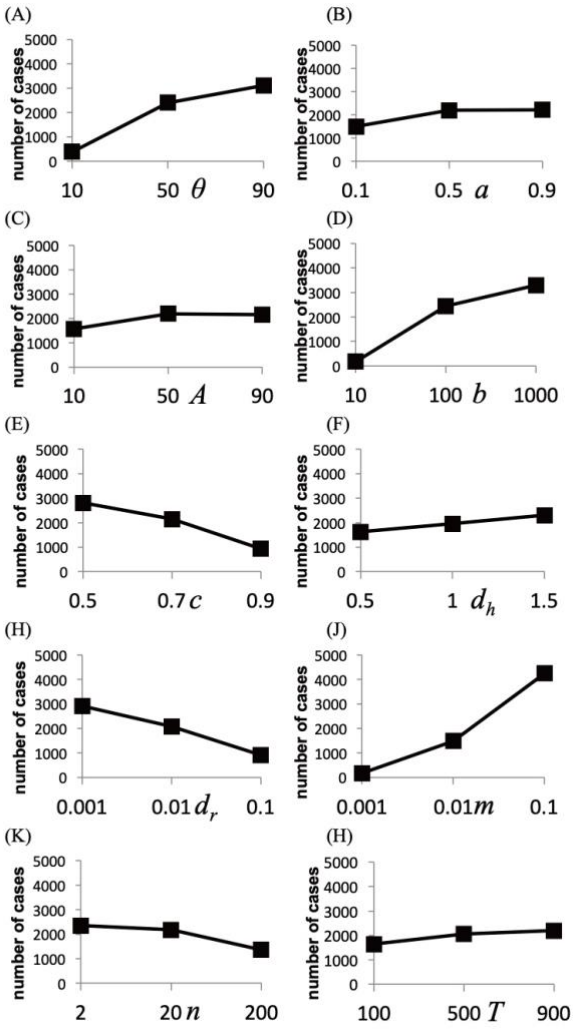

The score given by Eqs. 4, 5a, b, and c was adopted and the model is presented for 3^{10} parameter sets (Table 1). The horizontal axis shows three levels for each parameter and the vertical axis shows the number of cases achieving scores in the top 10% with the focal parameters specified in the horizontal axis. (a) Threshold of having symptoms, θ; (b) Intensity of pollen dose as therapy, a; (c) Intensity of pollen exposure, A; (d) Numbers of differentiating naive T cells per unit dose of pollen, b; (e) Rate of differentiation into Th2 cells, c; (f) Decay rates of Th2 cells, d_h; (g) Decay rate of Treg cells, d_r; (h) Suppression effect of Treg cells, m; (i) Number of nTreg cells, n; (j) Length of Therapy phase, T. Values that show large numbers of cases are likely to be associated with therapeutic success.

Figure 4 Variation of conventional method of pollen administration

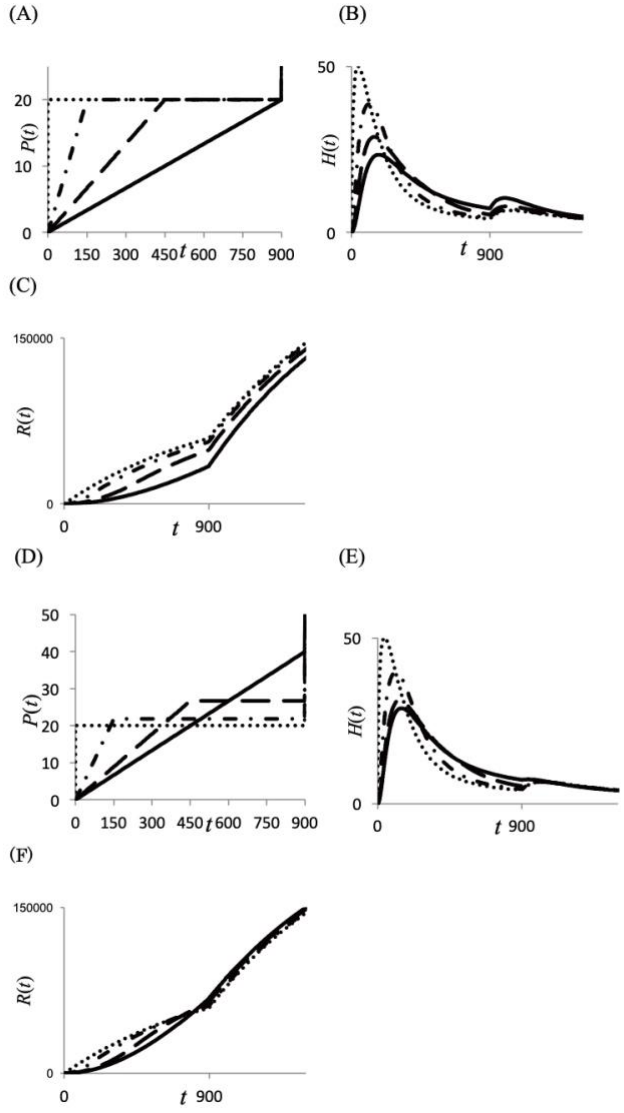

We changed the length of the induction phase T_i. The left graphs show therapy schedules; Vertical axes show $P(t)$ and horizontal axes shows time t. The right graphs show numbers of Th2 cells with time; Vertical axes shows $H(t)$ and horizontal axes shows time t. The length of therapy period was $T = 900$ for all methods. In (A) and (B), bold lines show cases of $T_i = 900$, broken lines show cases of $T_i = 450$, broken and dotted lines show cases of $T_i = 150$, and dotted lines show cases of $T_i = 0$. (A) The constant dose in the maintenance phase was fixed at $k = 20$ and T_i values were 0, 150, 450, and 900. (B) Constant total dose between methods with T_i values of 0, 150, 450, and 900.

Figure 5 Parameter sensitivity of relative peak height of $H(t)$

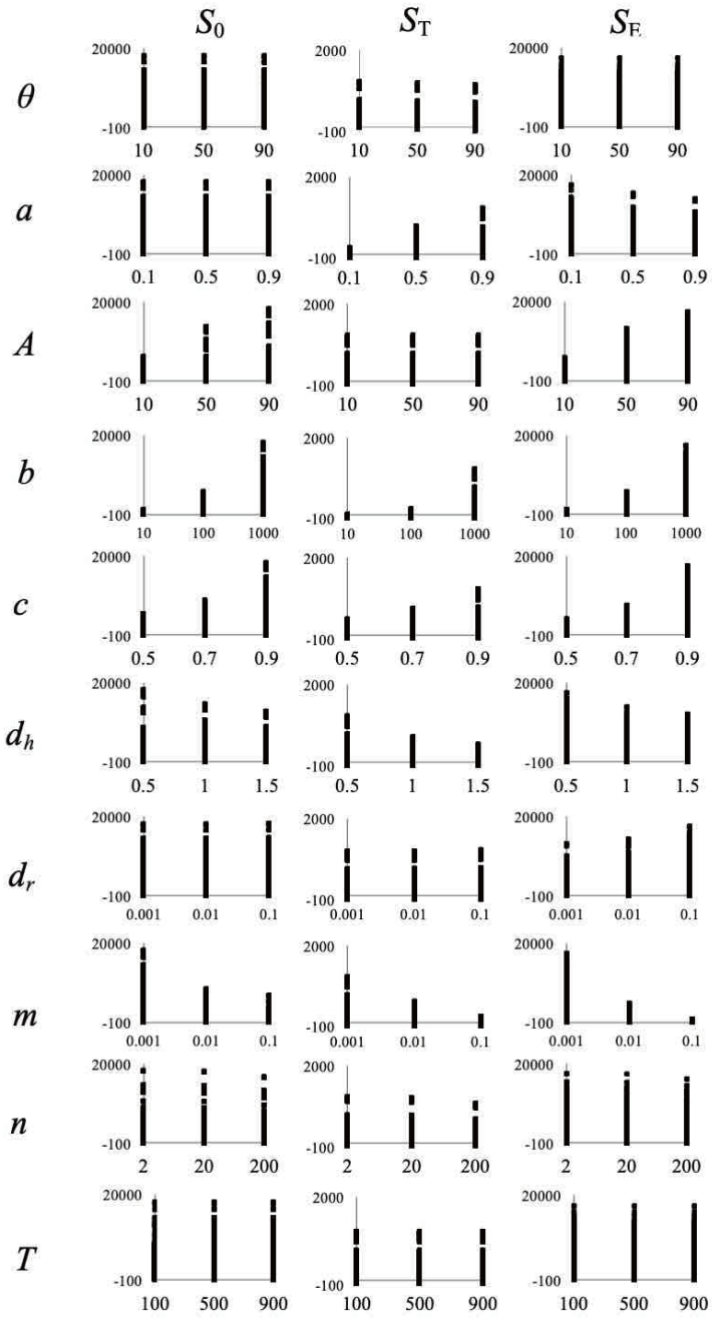

As shown in Table 1, three levels are set to each parameter and dynamics of $H(t)$ are calculated for $3^{10} = 59049$ parameter sets. The value of the relative peaks without, in and after therapy (S_0, S_T and S_E) are plotted in the graphs against three levels of parameters. Each row corresponds to each of ten parameters and S_0, S_T and S_E are plotted on the graphs in the left, middle and right column, respectively.

Figure 6 Distributions of relative peak height (S_0, S_T and S_E) and score calculated deriving parameters from uniform distribution

(A)

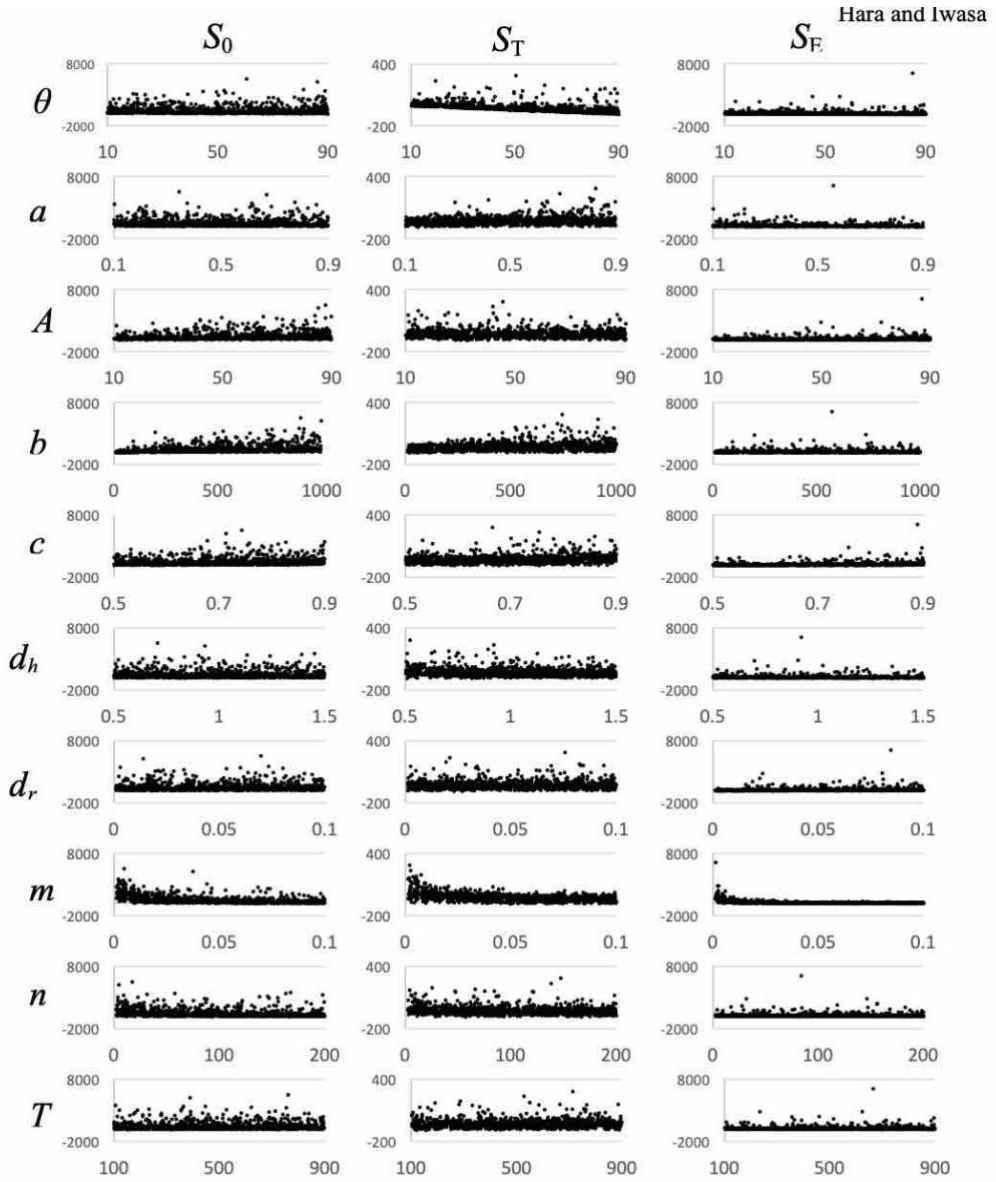

Deriving 1000 parameter sets from uniform distribution, we calculated $H(t)$ and plotted relative peak height (S_0, S_T and S_E) and score. In (A), each row corresponds to each of 10 parameters and S_0, S_T and S_E are plotted in the left, middle and right column, respectively.

(B)

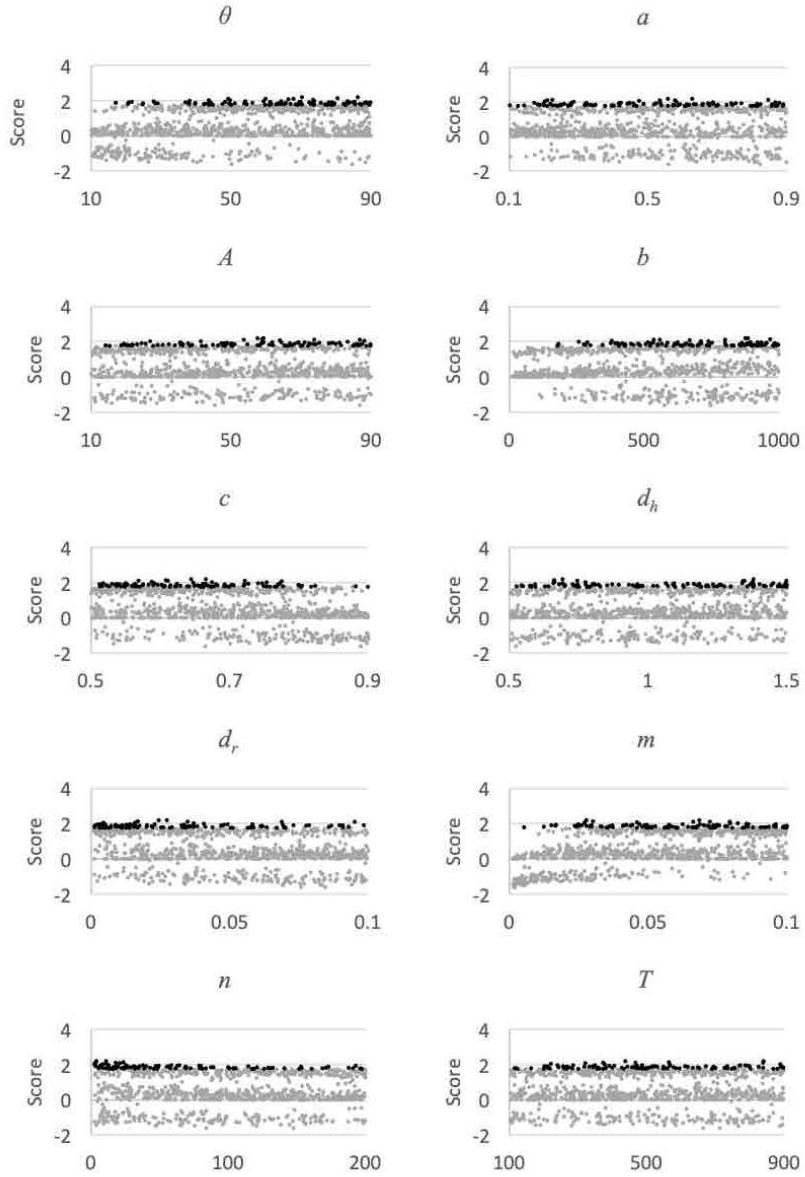

In (B), distribution of score given by Eqs. 4, 5a, b, and c are plotted. Black dots correspond to the cases which achieved top 10% high score and gray dots are 90%, the rest of the cases.

Figure 7 Percentages of the cases in which $S_0 > 0$, $S_T \leq 0$, and $S_E \leq 0$ were satisfied

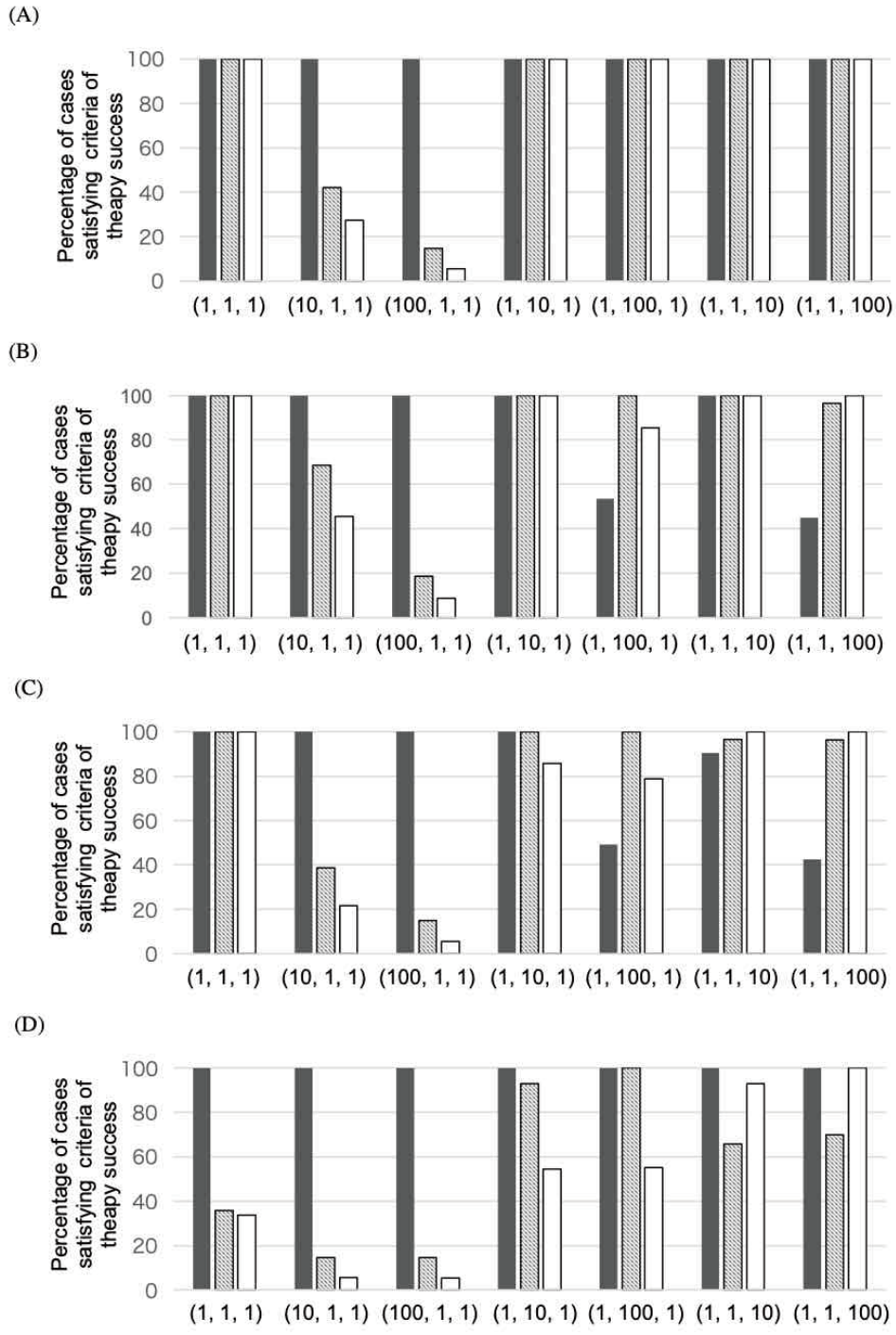

Percentages of cases in which the therapeutic success criteria $S_0 > 0$, $S_T < 0$, and $S_E < 0$ were satisfied are graphed as black bars, striped bars, and white bars, respectively. The weights of α, β, and γ are shown as w_α, w_β, and w_γ, respectively. (A) Result of runs of the

standard scoring method (Eq. 4, 5a, 5b and 5c); All runs of (w_α, w_β, w_γ) = (1, 1, 1), (1, 10, 1), (1, 100, 1), (1, 1, 10), and (1, 1, 100) satisfied all three criteria, as indicated by 100%. Runs of increasing weights for α, (10, 1, 1) and (100, 1, 1), show decreased percentages of the cases in which $S_T \leq 0$, and $S_E \leq 0$ are satisfied. (B) Result of runs of variation 1 (Eq. A.1) are shown. Runs of increasing weights for α, (10, 1, 1) and (100, 1, 1), show decreased numbers of cases satisfying $S_T \leq 0$ and $S_E \leq 0$. In cases with very large weights for β and γ, (1, 100, 1) and (1, 1, 100), the percentages of the cases satisfying $S_0 > 0$ were decreased, whereas in cases of (1, 1, 1), (1, 10, 1), and (1, 1, 10) all runs satisfied all three criteria. (C) Results of runs of variation 2 (Eq. A.2) were similar to those of variation 1. Parameter weights (w_α, w_β, w_γ) of (10, 1, 1) and (100, 1, 1) decreased numbers of cases satisfying $S_T \leq 0$ and $S_E \leq 0$, and with (1, 100, 1) and (1, 1, 100), fewer cases satisfied $S_0 > 0$. (D) Runs of variation 3 (Eq. A.2) were performed with power of 0.5 instead of 0.1 in the standard scoring. For all combinations of weights, less than 100% of cases satisfied all three criteria. With (w_α, w_β, w_γ) weights of (1, 1, 1), (10, 1, 1), and (100, 1, 1), percentages of cases that satisfied $S_T \leq 0$ and $S_E \leq 0$. were low. Increasing (w_α, w_β, w_γ) weights to (1, 10, 1), (1, 100, 1), (1, 1, 10) and (1, 1, 100) led to increased percentages of cases that satisfied $S_T \leq 0$ and $S_E \leq 0$.

Figure 8 Influence of intervals of administration

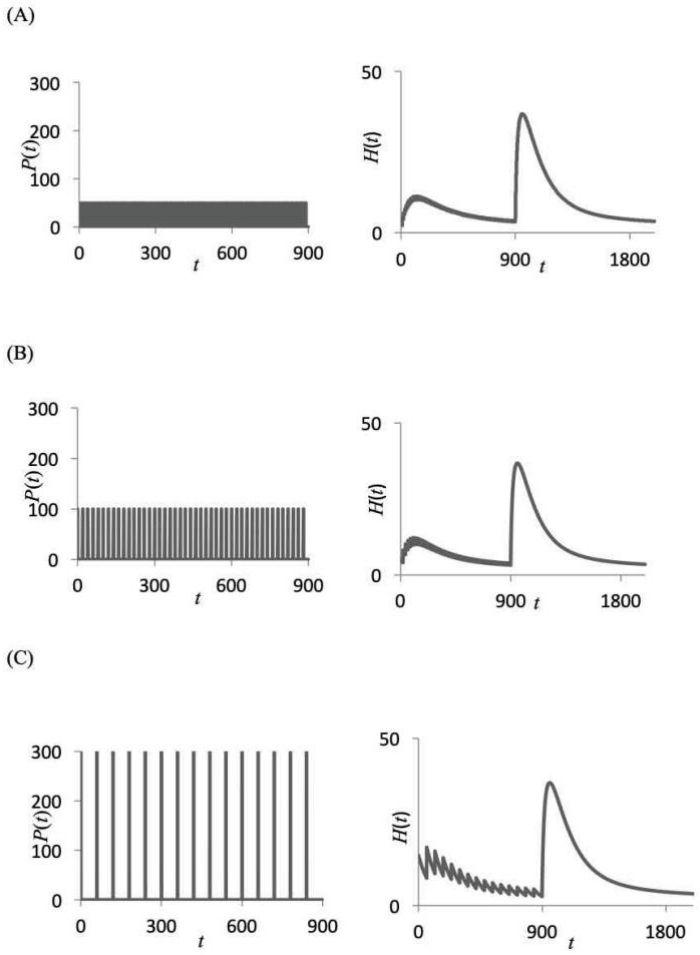

We changed the intervals of administration and examined the influence on therapeutic success. Total amounts doses were fixed at 4500 and the length of the therapy phase was $T = 900$. (A) Administration of pollen in 90 doses of 50; (B) Administration of pollen in 45 doses of 100; (C) Administration of pollen in 15 doses of 300. The left graph shows temporal patterns of administration ($P(t)$) in the therapy phase; the right graph is for $H(t)$. The values of parameters A, b, c, d_h, d_r, m, n, and T were 50.0, 10.0, 0.5, 0.01, 0.001, 0.045, 200.0, and 900.0. Peaks of $H(t)$ during therapy and after therapy were (A) $\max_{t<T} H_{\mathrm{w}}(t) = 11.275006$ and $\max_{t>T} H_{w}(t) = 36.801499$; (B) $\max_{t<T} H_{\mathrm{w}}(t) = 12.252302$ and $\max_{t>T} H_{\mathrm{w}}(t) = 36.775733$; (C) $\max_{t<T} H_{\mathrm{w}}(t) = 17.399794$ and $\max_{t>T} H_{\mathrm{w}}(t) = 36.695985$.

Figure 9 Influence of patterns in the therapy phase

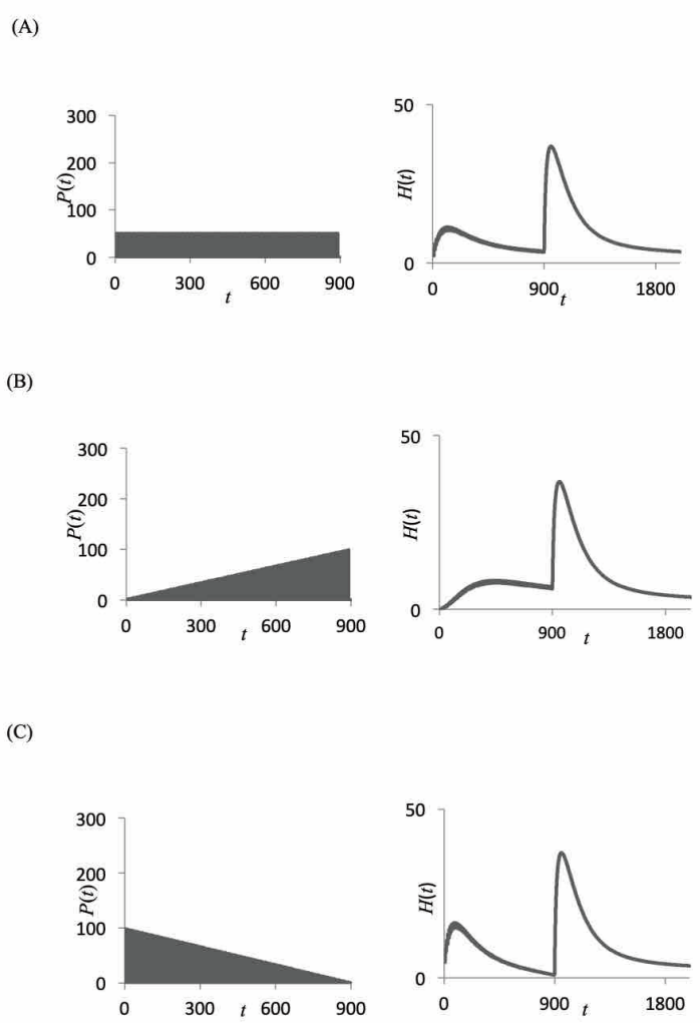

We examined the following three administration schedules: (A) 50 pollen constantly, (B) increasing administration with time in according to $a = 0.1099t$, (C) decreasing administration with time according to $a = 98.91—0.1099t$. The left graph shows changes in H(t) with time, and the right graph shows changes in $P(t)$ with time. The parameters A, b, c, d_h, d_r, m, n, and T were 50.0, 10.0, 0.5, 0.01, 0.001, 0.045, 200.0, and 900.0, respectively. Peaks of $H(t)$ in therapy and exposure phase were as follows:

(A) $\max_{t<T} H_w(t) = 11.275006$, $\max_{t>T} H_w(t) = 36.801499$; (B) $\max_{t<T} H_w(t) = 8.306327$, $\max_{t>T} H_w(t) = 36.97649$; (C) $\max_{t<T} H_w(t) = 16.31071$, $\max_{t>T} H_w(t) = 37.058121$.

Figure 10 Influence of changes in total doses during constant administration of pollen

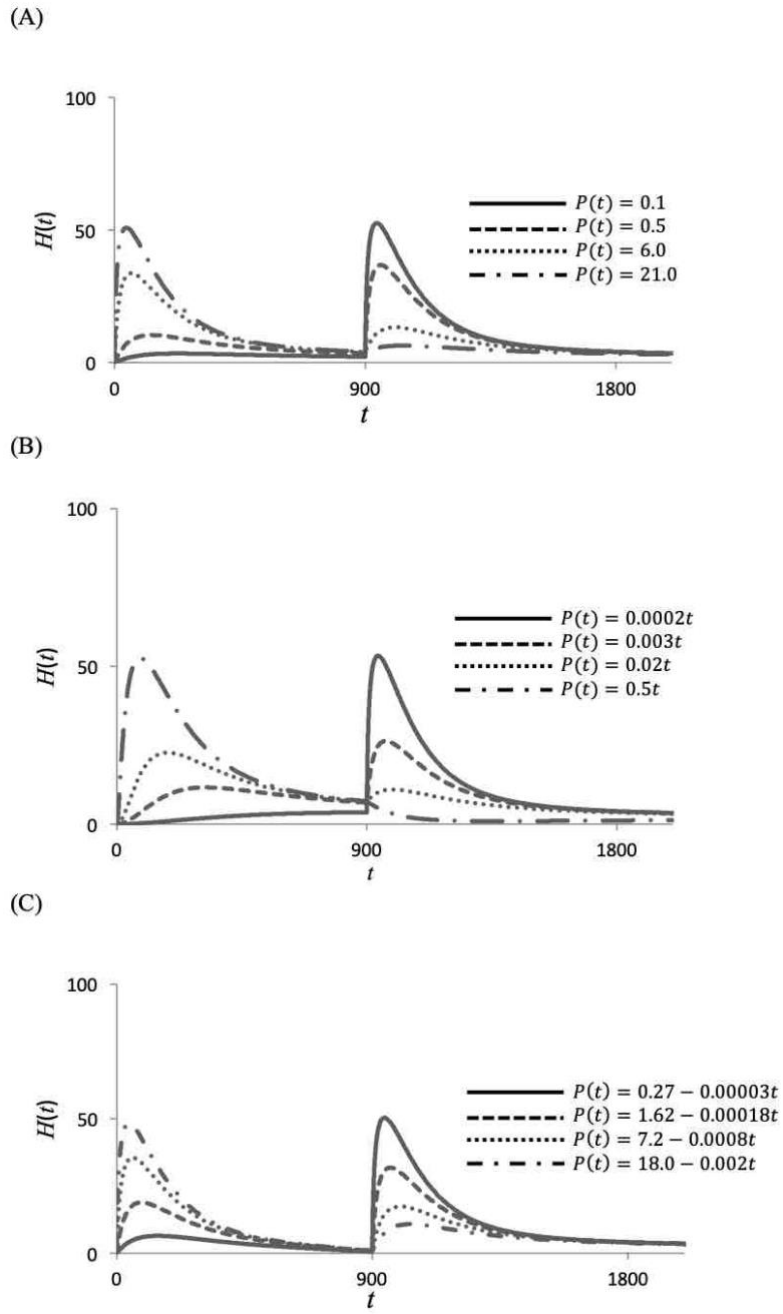

(A) Total pollen doses $P(t)$ in Eq. (3) were 0.1, 0.5, 6.0, and 21.0 and changes in $H(t)$ with time are graphed with fixed parameters A, b, c, d_h, d_r, m, n, and T of 50.0, 10.0, 0.5, 0.01, 0.001, 0.045, 200.0, and 900.0, respectively. Peaks of H(t) in therapy and exposure phases were as follows: $P(t) = 0.1$, $\max_{t<T} H_w(t) = 3.435564$ and $\max_{t>T} H_w(t) =$

52.656663; $P(t)$ = 0.5, $\max_{t<T} H_w(t)$ = 10.375391 and $\max_{t>T} H_w(t)$ = 36.828364; $P(t)$ = 6.0, $\max_{t<T} H_w(t)$ = 33.687784 and $\max_{t>T} H_w(t)$ = 13.351538; and $P(t)$ = 21.0, $\max_{t<T} H_w(t)$ = 50.844979 and $\max_{t>T} H_w(t)$ = 6.431192. (B) We represented doses as $P(t)$ = st (s > 0) and varied these with slope s values of 0.0002, 0.003, 0.02, and 0.5. Graphs show changes in $H(t)$ with time. The parameters A, b, c, d_h, d_r, m, n, and T were 50.0, 10.0, 0.5, 0.01, 0.001, 0.045, 200.0, and 900.0, respectively. Peaks of $H(t)$ in therapy and exposure phases were as follows: s = 0.0002, $\max_{t<T} H_w(t)$ =3.740696 and $\max_{t>T} H_w(t)$ = 53.367095; s = 0.003, $\max_{t<T} H_w(t)$ = 11.644834 and $\max_{t>T} H_w(t)$ = 26.332285; s = 0.02, $\max_{t<T} H_w(t)$ = 22.661222 and $\max_{t>T} H_w(t)$ = 10.94445; and s = 0.5, $\max_{t<T} H_w(t)$ = 52.591565 and $\max_{t>T} H_w(t)$ = 7.263804.

(C) We present total doses as $P(t)$ = u-st (s > 0 and u is constant) and varied the slope s at −0.00006, −0.00018, −0.0008, −0.002. Graphs show changes in $H(t)$ with time. The parameters A, b, c, d_h, d_r, m, n, and T were 50.0, 10.0, 0.5, 0.01, 0.001, 0.045, 200.0, and 900.0, respectively. Peaks of $H(t)$ in therapy and exposure phases were as follows: s = −0.00006, $\max_{t<T} H_w(t)$ = 6.45453 and $\max_{t>T} H_w(t)$ = 50.320351; s = −0.00018, $\max_{t<T} H_w(t)$ = 18.848269 and $\max_{t>T} H_w(t)$ = 31.80507; s = −0.0008, $\max_{t<T} H_w(t)$ = 35.47852 and $\max_{t>T} H_w(t)$ = 17.374652; and s = −0.002, $\max_{t<T} H_w(t)$ = 48.134032 and $\max_{t>T} H_w(t)$ = 10.789832.

Figure 11 Suppressive effects of constant and increasing pollen treatments

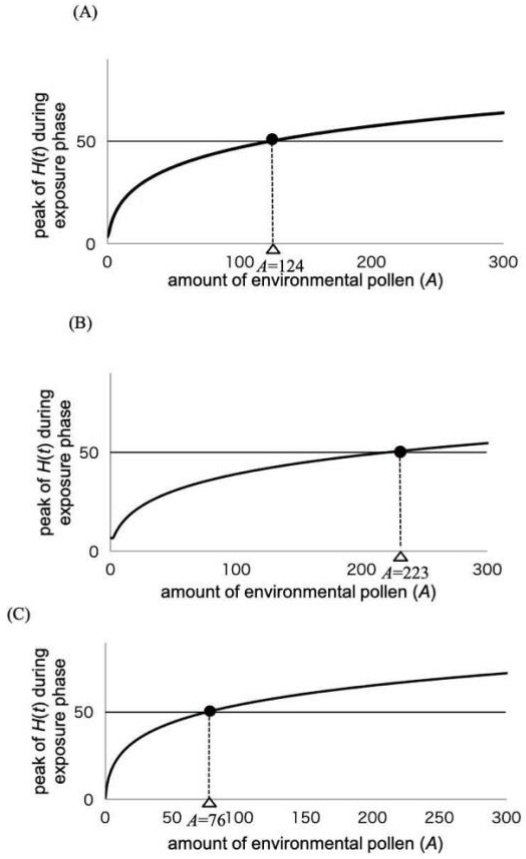

The administration schedules $P(t) = 0.4705$, $P(t) = 0.000204t$, and $P(t) = 0.5202 - 0.0000578t$ were chosen to represent constant, increasing, and decreasing doses, respectively. $H(t)$ peaks in the therapy phase were all close to 10. The vertical line shows $\max_{t>T} H_w(t)$ values and the horizontal line shows the environmental pollen exposure A. Using gradual changes in A, we determined the maximum value of A for which $\max_{t>T} H_w(t)$ was kept at less than or equal to the threshold θ. The method that achieves the larger A value should lead to better resistance to pollen exposure. (A) For $P(t) = 0.4705$, $H(t)$ reached the threshold θ at around $A = 124$, (B) for $P(t) = 0.000204t$, $H(t)$ reached the threshold θ at around $A = 223$, and (C) for $P(t) = 0.5202 - 0.0000578t$, $H(t)$ reached the threshold θ at around $A = 76$.

Chapter 2: Coupled dynamics of intestinal microbiome and immune system —A mathematical study

The study in this chapter, done in collaboration with Dr. Yoh Iwasa, was published in Journal of Theoretical Biology 464: 9–20 in 2019

Abstract

An immune system sometimes causes an exaggerated response to harmless materials, such as pollens, eggs, and metals, which is known as an allergy. The regulatory T (Treg) cells suppress such allergic responses. Recently, it has been observed that intestinal microbiota have a close association with immune systems. For example, some strains of bacteria induce Treg cells by producing short-chain fatty acids, such as butyrate. Moreover, a sufficiently diverse T cell receptor repertoire of Treg cells is required to prevent inflammation of intestine driven by the commensal intestinal microbiome. In this study, we develop a simple mathematical model describing the dynamic interaction of T helper cells, Treg cells, and Treg-inducing intestinal microbes. The proposed model may have multiple stable equilibria, and the allergic response is intense at the dysbiotic equilibrium, in which the Treg-inducing microbes are scarce. First, we search for the condition by getting rid of the stable dysbiotic steady state. Further, we examine different methods to reduce the allergic response at the equilibrium (which may be dysbiotic or non-dysbiotic). Furthermore, we discuss the possible therapeutic interventions focusing on the intestinal microbiome to suppress the allergic immune responses.

Key words: regulatory T cell; T helper cell; allergy; intestinal microbiota; dysbiosis

1. Introduction

An immune system interacts with various subsystems of a human body (Kataoka, 2016). Especially, a close interrelation between the intestinal microbiome and immune systems has been highlighted (Fujimura and Lynch, 2015). Furusawa et al. (2013) revealed that a group of human intestinal microbiomes induce regulatory T (Treg) cells by producing metabolites such as butyrate. Metabolites produced by an intestinal microbiome mediate peripheral Treg production (Arpaia et al. 2013). The Treg cells suppress exaggerated immune responses (Sakaguchi et al. 2008). Colonization of the intestinal microbiome plays a crucial role in the early stages of life, during which microbiomes have a strong effect on the development of the immune system (Gensollen et al. 2016). Drastic changes and reduction in microbiome diversity is called "dysbiosis." Dysbiosis in the neonatal and infant periods may cause dysfunction of the immune system, resulting in conditions such as asthma and atopy (Bisgaard et al. 2011; Abrahamsson et al. 2012; Arrieta et al. 2015; Fujimura et al. 2016). This suggests that the initial conditions of the intestinal microbiome have a significant impact on the development of allergic diseases.

Moreover, the intestinal microbiome may be affected by the immune system, as shown by Nishio et al. (2015). They revealed that a limited T cell receptor repertoire of Treg cells causes inflammation of intestine driven by the commensal intestinal microbiome. Treg cells play an important role of maintaining tolerance to the commensal intestinal microbiome.

A close interaction between an immune system and intestinal microbiome suggests that a suitable modification of the intestinal microbiome condition might improve the dysregulation of the immune system, such as allergy. This is supported by an experiment in which an injection of a certain strain of *Lactobacillus* sp. improved the allergic rhinitis (Ishida et al. 2005). Understanding the dynamics of interaction between the intestinal microbiome and immune system may be useful for finding a novel therapy for the dysregulation of immune systems.

In this study, we develop a simple mathematical model describing the dynamical interaction between allergy-related immune cells and intestinal microbiome. In a previous study (Hara & Iwasa, 2017), we developed a mathematical model

describing the process of differentiation of T helper (Th) cells and Treg cells. In this study, we combine the model for the immune system studied in Hara & Iwasa (2017) and a simple model for the intestinal microbiome, and discuss a possibility of mitigating excessive immune activities for an allergy by intervening the microbiome. We consider a simple mathematical model describing the dynamical interaction of Th cells, Treg cells, and Treg-inducing intestinal microbes. We here consider the abundance of Treg-inducing strains only, instead of the whole community of intestinal microbiota. The competitive/mutualistic interactions among microbiota would certainly be important for developing a therapy targeting on them, but in this first paper handling the interaction between immune system and intestinal microbiome, we focus a single variable for the Treg-inducing microbe. The model may have multiple stable equilibria, and the allergic response is intense at the dysbiotic equilibrium, in which the Treg-inducing microbes are scarce. First, we search for the condition by getting rid of the stable dysbiotic steady state. Further, we examine different methods to reduce the allergic response at the equilibrium (which may be dysbiotic or non-dysbiotic). Furthermore, we discuss the possible therapeutic interventions targeting on the intestinal microbiome to suppress the allergic immune responses. In this paper, we focus on the allergy treatments targeting on intestinal microbiome rather than those targeting on immune system itself.

2. Model

A scheme for a coupled microbe-immune system model discussed in this study is illustrated in Fig. 1. We consider the following equations:

$$\frac{dH(t)}{dt} = A \cdot b \cdot \frac{c}{1+g \cdot B(t)} \cdot \frac{1}{m(R(t)+n)} - d_h \cdot H(t), \tag{1a}$$

$$\frac{dR(t)}{dt} = A \cdot b \cdot \left(1 - \frac{c}{1+g \cdot B(t)}\right) - d_r \cdot R(t), \tag{1b}$$

$$\frac{dB(t)}{dt} = r \cdot B(t) \cdot \left(1 - \frac{B(t)}{K}\right) - f \cdot H(t) \cdot B(t). \tag{1c}$$

where $H(t)$ and $R(t)$ represent the abundances of Th and Treg cells, respectively. We focus on a fraction of the whole intestinal microbes that induce Treg cells. $B(t)$ stands for the abundance of these Treg-inducing intestinal microbes.

Eqs. (1a) and (1b) are for the immune system, which describe the

differentiation of naïve T cells to Th cells (trigger of the allergy) and to Treg cells (suppressor of the allergy), respectively, which are the same as those in our previous study (Hara and Iwasa, 2017). Reacting to the antigen, the abundance of which is denoted by A, the naïve T cells are activated by the antigen-presenting cells with the efficiency of b. The fraction $\frac{c}{1+g\cdot B(t)}$ of these cells are differentiated into Th cells and the other cells, with fraction $\left(1-\frac{c}{1+g\cdot B(t)}\right)$, are differentiated into Treg cells. c is the base level of differentiation, and $\left(1+g\cdot B(t)\right)$ corresponds to the induction of Treg cells by the intestinal microbiome (Furusawa et al. 2013). The larger the value of $g\cdot B(t)$ is, the more Treg cells and the less Th cells are produced. g indicates the induction efficiency of the Treg cells by those microbes. The denominator of the last factor in the first term of Eq. 1(a), $m(R(t)+n)$, indicates the suppression of Th cell production by Treg cells. The second terms of Eqs. 1(a) and 1(b) represent the decay of Th and Treg cells, respectively, in which d_h and d_r are the decay rates of Th and Treg cells, respectively.

Population dynamics of the intestinal microbes with Treg-induction ability (Furusawa et al. 2013) is given by Eq. 1(c). The biomass of this group of intestinal microbes follows a logistic growth. r and K represent the intrinsic rates of natural increase and carrying capacity, respectively. The second term represents the suppression of the microbes by the Th cells, and f is the reduction rate of microbes per Th cell (Nishio et al., 2015). These parameters are listed in Table 1.

In the part of an immune system (Eqs. 1(a) and 1(b)), we adopted T cell differentiation model developed by Hara and Iwasa (2017), which focused on allergen immunotherapy. Hara and Iwasa assumed that a patient takes in an extract of antigen before being exposed to massive allergen to induce Treg cells and immune tolerance. Undifferentiated immune cells are activated by the antigen taken in by the patient and then they are differentiated into Treg and Th cells. Treg cells suppress the differentiation of Th, which is represented as the last factor of the first term with the denominator including $R(t)$. The factor has a form similar to but is more simplified in Eq. (1a) than in Hara and Iwasa (2017).

Bacteria in the intestinal environment forms ecosystems in which numerous

bacterial strains cooperate and compete with each other. However, in this study, we focus on a group of Treg-inducing bacteria, the abundance of which is denoted by $B(t)$, and which follows Eq. (1c).

In this study, we focus on the intervention targeting the gut microbes, rather than direct intervention of the immune system to reduce the allergic reactions. Thus, we explore the possibility of modifying bacteria related parameters, such as *r, K, g,* and *f,* to realize the final steady state with low levels of Th cells.

3. Analysis of the model

First, we examine the non-negative steady states of the model given by Eqs. 1(a)–1(c).

In Appendix A, we analyze the equilibria of the dynamical system given by Eq. (1). There is always an equilibrium with $\hat{B} = 0$. Sometimes there exist one or more equilibria with $\hat{B} > 0$. These can be obtained by the following two relations. The first relation is given by

$$\hat{H} = c/\left[d_h m\left(g\left(\frac{1}{d_r}+\frac{n}{Ab}\right)\hat{B}+\frac{1-c}{d_r}+\frac{n}{Ab}\right)\right] . \tag{2a}$$

This is interpreted as the equilibrium level of Th cells as a result of immune dynamics, Eqs. 1(a) and 1(b), when the bacterial level is fixed at level $\hat{B}$. The second relation is given by either

$$\hat{B} = 0 \text{ or } \hat{H} = \frac{r}{f}\left(1-\frac{\hat{B}}{K}\right). \tag{2b}$$

The second equation indicate the equilibrium abundance of bacterial dynamics if the level of Th cells is maintained at a given level $\hat{H}$. A crossing point satisfying both Eqs. 2(a) and 2(b) is the equilibrium of the original three-dimensional dynamics Eq. (1).

On a plane in which horizontal axis is $\hat{B}$ and vertical axis is $\hat{H}$, we can show Eqs. 2(a) and 2(b) as a curve and a straight line (Figs. 2(A), 2(B), and 2(C)), respectively.

For the equilibrium with $\hat{B} = 0$, the other two variables are: $\hat{H} = c/\left[d_h m\left(\frac{1-c}{d_r}+\frac{n}{Ab}\right)\right]$ and $\hat{R} = \frac{Ab(1-c)}{d_r}$.

The equilibrium with $\hat{B} > 0$ can be obtained as a crossing points of a curve Eq. 2(a) and a straight-line Eq. 2(b). These are the non-negative steady states of the model given by Eqs. 1(a)–1(c).

Depending on parameter values, the model exhibits three qualitatively different behaviors, which differ in the number of positive steady states. Three different situations are illustrated in Fig. 2. These cases illustrate that the equilibrium with $\hat{B} = 0$ tends to be accompanied by a large abundance of Th cells ($\hat{H}$), whilst the equilibria with positive $\hat{B}$ correspond to the state with mild abundance of Th cells.

The local stability of these equilibria is also analyzed in Appendix A. The results of three cases are illustrated in Fig. 2, in which open circles are unstable equilibria whilst closed circles are stable equilibria (please read the derivation of these results in Appendix A). Thus, there are three cases differing in the number of equilibria:
[Case 1] Having $\hat{B} = 0$ as the only one stable steady state (Fig. 2(A)).
[Case 2] Having one positive stable steady state and another positive unstable steady state, and $\hat{B} = 0$ that is a stable steady state (Fig. 2(B)),
[Case 3] Having one positive stable steady state and $\hat{B} = 0$ that is an unstable steady state (Fig. 2(C)).

As explained earlier, the steady states with $\hat{B} = 0$, observed in Case 1 and Case 2 (black dots on the vertical axis in Figs. 2(A) and 2(B)), are associated with a very high level of Th cells (i.e. high levels of $H(t)$ in Figs. 2(A) and 2(B)). Since Th cells are triggers of allergy, we interpret these steady states with a high risk of allergy. In contrast, the equilibria with positive $\hat{B}$ tend to have mildly large Th cells (in Figs. 2(B) and 2(C)). These can be situations with a lower risk of allergy. In Case 2 and Case 3, filled circles with $\hat{B} > 0$ in Figs. 2(A) and 2(B) indicate the equilibria corresponding to healthy states.

3.1 Parameter dependence of the model

We examined parameter dependence of the equilibria of the model. We changed one of the parameters, and derived the abundances of Th cells ($\hat{H}$) and intestinal microbiome ($\hat{B}$) at equilibria, calculating the intersections of Eqs. 2(a) and 2(b). Figure 3 describes $\hat{B}$ and $\hat{H}$ in the equilibria for different value of a single parameter that is in horizontal

axis. We fixed other parameters at the values indicated in the captions to Fig. 3. The solid and dashed lines represent the branches of the stable and unstable steady states, respectively. Grey broken lines are equilibria which have negative $\hat{B}$ values.

The equilibrium with $\hat{B} = 0$ corresponds to the "dysbiosis" that means the abundance of Treg-inducing bacteria is quite low. This state is normally accompanied by a high level of $\hat{H}$, which represents a high risk of allergy development. In contrast, the steady states with a positive $\hat{B}$ is accompanied by a relatively low level of Th cells $\hat{H}$, implying that the patient has a low risk of having allergy. We examined how these two kinds of equilibria appear and disappear, when each of the parameters changes with others fixed. The results are summarized as follows:

(i) f: strength of attack on the intestinal microbiome by the Th cells
In Figs. 3(A) and 3(B), the horizontal axis represents f in the range of $0 < f < 0.001$. The model has one positive stable equilibrium and another unstable equilibrium at $\hat{B} = 0$ if f is smaller than 0.00043. At the stable equilibrium, the patients have sufficient amount of intestinal microbiome and low level of Th cells. If f is between 0.00043 and 0.00060, a positive unstable equilibrium appears and the system now has two stable equilibria: one with a positive $\hat{B}$ and another with $\hat{B} = 0$. In this case, patients may or may not have allergy depending on their initial condition. If f is greater than 0.00060, a positive equilibrium disappears and the equilibrium $\hat{B} = 0$ remains stable. In this situation, the patient always suffers allergy. This indicates that, when the strength of attack on intestinal microbiome f is very large, the patients may have dysbiotic condition in their intestine.

(ii) m: strength of suppression by Treg cells
In Figs. 3(C) and 3(D), the horizontal axis represents m in the range of $0 < m < 0.01$. When m is smaller than 0.0017, the model has one stable equilibrium $\hat{B} = 0$, which corresponds to dysbiosis of intestinal microbiome. For $0.0017 < m < 0.0023$, one unstable and one stable positive equilibria appear together with the equilibrium with $\hat{B} = 0$. The dynamics is bistable. When m is larger than about 0.0023, the model has only a single stable equilibrium with a positive $\hat{B}$. This dependence can be interpreted

as follows: When the suppression effect m is very weak, the patient suffers allergy and dysbiosis, because of the attack by Th cells cannot be suppressed by Treg cells effectively. As the strength of suppression increases, the risks of allergy and dysbiosis become reduced. When $m < 0.0017$, i.e. m is close to zero, the model developed the equilibrium with a high level of H. Even if we fail to produce the equilibrium for healthy state, enhancing m is still a useful therapeutic strategy as it mitigates the symptom at the dysbiosis equilibrium ($\hat{B} = 0$).

(iii) g: Treg induction efficiency by intestinal microbes

In Figs. 3(E) and 3(F), the horizontal axis represents g in the range of $0 < g < 0.1$. When g is smaller than about 0.066, the model has one stable equilibrium $\hat{B} = 0$, implying dysbiosis of intestinal microbiome. When g exceeds 0.066, one unstable and one stable equilibria with positive $\hat{B}$ appear and the model becomes bistable. This can be interpreted as follows: When the suppression effect of Treg g is very weak, the patient develops allergy because dysbiosis caused by Th cells cannot be prevented by Treg cells. As the fraction of Treg inducing strains increases, Treg suppression is enhanced and allergy is reduced.

(iv) r: growth rate of intestinal microbes

In Figs. 3(G) and 3(H), the horizontal axis represents r in the range of $0 < r < 0.1$. When r is below about 0.018, the model has one stable equilibrium $\hat{B} = 0$, which corresponds to dysbiosis of intestinal microbiome. For $0.018 < r < 0.023$, one unstable equilibrium and one stable equilibrium appear and the model has three equilibria (two equilibria with positive $\hat{B}$ and another with $\hat{B} = 0$). When r is larger than 0.023, the model has only one positive equilibrium that corresponds to a healthy state. When the suppression effect m is very weak, the patients have allergy and dysbiosis is caused by Th cells which cannot be suppressed by Treg cells. As the growth rate of the microbes increases, the risks of allergy and dysbiosis is reduced.

(v) K: carrying capacity of intestinal microbes

In Figs. 3(I) and 3(J), horizontal axis represents K in the range of $0 < K < 100$. When K is smaller than about 43, the model has one stable equilibrium $\hat{B} = 0$, implying dysbiosis of intestinal microbiome. When K exceeds 43, one unstable and one stable equilibria with positive $\hat{B}$ appear and the model becomes bistable. This implies that, when the carrying capacity K is very small, the abundance of Treg-inducing microbes stay low, Treg cells cannot prevent dysbiosis caused by Th cells, and the patient develops allergy. As the fraction of Treg-inducing strains increases, Treg suppression is enhanced, and the intensity of allergy is reduced.

We may summarize these results of parameter dependence as follows: Enhancing m, r and reducing f resulted in eliminating a high-risk steady state and producing a low-risk steady state for allergy development. In contrast, enhancing g and K, the unstable equilibrium keeps remained and the state having only healthy state is not realized even if these parameters becomes very large.

4. How to mitigate the allergic symptoms

Considering [Case 1], [Case 2] and [Case 3] in Section 3, we have the following two different targets for finding methods of intervention to allergy in the model.

[1] To make the dysbiotic steady state unstable

This is realized if the condition for Case 1 is satisfied, in which the system has a single stable equilibrium that has a positive $\hat{B}$. The equilibrium with $\hat{B} = 0$ exists but it is unstable. In this case, there is no dysbiotic state accompanied by high risk of allergy.

[2] To reduce the risk level of allergy at the steady state

This can be done by enhancing the effectiveness of microbe-related parameters in suppressing the allergy intensity. To mitigate allergic symptoms in the final state, we may search for parameters effective in reducing the abundance of Th cells at the steady state. We varied four parameters related to intestinal microbiome, r: growth rate, K: carrying capasity, g: induction efficiency and f: suppression effect on microbes by Th cells, which we regarded target of intervention. We investigated the levels of $H, R,$ and B at the steady states (after $t = 50000$), by extensive numerical analysis.

4.1. To make the dysbiotic steady state unstable

If the equilibrium with $\hat{B} = 0$ becomes unstable, then the system has no dysbiotic state. According to the analysis in Appendix A, this holds when the following inequality holds:

$$m\frac{d_h}{c}\left(\frac{1-c}{d_r}+\frac{n}{Ab}\right) > \frac{f}{r}. \quad (3)$$

The left-hand side represents suppression effect of Treg on Th cells. $m\frac{d_h}{c}$ represents suppression effect of Treg on Th per Th cell. $\frac{1-c}{d_r}$ is the production rate of iTreg cells relative to the decay rate of them and $\frac{n}{Ab}$ is the production rate of nTreg cells relative to that of naïve T cells. $\left(\frac{1-c}{d_r}+\frac{n}{Ab}\right)$ is the total production of iTreg and nTreg cells, and therefore the left-hand side is the product of the suppression effect of Treg per Th cells and the total production rate of Treg cells. The right-hand side represents relative reduction rate of intestinal microbiome. f and r are reduction effect and growth rate of intestinal microbiome, respectively. After all, the formula represents the condition indicating that the suppression effect of Treg cells on Th cells is larger than relative suppression effects of Th on intestinal microbiome.

4.2. To reduce the allergic reaction at the steady state

If the inequality condition (3) fails, there is a chance that the system may go to the state of $\hat{B} = 0$ which is now locally stable. In this situation, we still have several options mitigating allergies. First, even if the system converges to dysbiosis $\hat{B} = 0$, the level of Th cells might be reduced by modifying parameters. Second, even if the system converges to the non-dysbiotic state $\hat{B} > 0$, there exist some Th cells and their abundance is lower in the non-dysbiotic state than in the dysbiotic state. However, we can reduce Th cells in this non-dysbiotic equilibrium by modifying parameters. In the following, we consider these two methods.

4.2.1 Th cells at the dysbiotic equilibrium

First, concerning the dysbiotic equilibrium where $\hat{B} = 0$ holds, we can calculate the

level of Th cells explicitly, as follows:

$$\widehat{H} = c/\left[d_h m\left(\frac{1-c}{d_r} + \frac{n}{Ab}\right)\right]. \quad (4)$$

Note that Eq. (4) is independent of bacteria-related parameters (r, g, f and K). We can reduce the level of Th cells at the dysbiotic equilibrium only by modifying parameters of immune system such as m. Figure 3 illustrates how the level of helper T cells $\widehat{H}$ at the equilibrium is mitigated by reducing m at the equilibrium with higher Th level (Fig. 3(D); $m < 0.00043$). Moreover, no change in microbiome-related parameters (r, g, f and K) can mitigate the severity of allergic symptoms at the dysbiotic equilibrium (Figs 3(B), 3(F), 3(H), and 3(J)).

The right-hand side of Eq. (4) is the inverse of the left-hand side of the inequality (3), the condition for the instability of the dysbiotic equilibrium. Therefore, reducing $\widehat{H}$ in Eq. (4) makes Eq. (3) satisfied more easily. Reducing the quantity in the right-hand side would mitigate the intensity of allergy (i.e. Th level), even if the dysbiotic equilibrium remains stable (i.e. Eq. (3) is violated). However, this is irrelevant in the present study, because we here focus on the intervention of gut microbes, both the direct intervention of the immune system.

4.2.2. Abundance of Th cells at the non-dysbiotic stable state

Second, we may succeed in maintaining the system at a non-dysbiotic steady state where $\hat{B} > 0$ holds. Then, we may examine the therapy to reduce the Th cell level further to decrease the risk of allergy development.

The level of Th cells at the equilibrium $\hat{B} > 0$ can be calculated numerically. We examined the steady state for ten different levels for each of the following four parameters controlling the bacterial population dynamics and their effects to the immune system: r: growth rate, K; carrying capasity, g: Treg induction efficiency and f: suppression effect on the microbes by the Th cells. We examine the number of Th ($\widehat{H}$), Treg ($\hat{R}$) and intestinal microbiome ($\hat{B}$) after a sufficiently long time ($t = 50000$). We evaluate the magnitude of allergic symptoms by Th ($\widehat{H}$) level (Fig 4(A1), (B1)). We set the range of r from 0.01 to 0.1, the range of g from 0.01 to 0.1, the range of K from 10 to 100 and the range of f from 0.0001 to 0.001. Each combination of two parameters are chosen and we examined the effect on the values of

$\hat{H}$, $\hat{R}$ and $\hat{B}$,. The parameters except for these two were fixed as $A = 1,\ b = 1,\ c = 0.7,\ d_h = 0.1,\ d_r = 0.001,\ m = 0.001,\ g = 0.01,\ n = 1,\ K = 10,\ r = 0.01,$ and $f = 0.001$. In Fig. 4, we show $\hat{H}$, $\hat{R}$, and $\hat{B}$ at equilibrium, for several cases, in which two axes are parameters chosen among r, K, g and f with others fixed. Symbols "D" and "N", indicating dysbiotic ($\hat{B} = 0$) and non-dysbiotic ($\hat{B} > 0$) states area, respectively. Below, we explain a few cases (Figs. 4(A1)–4(A3) for r and K; Figs 4(B1)–4(B3) for g and f), and explain other graphs in Appendix B.

(i) *Effects of r and K*

Figs. 4(A1), 4(A2), and 4(A3) illustrate $\hat{H}$, $\hat{R}$, and $\hat{B}$, respectively, after $t = 50000$ for different combinations of r and K. The initial values are $(H(0), R(0), B(0)) = (25, 289, 0.01)$. When r and K are large, Th cells are suppressed ($\hat{H}$ become smaller, as shown in Fig. 4 (A1)), and Treg and microbiome abundance are enhanced ($\hat{R}$ and $\hat{B}$ become larger, as shown in Figs. 4(A2) and 4(A3)). If $r \leq 0.02$, patients have high level of Th cells (Fig. 4(A1)), corresponding to a high-risk for allergy state accompanied by dysbiosis (shown by "D" in Fig. 4(A3); $\hat{B} = 0$). In the area $r \geq 0.03$, the level of Th is low (Fig. 4 (A1)) and the number of bacteria is positive (non-dysbiosis, "N" in Fig. 4(A3)). In this non-dysbiotic state, a drastic change of $\hat{B}$ is caused by the enhancement of K (Fig. 4(A3)), and subsequently both $\hat{H}$ and $\hat{R}$ change (see Figs. 4(A1) and 4(A2)). The result indicates that the disadvantage on allergy prevention by slow growth of intestinal microbiome (low r) can be overcome by enhancing carrying capacity (low K) in the healthy state, but r needs to be larger than 0.03 to prevent from being trapped in the allergic state.

(ii) *Effects of f and g*

Figs. 4(B1), 4(B2), and 4(B3) show the value of $\hat{H}$, $\hat{R}$ and $\hat{B}$, respectively varying g and f, after $t = 50000$. The initial values are $(H(0), R(0), B(0)) = (7.29, 576, 16)$. Within the non-dysbiotic states (shown by "N" in Fig. 4(B1)), when enhancing g or reducing f, Th cells are suppressed (shown by smaller $\hat{H}$ in Fig. 4(B1)) and Treg are enhanced (shown by larger $\hat{R}$ in Fig. 4(B2)) and bacteria are enhanced (shown by larger $\hat{B}$ in Fig. 4(B3)). f is the damage to microbe by Th cells, and g is the strength

of Treg induction by the microbe. When f is large ($f \geq 0.007$), patients present dysbiotic state even if g is enhanced (Fig. 4(B3)). Microbes severely damaged by Th cells cannot induce Treg enough to suppress Th and dysbiosis.

We aim to decrease the number of Th cells $\hat{H}$ and to increase the number of Treg cells $\hat{R}$ to suppress allergic symptoms. According to the results of **(i), (ii)**, the enhanced g (the strength of induction of Treg by microbe), K (carrying capacity of microbes) and r (growth rate of microbe), and the reduced f (suppression effect on the microbes by the Th cells) achieve a low level of $\hat{H}$ and a high level of $\hat{R}$ among the healthy steady states. Lower risks of allergy development can be realized even if they have been already non-dysbiotic state (Figs. 4(A1) and 4(B1)). By running the model for different sets of initial values of Th, Treg, and bacteria, we found bistable dynamics, which is indicated in Fig. 3. However, the bistability does not change the main results explained in this section and illustrated in Fig. 4.

When we consider a method to escape from allergic states, r and f is also an important element. In Figs. 4(A1)–4(A3), when $r \leq 0.02$ holds, patients cannot escape from allergic states even if they enhance other features of microbes, g and K. Similarly, in Figs. 4(B1)–4(B3), when $f \geq 0.07$ holds, patients cannot escape from allergic states even if they enhance g and K. Note that the condition for the absence of allergic state, inequality (3) has r and f in its right-hand side but g and K are not included in (3). Only modifying r and f in these three parameters can realize the condition without allergy [Case 3] in Section 3. Results for other combinations of two parameters are explained in Appendix B.

5. Discussion

In this study, we investigated the interaction between the intestinal microbiome and immune system, and examined a possible strategy for the treatment of allergy using a simple mathematical model. We focused the intervention targeting on the intestinal microbe to reduce the allergic reaction, rather than the therapy to modify the immune system directly.

We observed that at a dysbiotic equilibrium the Treg-inducing bacteria is scarce

($\hat{B} = 0$), which may or may not be stable. The abundance of Th cells at the dysbiotic equilibrium is much larger than at the non-dysbiotic equilibrium ($\hat{B} > 0$), if the latter exists. Thus, we first studied a method to make the dysbiotic equilibrium unstable. We obtained the condition as an inequality (Eq. (3)).

Further, even if the dysbiotic equilibrium is locally stable (i.e., if Eq. (3) is violated), we might be able to reduce the abundance of Th cells at the dysbiotic equilibrium. This is given by Eq. (4), which is independent of the parameters related to the bacterial population. This implies that we cannot mitigate the intensity of allergies at the dysbiotic equilibrium by modifying the bacteria-related parameters.

Furthermore, we considered a method to reduce the Th cell abundance at the non-dysbiotic equilibrium ($\hat{B} > 0$). We performed numerical parameter-sensitivity analysis. We observed that larger values of g and K, and smaller value of f reduces the allergic reaction. Note that, even if the dysbiotic equilibrium is locally stable, we may be able to make the systems convergence to the dysbiotic equilibrium less likely, by narrowing its domain of attraction.

This study is the first step toward modeling the interaction of these two systems. The model is simplified to gain a qualitative insight of the system. Considering more quantitative analysis aiming to a clinical approach, this model has rooms for improvement.

For example, in this study, we consider $B(t)$ as a variable for the biomass of Treg-inducing intestinal microbiome (Fig. 1 and Eq. 1(c)). Thus, we explicitly consider the population of microbes, especially those producing metabolites that induce Treg cells. However, the cooperation and competition with other microbial strains may have important effects on the Treg-inducing strains and the unbalance of the intestinal microbiome may cause dysregulation of the immune system. To describe a more realistic situation, a single compartment $B(t)$ should be separated into subgroups for several strains. Some studies revealed that dysbiosis, a decrease in the microbial diversity, is a key factor that enhances the risk of some allergic diseases (Arrieta et al. 2015; Fujimura et al. 2016). Thus, predicting the changes in the composition of bacterial strains can be an important method and have significant effects on human health. To model the changes in the bacterial composition, multiple subgroups

corresponding to different strains should be considered in the model, and competition among the subgroups for limited resources in human intestine, such as nutrition and habitats, can be an important element for predicting the allergy development.

In Eq. (1a) and (1b), the abundance of Treg-inducing microbe modifies the differentiation fraction (c is modified as $c/(1+gB)$), and after this step, there is a step in which a fraction of those to be differentiated to Th are suppressed by the presence of regulatory T cells (see the first term of Eq. (1a)). In contrast, the regulatory T cells may simply change the differentiation fraction (i.e., c is modified as $c/[(1+gB)m(R+n)]$). We may consider still other forms of interaction among regulatory T cells and microbiome in the differentiation to Th cells. We need quantitative experimental study of this process. Before this becomes available, study of models with alternative mechanisms would be a useful future theoretical study.

Modeling the specificity of Th and Treg cells will be definitely important theme for clinical applications. Th cells and Treg cells are from naive T cells that have antigen specificity. However, in the present paper, we did not explicitly handle them. $H(t)$ and $R(t)$ are the subsets corresponding to a mixture of Th and Treg cells reactive to different antigens. $H(t)$ is the number of Th cells that includes both of triggers of allergy and the ones reacting to commensal intestinal bacteria. $R(t)$ is the number of Treg cells suppressing each Th subsets with reactivity to different antigens. We assume that the enhancement of Treg cells by bacteria through production of metabolites is not antigen-specific. To describe interaction with intestinal microbes more accurately, we need a mathematical model with multiple groups of Th cells and Treg cells reactive to different antigens. The effect of the T cell specificity on the allergy development and on the treatment targeting on microbiota should be important theme of future theoretical study.

Considering the parameter estimation by data fitting, the time-series data will be useful for evaluating the changes in the bacterial composition; however, the availability of sufficiently long time-series data on human intestinal microbiome is still limited at this moment. Hara et al. (2018) evaluated a method of constructing a pseudo-time series of intestinal microbiome using public data on human intestinal microbiome. Assuming that all data can be allocated on the path from non-allergic to allergic states,

they estimated the transition of the intestinal microbiome structure. This method was originally developed for gene expression dynamic analysis using single-cell RNA-seq data (Ji and Ji, 2016). Although there remain some problems in its application to the intestinal microbiome data, the pseudo time-course data is likely to become a useful tool in analyzing the data using mathematical models in the near future.

Modification of parameter ranges based on experimental data is necessary to examine the realistic behavior of a coupled system between an immune system and the intestinal microbiome, and to provide a quantitative strategy for the allergy treatment. The appearance of the three states illustrated in Fig. 2 in realistic situations should be tested using the actual parameter ranges of a human body. Especially in the intestinal microbiome, a recent study considering time-series data of the intestinal microbiome from a fecal sample will be helpful for modeling the intestinal microbiome. For example, Davis et al. (2016) sampled a fecal microbiome from a female infant weekly, and observed a rapid change in the microbiome after a transition from breast milk to cow milk. If the model is expanded to have multiple compartments for each strain, the changes in the composition of strains can be fitted using the time-series data of intestinal microbiome, which would be an important theme for a future theoretical study.

In Section 4.2, the parameters related to intestinal microbiome (r, g, K, and f) are examined with their effects on the number of Th, Treg, and intestinal microbiome after a long time. Modifying these parameters prevents us from allergy suppressing differentiation into Th cells (Fig. 4). Increasing the g parameter enhances Treg-induction efficiency, which corresponds to the enhancement of the production of metabolites, such as short-chain fatty acids that enhance Treg induction. Increasing the value of K may correspond to giving more resources to the intestinal environment; thus, then more microbe can be maintained. Increasing the value of r corresponds to making microbe grow and reproduce faster. Decreasing the value of f corresponds to reduction in attack on the intestinal microbiome by the Th cells. The surface of an intestine is covered with mucosal barriers, which is kept away from the Th cells in the inner layer of intestine. Once the mucosal layer is destroyed, microbiota invades the inner layer and inflammation is caused (Okumura and Takeda, 2017). Moreover, IgA,

produced mainly in mucosal membrane of small intestine, selectively reacts to specific proinflammatory taxa of intestinal microbiota (Macpherson et al., 2018), suggesting the importance of IgA in regulating intestinal microbiota composition. f may correspond to the barrier function of an intestine. Okumura et al. (2016) discovered a protein that suppresses bacteria invasion into an inner tissue, which would be a target of treatment in terms of protecting the intestinal microbiome from exaggerated immune responses.

Recently, the concept of "prebiotics" is proposed to improve the intestinal environment (Gibson et al. 2004). According to Gibson et al., the definition of prebiotics includes that the substances should stimulate the growth or activity of microbe associated to health and wellbeing. The concept of "probiotics" is also proposed, which is a method taking microbial feed supplement (Fuller, 1991). The effectiveness of prebiotics and probiotics on allergy suppression and immune dysregulation is under discussion (Forsberg et al. 2016; Dwivedi et al. 2016) and probiotic intervention during the neonatal age protects against asthma (Nunes et al. 2018). Planning an intervention schedule in human life is also an important point considering the practical treatment method. Prebiotics and probiotics are intervention strategies for allergy targeting on the intestinal microbiome, and their effectiveness will be evaluated using parameters such as r, g, and K. Correspondence of intervention in each parameter and pre/probiotics methods needs to be discussed in detail in future works.

Details of interaction between the peripheral immune system and intestinal microbiome needs to be studied. Arpaia et al. (2013) concluded that metabolites produced by microbiomes promote Treg production in peripheral organs, such as spleen and colon; however, another experimental study by Trompette et al. (2014) suggests that circulating the metabolites produced by microbes have an effect on dendritic cells to have impaired ability to induce type 2 Th cells. In the future work, not only Treg cells but also other immune cells such as dendritic cells, can be considered as a target of immune suppression by intestinal microbiome. We hope that the theoretical study of a simple dynamic system for interaction between the immune system and intestinal microbe, like the one studied in this study, might encourage the experimental study of their interaction leading to a novel therapeutic intervention in the near future.

Acknowledgments

This work was supported by the Grant-in-Aid for JSPS fellows (No. 18J20316) from the Japan Society for the Promotion of Science, Leave-a-Nest Grant (Metagen Intestinal-Design prize) to A.H., and also Naito Grant for the Promotion of Focused Research, the Naito Foundation to Y. I. We are grateful to Dr. Shinji Nakaoka for his helpful advice on both modeling and biological background of intestinal microbiome, and Dr. Shinji Fukuda for his encouragement as an expert of intestinal microbiome. We would like to thank the following people for their useful advices: Yusuke Kakizoe, Akira Sasaki, and members of mathematical biology laboratory of Kyushu University.

References

Abrahamsson, T. R., Jakobsson, H. E., Andersson, A. F., Bjorksten, B., Engstrand, L., Jenmalm, M. C., 2012. Low diversity of the gut microbiota in infants with atopic eczema. J Allergy Clin Immunol 129(2), 434–440, doi:10.1016/j.jaci.2011.10.025.

Arpaia, N., Campbell, C., Fan, X., Dikiy, S., van der Veeken, J., deRoos, P., Liu, H., Cross, J. R., Pfeffer, K., Coffer, P. J., Rudensky, A. Y., 2013. Metabolites produced by commensal bacteria promote peripheral regulatory T-cell generation. Nature 504, 451–5, doi:10.1038/nature12726.

Arrieta, M. C., Stiemsma, L. T., Dimitriu, P. A., Thorson, L., Russell, S., Yurist-Doutsch, S., Kuzeljevic, B., Gold, M. J., Britton, H. M., Lefebvre, D. L., Subbarao, P., Mandhane, P., Becker, A., McNagny, K. M., Sears, M. R., Kollmann, T., Mohn, W. W., Turvey, S. E., Finlay, B. B., Investigators, C. S., 2015. Early infancy microbial and metabolic alterations affect risk of childhood asthma. Sci Transl Med 7, 307ra152, doi:10.1126/scitranslmed.aab2271.

Bisgaard, H., Li, N., Bonnelykke, K., Chawes, B. L. K., Skov, T., Paludan-Muller, G., Stokholm, J., Smith, B., Krogfelt, K. A., 2011. Reduced diversity of the intestinal microbiota during infancy is associated with increased risk of allergic disease at school age. J Allergy Clin Immunol 128(3), 646–U318, doi:10.1016/j.jaci.2011.04.060.

Davis, M. Y., Zhang, H., Brannan, L. E., Carman, R. J., Boone, J. H., 2016. Rapid change of fecal microbiome and disappearance of Clostridium difficile in a colonized infant after transition from breast milk to cow milk. Microbiome 53(4), doi:10.1186/s40168-016-0198-6.

Dwivedi, M., Kumar, P., Laddha, N. C., Kemp, E. H., 2016. Induction of regulatory T cells: A role for probiotics and prebiotics to suppress autoimmunity. Autoimmun Rev 15(4), 379–392, doi:https://doi.org/10.1016/j.autrev.2016.01.002.

Forsberg, A., West, C. E., Prescott, S. L., Jenmalm, M. C., 2016. Pre- and probiotics for allergy prevention: time to revisit recommendations? Clin Exp Allergy 46(12), 1506–1521, doi:10.1111/cea.12838.

Fujimura, K. E., Lynch, S. V., 2015. Microbiota in allergy and asthma and the emerging relationship with the gut microbiome. Cell Host Microbe 17, 592–602, doi:10.1016/j.chom.2015.04.007.

Fujimura, K. E., Sitarik, A. R., Havstad, S., Lin, D. L., Levan, S., Fadrosh, D., Panzer, A. R., LaMere, B., Rackaityte, E., Lukacs, N. W., Wegienka, G., Boushey, H. A., Ownby, D. R., Zoratti, E. M., Levin, A. M., Johnson, C. C., Lynch, S. V., 2016. Neonatal gut microbiota associates with childhood multisensitized atopy and T cell differentiation. Nat Med 22, 1187–1191, doi:10.1038/nm.4176.

Fuller, R., 1991. Probiotics in human medicine. Gut 32, 439–42.

Furusawa, Y., Obata, Y., Fukuda, S., Endo, T. A., Nakato, G., Takahashi, D., Nakanishi, Y., Uetake, C., Kato, K., Kato, T., Takahashi, M., Fukuda, N. N., Murakami, S., Miyauchi, E., Hino, S., Atarashi, K., Onawa, S., Fujimura, Y., Lockett, T., Clarke, J. M., Topping, D. L., Tomita, M., Hori, S., Ohara, O., Morita, T., Koseki, H., Kikuchi, J., Honda, K., Hase, K., Ohno, H., 2013. Commensal microbe-derived butyrate induces the differentiation of colonic regulatory T cells. Nature 504, 446–50, doi:10.1038/nature12721.

Gensollen, T., Iyer, S. S., Kasper, D. L., Blumberg, R. S., 2016. How colonization by microbiota in early life shapes the immune system. Science 352, 539–544, doi:10.1126/science.aad9378.

Gibson, G. R., Probert, H. M., Loo, J. V., Rastall, R. A., Roberfroid, M. B., 2004. Dietary modulation of the human colonic microbiota: updating the concept of prebiotics. Nutr Res Rev 17, 259–75, doi:10.1079/NRR200479.

Hara, A., Iwasa, Y., 2017. When is allergen immunotherapy effective? Journal of Theoretical Biology 425, 23–42, doi:10.1016/j.jtbi.2017.04.030.

Hara, A., Nakaoka, S., Aihara, K., 2018. Big-data analysis of allergy associations with gut microbiota. SEISAN KENKYU 70, 141–144, doi:10.11188/seisankenkyu.70.141.

Ishida, Y., Nakamura, F., Kanzato, H., Sawada, D., Hirata, H., Nishimura, A., Kajimoto, O., Fujiwara, S., 2005. Clinical effects of Lactobacillus acidophilus strain L-92 on perennial allergic rhinitis: a double-blind, placebo-controlled study. J Dairy Sci 88, 527–33, doi:10.3168/jds.S0022-0302(05)72714-4.

Ji, Z., Ji, H., 2016. TSCAN: Pseudo-time reconstruction and evaluation in single-cell RNA-seq analysis. Nucleic Acids Research 44, e117–e117, doi:10.1093/nar/gkw430.

Kataoka, K., 2016. The intestinal microbiota and its role in human health and disease. Journal of Medical Investigation 63, 27–37, doi:10.2152/jmi.63.27.

Macpherson, A. J., Yilmaz, B., Limenitakis, J. P., Ganal-Vonarburg, S. C., 2018. IgA Function in Relation to the Intestinal Microbiota. Annu Rev Immunol 36, 359-381, doi:10.1146/annurev-immunol-042617-053238.

Nishio, J., Baba, M., Atarashi, K., Tanoue, T., Negishi, H., Yanai, H., Habu, S., Hori, S., Honda, K., Taniguchi, T., 2015. Requirement of full TCR repertoire for regulatory T cells to maintain intestinal homeostasis. Proc Natl Acad Sci U S A 112, 12770–5, doi:10.1073/pnas.1516617112.

Nunes, C. F., Nogueira, J. S., Vianna, P. H. O., Ciambarella, B. T., Rodrigues, P. M., Miranda, K. R., Lobo, L. A., Domingues, R., Busch, M., Atella, G. C., Vale, A. M., Bellio, M., Nobrega, A., Canto, F. B., Fucs, R., 2018. Probiotic treatment during neonatal age provides optimal protection against experimental asthma through the modulation of microbiota and T cells. International Immunology 30, 155–169, doi:10.1093/intimm/dxy011.

Okumura, R., Takeda, K., 2017. Roles of intestinal epithelial cells in the maintenance of gut homeostasis. Exp Mol Med 49, e338, doi:10.1038/emm.2017.20.

Okumura, R., Kurakawa, T., Nakano, T., Kayama, H., Kinoshita, M., Motooka, D., Gotoh, K., Kimura, T., Kamiyama, N., Kusu, T., Ueda, Y., Wu, H., Iijima, H., Barman, S., Osawa, H., Matsuno, H., Nishimura, J., Ohba, Y., Nakamura, S., Iida, T., Yamamoto, M., Umemoto, E., Sano, K., Takeda, K., 2016. Lypd8 promotes the segregation of flagellated microbiota and colonic epithelia. Nature 532, 117–21, doi:10.1038/nature17406.

Sakaguchi, S., Yamaguchi, T., Nomura, T., Ono, M., 2008. Regulatory T cells and immune tolerance. Cell 133, 775–787, doi:10.1016/j.cell.2008.05.009.

Trompette, A., Gollwitzer, E. S., Yadava, K., Sichelstiel, A. K., Sprenger, N., Ngom-Bru, C., Blanchard, C., Junt, T., Nicod, L. P., Harris, N. L., Marsland, B. J., 2014. Gut microbiota metabolism of dietary fiber influences allergic airway disease and hematopoiesis. Nat Med 20, 159–66, doi:10.1038/nm.3444.

Appendix A

1. Number of equilibria

We find three types of different cases depending on the number of equilibria, as illustrated in Figs. 2(A), 2(B), and 2(C), respectively. The following are the details of this derivation:

Let $(\hat{H},\ \hat{R},\ \hat{B})$ be the equilibrium of the dynamics (Eqs. 1(a), 1(b), and 1(c)). Further, it satisfies the following equations:

$$\hat{H} = \frac{Ab}{d_h m} \cdot \frac{c}{(1+g\hat{B})(\hat{R}+n)} \quad , \tag{A.1a}$$

$$\hat{R} = \frac{Ab}{d_r}\left(1 - \frac{c}{1+g\hat{B}}\right) \quad , \tag{A.1b}$$

$$r\hat{B}\left(1 - \frac{\hat{B}}{K}\right) = f\hat{H}\hat{B} \quad . \tag{A.1c}$$

By eliminating $\hat{R}$, we obtain the following equation from Eqs. (A.1a) and (A.1b):

$$\hat{H} = c/\left[d_h m\left(g\left(\frac{1}{d_r} + \frac{n}{Ab}\right)\hat{B} + \frac{1-c}{d_r} + \frac{n}{Ab}\right)\right] . \tag{A.2}$$

From Eq. A.1(c), we have $\hat{B} = 0$ or

$$\hat{H} = \frac{r}{f}\left(1 - \frac{\hat{B}}{K}\right) \quad . \tag{A.3}$$

[1] For the equilibria without bacterium ($\hat{B} = 0$), the other two variables are: $\hat{H} = c/\left[d_h m\left(\frac{1-c}{d_r} + \frac{n}{Ab}\right)\right]$ and $\hat{R} = \frac{Ab(1-c)}{d_r}$.

In Fig. 2, we plot the phase plane with $\hat{H}$ as vertical axis and $\hat{B}$ as horizontal axis. This equilibrium is the intersection of the curve (A.2) and $\hat{H}$ axis (indicating $\hat{B} = 0$).

[2] For the equilibria with some bacteria ($\hat{B} > 0$), the value of Th cells and the bacteria abundance at the equilibrium can be obtained from Eqs. (A.2) and (A.3), respectively. In Fig. 2, these equilibria are graphically obtained as intersections of the curve (A.2) and the line (A.3) or $\hat{H}$ axis (indicating $\hat{B} = 0$). As $\hat{B}$ increases, the value of $\hat{H}$ starts from a positive value $\hat{H} = r/f$ with $\hat{B} = 0$, decreases at a decelerating rate, and finally converges to $\hat{H} = 0$ when $\hat{B}$ becomes very large. The curve has a negative slope and is convex downward. The curve can have three, two, one, or zero interactions

with the straight line (A.3). The value of $\hat{B}$ can be obtained as positive roots of the following quadratic equation:

$$\left(1-\frac{\hat{B}}{K}\right)\left(g\left(\frac{1}{d_r}+\frac{n}{Ab}\right)\hat{B}+\frac{1-c}{d_r}+\frac{n}{Ab}\right)=\frac{fc}{rd_hm} \quad . \tag{A.4}$$

Together with the equilibrium with $\hat{B}=0$, we have the following three cases differing in the number of equilibria as explained in the text.

2. Local stability of the equilibria

The local stability of the equilibrium can be calculated from the eigenvalues of the Jacobian of the dynamics evaluated at the equilibrium. The elements of the Jacobian are as follows:

$\frac{\partial}{\partial H}\left(\frac{dH}{dt}\right)=-d_h$, $\frac{\partial}{\partial R}\left(\frac{dH}{dt}\right)=\frac{Abc(-1)}{m(1+g\hat{B})(\hat{R}+n)^2}$, $\frac{\partial}{\partial B}\left(\frac{dH}{dt}\right)=\frac{Abcg(-1)}{m(1+g\hat{B})^2(\hat{R}+n)}$, $\frac{\partial}{\partial H}\left(\frac{dR}{dt}\right)=0$,

$\frac{\partial}{\partial R}\left(\frac{dR}{dt}\right)=-d_r$, $\frac{\partial}{\partial B}\left(\frac{dR}{dt}\right)=\frac{Abcg}{(1+g\hat{B})^2}$, $\frac{\partial}{\partial R}\left(\frac{dB}{dt}\right)=0$.

The two other elements are expressed differently when $\hat{B}=0$ and $\hat{B}>0$.

[1] For the equilibrium with $\hat{B}=0$

When $\hat{B}=0$ holds at the equilibrium, we have $\frac{\partial}{\partial R}\left(\frac{dB}{dt}\right)=0$. Thus, all the three sub-diagonal elements of the Jacobian are zero. Therefore, the eigenvalues are: $-d_h$, $-d_r$, and $\frac{\partial}{\partial B}\left(\frac{dB}{dt}\right)=r-f\hat{H}$. Consequently, the equilibrium is stable if $\hat{H}>r/f$. It is unstable if $\hat{H}<r/f$. Using $\hat{H}=c/\left[d_hm\left(\frac{1-c}{d_r}+\frac{n}{Ab}\right)\right]$ at the equilibrium, we have:

$$\text{The equilibrium is unstable if } \frac{f}{r}<\frac{md_h}{c}\cdot\left(\frac{n}{Ab}+\frac{1-c}{d_r}\right), \tag{A.5}$$

and is stable if the opposite inequality holds. This corresponds to Eq. (2) in text.

[2] For the equilibrium with $\hat{B}>0$

For the equilibrium with $\hat{B}>0$, we have the following Jacobian:

$$M=\begin{pmatrix} -d_h & \frac{Abc(-1)}{m(1+g\hat{B})(\hat{R}+n)^2} & \frac{Abcg(-1)}{m(1+g\hat{B})^2(\hat{R}+n)} \\ 0 & -d_r & \frac{Abcg}{(1+g\hat{B})^2}, \\ -f\hat{B} & 0 & -\frac{r}{K}\hat{B} \end{pmatrix}. \tag{A.6}$$

The characteristic function is $\varphi(\lambda)=det\|\lambda I-M\|$. It is expressed as follows:

$$\varphi(\lambda) = (\lambda + d_h)(\lambda + d_r)\left(\lambda + \frac{r}{K}\hat{B}\right)$$
$$-f\hat{B}\frac{Abcg}{m(1+g\hat{B})^2(\hat{R}+n)}(\lambda + d_r) - f\hat{B}\frac{A^2b^2c^2g}{m(1+g\hat{B})^3(\hat{R}+n)^2}. \quad \text{(A.7)}$$

The equilibrium is stable if all the roots of the characteristic equation $\varphi(\lambda) = 0$ have negative real parts. One necessary condition for this is $\varphi(0) > 0$. If the opposite inequality $\varphi(0) < 0$ holds, there exists at least one real positive root, which makes the equilibrium unstable (because $\varphi(\infty) < \infty$). It is

$d_h d_r \frac{rm}{fKg} < \frac{Abcd_r}{(1+g\hat{B})^2(\hat{R}+n)} + \frac{A^2b^2c^2}{(1+g\hat{B})^3(\hat{R}+n)^2}$. Using (A.1a) and (A.1b), we can rewrite the right-hand side of this inequality as $\frac{\hat{H}^2{d_r}^2m^2}{c}\left(\frac{1}{d_r} + \frac{n}{Ab}\right)$. Thus, we have

$$\varphi(0) < 0 \text{ is equivalent to } \frac{r}{fK} < \frac{\hat{H}^2 d_h mg}{c}\left(\frac{1}{d_r} + \frac{n}{Ab}\right). \quad \text{(A.8)}$$

We observe that this inequality is closely related to the slope of the curve (Eq. (A.2)) and the straight line (Eq. (A.3)) at the corresponding intersection on the $(\hat{B}, \hat{H})$-plane (see Fig. 2##). Note that the slope of the straight line (Eq. (A.3)) is

$$\left(\frac{d\hat{H}}{d\hat{B}}\right)_{\text{(A.3)}} = -\frac{r}{fK},$$

and the slope of the curve (Eq. (A.2)) is

$$\left(\frac{d\hat{H}}{d\hat{B}}\right)_{\text{(A.2)}} = \frac{(-1)cg\left(\frac{1}{d_r}+\frac{n}{Ab}\right)}{d_h m\left(g\left(\frac{1}{d_r}+\frac{n}{Ab}\right)\hat{B}+\frac{1-c}{d_r}+\frac{n}{Ab}\right)^2}.$$

Using Eq. A.1(a), we can rewrite the right-hand side as $(-1)\frac{\hat{H}^2 d_h mg}{c}\left(\frac{1}{d_r} + \frac{n}{Ab}\right)$. Thus, the inequality (A.8) is equivalent to that the slope of the straight line is sharper (more strongly negative) than the slope of the curve. Furthermore, we can conclude that $\varphi(0) < 0$ holds for the equlibrium with positive but smaller $\hat{B}$ when there are two equilibria with $\hat{B} > 0$ (i.e. Case 1). This equilibrium is unstable because it has at least one positive eigenvalue of Jacobi matrix.

Similarly, the opposite inequality $\varphi(0) > 0$ holds for the positive equilibrium with a larger $\hat{B}$ when there are two positive equilibria (Case 1), and for the equilibrium with a positive $\hat{B}$ when there is a single equilibrium with $\hat{B} > 0$ (Case 2). However, we cannot conclude the stability of these equilibria because $\varphi(0) > 0$ is only a

necessary condition for the stability. In all the cases examined in this study, we observed that the positive equilibria are locally stable, which is checked by numerical calculation as far as we examined.

Appendix B

We calculated the equilibria of $\hat{H}$, $\hat{R}$, and $\hat{B}$ and explained how they depend on parameters g, r, K, and f. In Section 4.2, two figures are presented for the combination of r and K (Figs. 4(A1)–4(A3)) and combination of g and f (Figs. 4(B1)–4(B3)). In this section, we present the rest of the figures representing other combinations of parameters. The implications of these results are similar to those discussed in Section 4.2 in text: Low r and high f are likely to cause a dysbiotic state (Figs. 5(B1)–5(B3) and 5(C1)–5(C3)).

(i) *Effects of g and K*

Figs. 5(A1), 5(A2), and 5(A3) show the value of $\hat{H}$, $\hat{R}$, and $\hat{B}$, respectively varying g and K, after $t = 50000$. The initial values are $(H(0), R(0), B(0)) = (7.29, 576, 16)$. Within the non-dysbiotic states (labeled as "N"), when enhancing g or K, the Th cells are suppressed (smaller $\hat{H}$, Fig. 5(A1)) and the Treg cells are enhanced (larger $\hat{R}$, Fig. 5(A2)). In terms of abundance of the intestinal microbiome $\hat{B}$, a change in K has a larger effect than a change in g (Fig. 5(A3)). Changing K from 10–100 have drastic effects on the abundance of the intestinal microbiome; however, the effects are not directly reflected by the number of Th cells (Fig. 5(A1)). K is the microbial biomass that is to be stably maintained in the intestinal environment, and g is the strength of Treg induction by the microbes. K has a direct effect on the number of microbe $\hat{B}$ (Fig. 5(A3)), but a few microbes (low K) can induce many Treg cells if the Treg induction by each bacterium is strong (i.e., high g) (Figs. 5(A1) and 5(A2)).

(ii) *Effects of g and r*

Figs. 5(B1), 5(B2), and 5(B3) show the value of $\hat{H}$, $\hat{R}$, and $\hat{B}$, respectively, after $t = 50000$ for different combinations of g and r. The initial values are $(H(0), R(0), B(0)) = (25, 289, 0.01)$. If $r \leq 0.02$, the patients are in the condition of dysbiosis (Fig. I; $\hat{B} = 0$) and show a high Th level, indicating a dysbiotic state (Fig.

5(B1)). If $r \geq 0.03$, the patients are in the non-dysbiotic state (N) with a lower Th level, compared to the case of $r \leq 0.02$ (Fig. 5(B1)), and they have a positive abundance of Treg-inducing bacteria (Fig. 5(B3)). In the non-dysbiotic states, the Th cells are suppressed when g and r are enhanced (Fig. 5(B1)). As g increases, the Th level ($\hat{H}$) is suppressed (Fig. 5(B1)) and the Treg level ($\hat{R}$) is enhanced (Fig. 5(B2)). Drastic changes in the numbers of Th and Treg cells (Figs. 5(B1) and 5(B2)) are caused by enhanced g rather than enhanced r. In contrast, $\hat{B}$ did not change much in response to the change in g (Fig. 5(B3)). r represents the intrinsic rate of natural increase of microbe, or the growth speed of $B(t)$. Figs. 5(B1) and 5(B2) illustrate that the growth rate of microbe (r) has less effect on the Th and Treg cells than the induction efficiency of Treg (g), which indicates that the disadvantage of slowly growing microbe can be overcome if it has a high Treg-induction efficiency. In addition, r should be larger than 0.02 to avoid dysbiosis and allergy.

(iii) *Effects of K and f*

Figs. 5(C1), 5(C2), and 5(C3) show the value of $\hat{H}$, $\hat{R}$, and $\hat{B}$, respectively for varying K and f, after $t = 50000$. The initial values are $(H(0), R(0), B(0)) = (7.29, 576, 16)$. Within the non-dysbiotic states, when enhancing K or reducing f, the Th cells are suppressed (shown as smaller $\hat{H}$ in Fig. 5(C1)), the Treg cells are enhanced (shown as larger $\hat{R}$, in Fig. 5(C2)), and the bacteria are enhanced (shown as larger $\hat{B}$ in Fig. 5(C3)). When f is large ($f \geq 0.007$), patients are present in the dysbiotic state, even if K is enhanced (Fig. 5(C3)). Even if the carrying capacity of the bacteria is large, they are driven away if exposed to a strong attack by the Th cells.

(iv) *Effects of r and f*

Figs. 5(D1), 5(D2), and 5(D3) show the value of $\hat{H}$, $\hat{R}$ and $\hat{B}$, respectively, varying r and f, after $t = 50000$. The initial values are $(H(0), R(0), B(0)) = (7.29, 576, 16)$. Within the non-dysbiotic states, when enhancing r or reducing f, the Th cells are suppressed (shown as smaller $\hat{H}$ in Fig. 5(D1)), the Treg cells are enhanced (shown as larger $\hat{R}$ in Fig. 5(D2)) and the bacteria are enhanced (shown as larger $\hat{B}$ in Fig. 5(D3)). The dysbiotic state appears when r is small and f is large. By enhancing r

(to be $r \geq 0.02$) or reducing f (to be $f \leq 0.004$), patients can exit from the dysbiotic state and achieve the non-dysbiotic state. The disadvantage of strong suppression by Th on bacteria (high level of f) can be compensated by enhancing the growth rate of bacteria (enhance r); and the disadvantage of slow growth of bacteria (low level of r) can be compensated by reducing Th attacks (reduce f).

Table

Table 1 Parameters in the model

Parameters included in the model are listed with their symbols, names, and units. "Cell", "Bacteria," and "Antigen" are the units of Th and Treg cells, intestinal microbes, and antigens, respectively.

Symbol	Name	Unit
$B(t)$	Number of bacteria	Bacteria
$H(t)$	Number of Th2 (indicator of allergic symptom)	Cell
$R(t)$	Number of iTreg cells	Cell
A	Amount of antigen	Antigen/Day
b	Sensitivity of naive T cells differentiate into Th or Treg cells	Cell/Antigen
c	Base level of differentiation into Th cells	1
d_h	Decay rate of Th cells	1/Day
d_r	Decay rate of iTreg cells	1/Day
m	Suppression effect by Treg	1/Cell
n	Number of nTreg cells	Cell
g	Treg induction efficiency	1/Bacteria
f	Suppression effect on bacteria	1/(Cell・Day)
r	Growth rate of bacteria	1/Day
K	Carrying capacity of bacteria	Bacteria

Figures

Figure 1

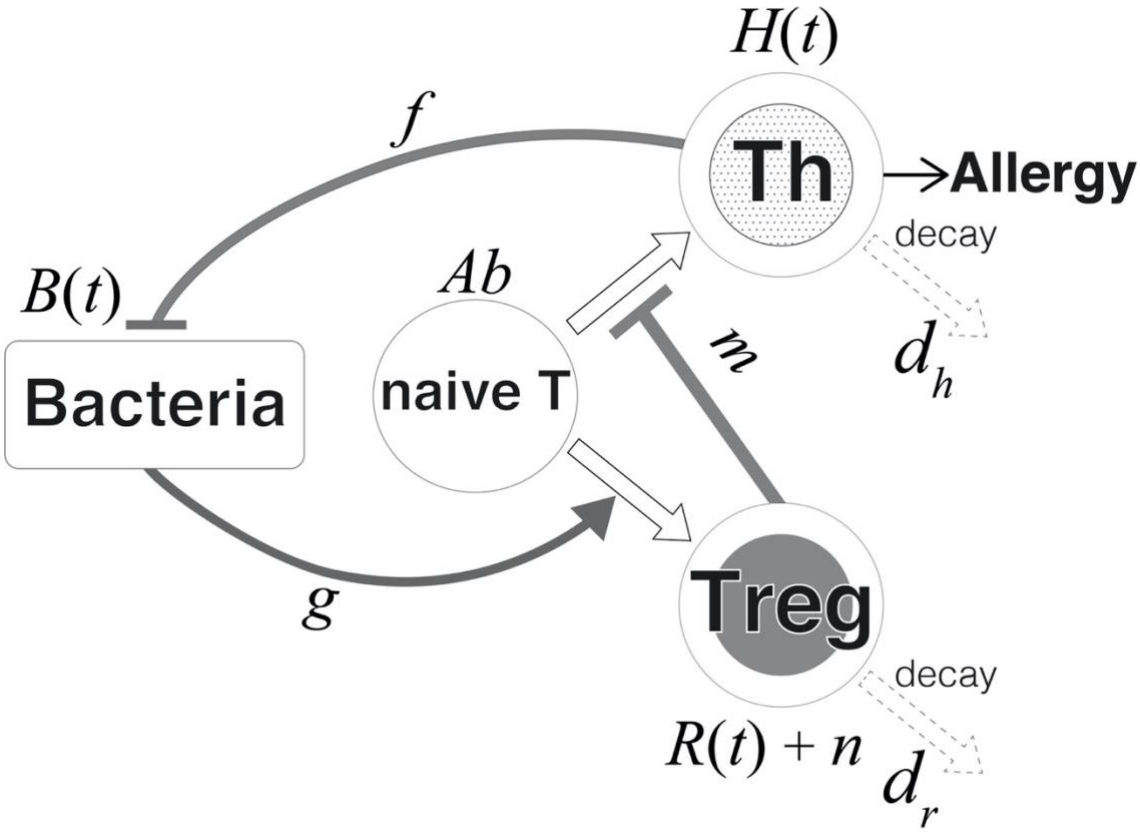

Scheme of the model. Allergen particles are presented to the naïve T cells (Th0), which subsequently produce *Ab* differentiated T cells. Fraction $\frac{c}{1+g\cdot B(t)}$ of the naïve T cells differentiates into Th cells, and fraction $\left(1-\frac{c}{1+g\cdot B(t)}\right)$ differentiates into Treg cells. $\left(1+g\cdot B(t)\right)$ corresponds to the induction of Treg cells by the intestinal microbiome and g indicates the induction strength of Treg cells. The Th and Treg cells have decay rates of d_h and d_r, respectively. The total number of naturally occurring regulatory T (nTreg) cells is indicated by n. f is the reduction rate of microbes per Th cell.

Figure 2

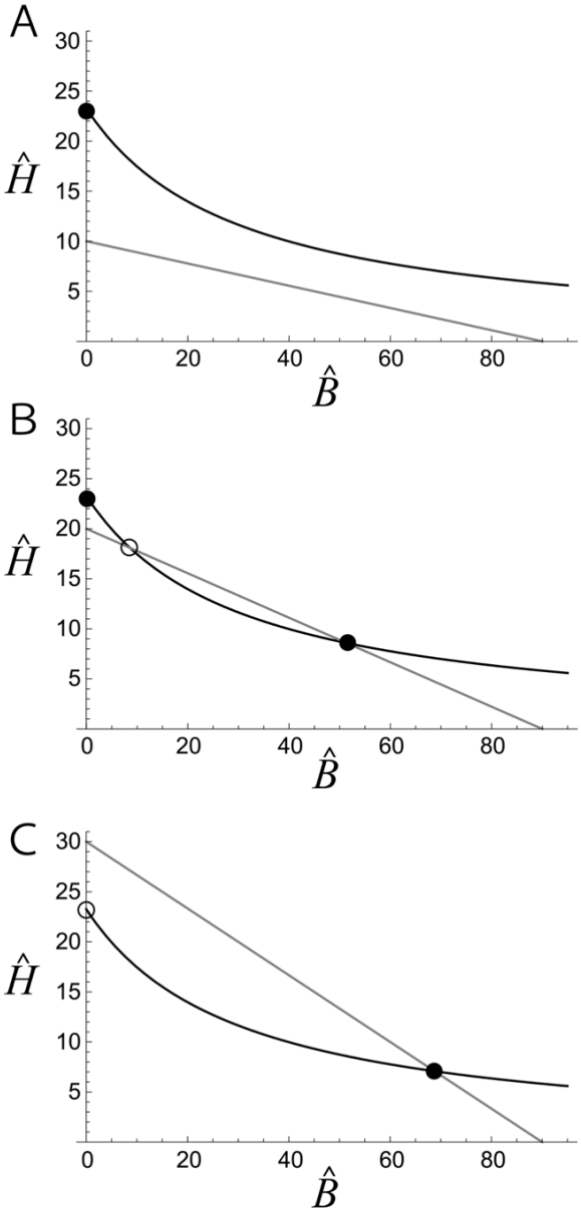

Three cases with different number of equilibria. The vertical axis corresponds to $\hat{H}$ (equilibrium level of the Th cells) and horizontal axis corresponds to $\hat{B}$ (equilibrium level of the intestinal microbiome). The growth rate of bacteria is indicated by r, which is varied among the three figures, and the other parameters are fixed as $A = 1, b = 1, c = 0.7, d_h = 0.1, d_r = 0.001, m = 0.001, g = 0.01, n = 1, K = 90, and\ f = 0.001$. The black curves represent Eq. 2(a) in text, indicating the equilibrium Th level for a given Treg-inducing microbe level $\hat{B}$. The grey straight lines represent Eq. 2(b) in text, indicating the equilibrium bacterial level for a given immune activity. Their intersections are the equilibria of the dynamics (Eq. (1)). The solid circles represent stable equilibria, and the open circles represent unstable equilibria. According to the number of equilibria, we classified the following three cases: (A) [Case 1] $r = 0.01$, with $\hat{B} = 0$ as the only stable steady state. (B) [Case 2] $r = 0.02$, with one positive stable steady state and another positive unstable one, in which $\hat{B} = 0$ is the stable steady state. (C) [Case 3] $r = 0.03$, with one positive stable steady state and $\hat{B} = 0$ is the unstable steady state.

Figure 3

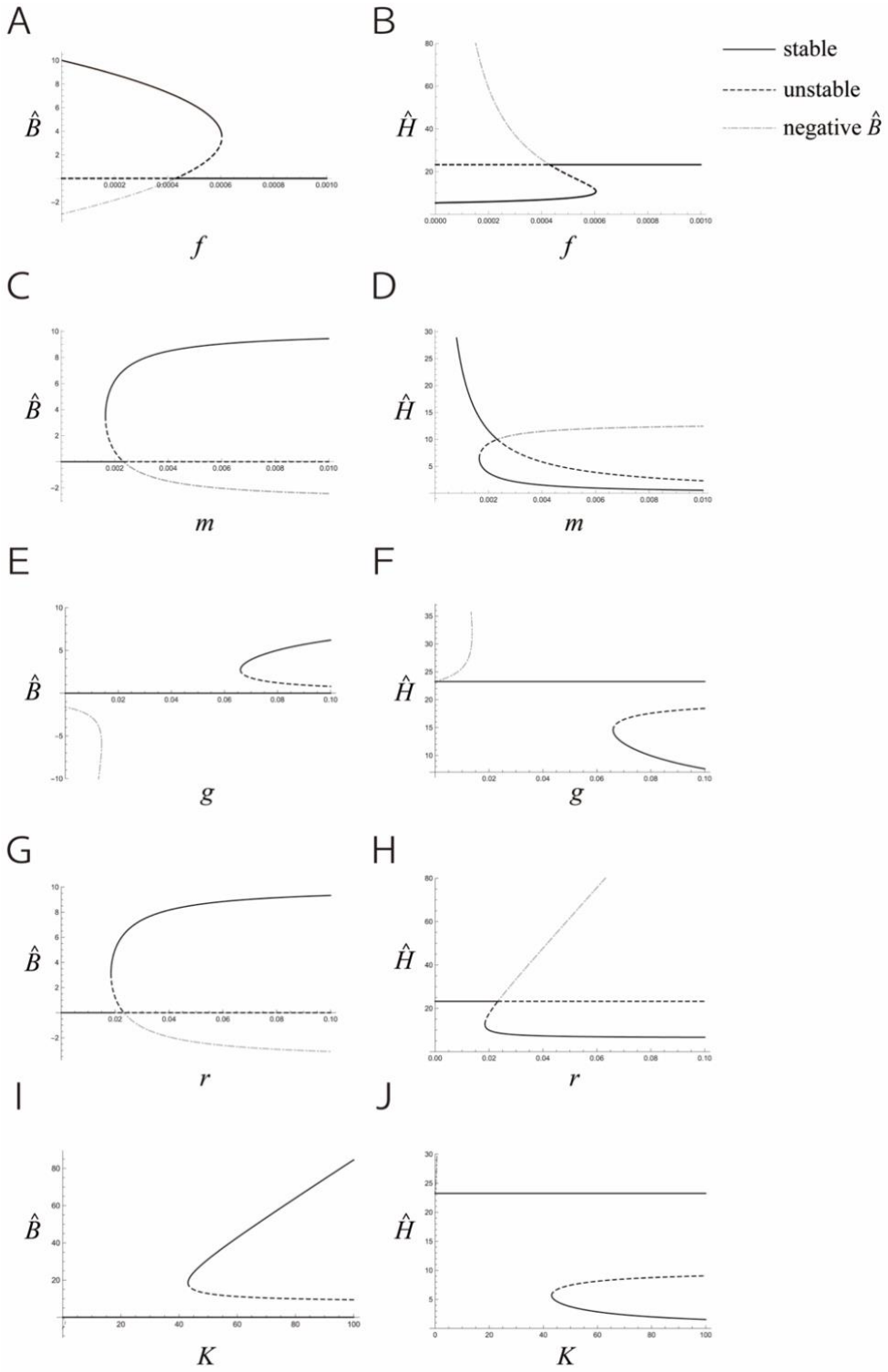

Parameter dependence of the equilibria. We varied some parameters' values and analytically calculated the intersection of Eqs. 2(a) and 2(b), which corresponds to the equilibria of $\hat{B}$ and $\hat{H}$ in this system. The black solid lines show the value of the

stable equilibria, and the black dotted lines show that of the unstable equilibria. The grey dashed line represents the equilibria of the dynamics; however, the value is accompanied by negative $\hat{B}$. Thus, we can ignore them in this context. The value of $\hat{B}$ and $\hat{H}$ are shown in the parts in the left (Figs. 3(A), 3(C), 3(E), 3(G), and 3(I)) and those in the right (Figs. 3(B), 3(D), 3(F), 3(H), and 3(J)), respectively.

Figs. 3(A) and 3(B) show the results of varying *f* (suppression effect of Th on bacteria). The parameters, except for *f*, are set at the following standard values: $A = 1, b = 1, c = 0.7, dh = 0.1, dr = 0.001, m = 0.001, g = 0.1, n = 1, K = 10, r = 0.01,$ and $f = 0.001$.

Figs. 3(C) and 3(D) show the results for different values of *m* (Treg suppression strength), which are on the horizontal axes. The other parameters are set at the standard parameter values.

Figs. 3(E) and 3(F) show the results for different values of *g* (Treg induction efficiency of the microbes), which are on the horizontal axis. The other parameters are set at the standard parameter values, except for $r = 0.02$.

Figs. 3(G) and 3(H) show the results for different values of *r* (growth rate of the microbes), which are on the horizontal axis. The other parameters are set at the standard values, except for $g = 0.08$.

Fig 3(I) and 3(J) show the results for different values of *K* (carrying capacity of the microbes), given on the horizontal axis. The other parameters are set at the standard values, except for $g = 0.05$.

Figure 4

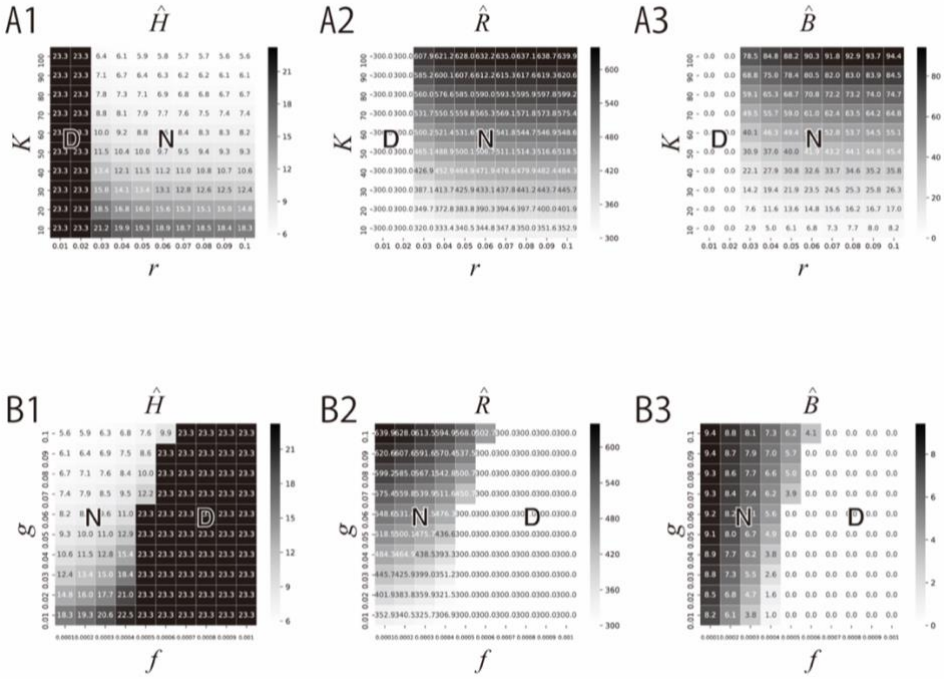

Effects of bacteria-related parameters on equilibria (r and K; f and g). We vary the bacteria-related parameters (*r*, *g*, *f*, and *K*) for ten levels and numerically calculate the abundance of Th ($\hat{H}$), Treg ($\hat{R}$), and Treg-inducing intestinal microbes ($\hat{B}$) after a sufficiently long time (t =50000) has passed. Each cell has the values of $\hat{H}$, $\hat{R}$, and $\hat{B}$ in it, and its color represents the magnitude. Each graph has a color scale presenting values beside it.

The symbols "D" and "N" indicate that the corresponding area is in dysbiosis ($\hat{B} = 0$) and non-dysbiosis state ($\hat{B} > 0$), respectively. All parameters except for *r*, *g*, *f*, and *K* are fixed as $A = 1, b = 1, c = 0.7, d_h = 0.1, d_r = 0.001, m = 0.001, g = 0.01, r = 0.01, n = 1, K = 10, and\ f = 0.001$.

Figs. 4(A1), 4(A2), and 4(A3) illustrate the results for different values of *r* (growth rate; on the horizontal axis) and *K* (carrying capacity; on the vertical axis). The "D" area with $r = 0.01, 0.02$ has a high Th level, low Treg level, and almost zero microbes; which correspond to a dysbiotic state.

Figs. 4(B1), 4(B2), and 4(B3) illustrate the result for different *f* (suppression effect on the microbes by the Th cells; on the horizontal axis) and *g* (Treg induction efficiency; on the vertical axis). "D" appears where *f* is large and *g* is small.

Figure 5

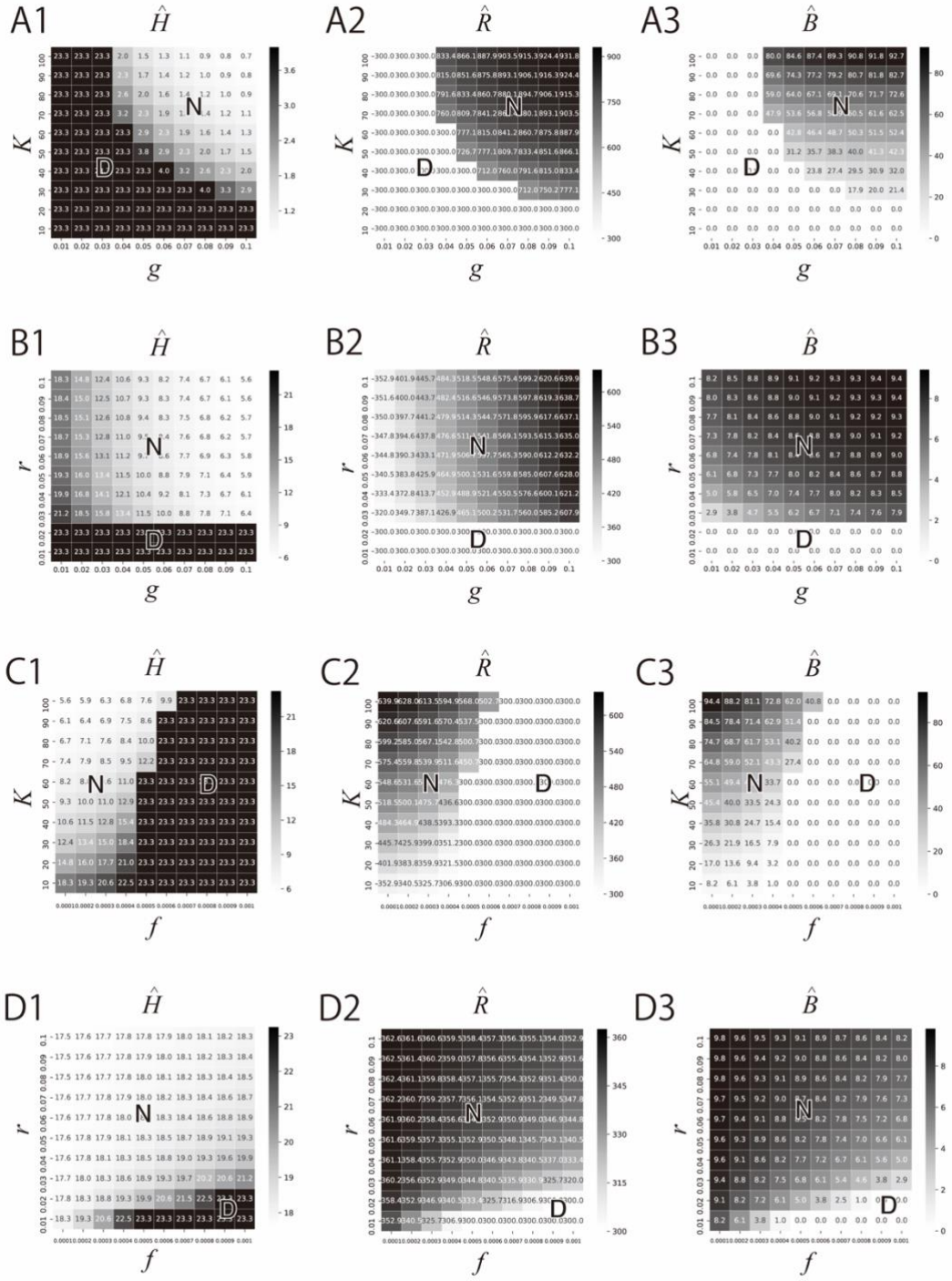

Effects of bacteria-related parameters on equilibria (combinations other than those in Figure 4). We vary the bacteria-related parameters (*r*, *g*, *f*, and *K*) for ten levels and

numerically calculate the abundance of Th ($\hat{H}$), Treg ($\hat{R}$), and Treg-inducing intestinal microbes ($\hat{B}$) after a sufficiently long time (t =50000) has passed. Each cell has the values of $\hat{H}$, $\hat{R}$, and $\hat{B}$ in it, and its color represents the magnitude. Each graph has a color scale presenting values beside it.

The symbols "D" and "N" indicate that the corresponding area are in dysbiosis ($\hat{B} = 0$) and non-dysbiosis state ($\hat{B} > 0$), respectively. All parameters except for r, g, f, and K are fixed as $A = 1, b = 1, c = 0.7, d_h = 0.1, d_r = 0.001, m = 0.001, g = 0.01, r = 0.01, n = 1, K = 10, and\ f = 0.001$.

Figs. 5(A1), 5(A2), and 5(A3) illustrate the results for different values of g (Treg induction efficiency; on the horizontal axis) and K (carrying capacity; on the vertical axis). The "N" area, where both g and K are large, represents a lower Th level and higher Treg and microbe levels; and the "D" area, where either g or K is small, represents the dysbiotic state.

Figs. 5(B1), 5(B2), and 5(B3) illustrate the results for different values of g (Treg induction efficiency; on the horizontal axis) and r (growth rate; on the vertical axis). The "D" area with $r = 0.01, 0.02$ has a high Th level, low Treg level, and almost zero microbes. The "N" area has a relatively low Th level and high Treg and microbe levels.

Figs. 5(C1), 5(C2), and 5(C3) illustrate the results for different values of f (suppression effect on the microbes by the Th cells; on the horizontal axis) and K (carrying capacity; on the vertical axis). "D" appears where f is large and K is small.

Figs. 5(D1), 5(D2), and 5(D3) illustrate the results for different values of f (suppression effect on the microbes by the Th cells; on the horizontal axis) and r (growth rate; on the vertical axis). "D" appears where f is large and r is small.

Chapter 3: Autoimmune diseases initiated by pathogen infection: Mathematical modeling

The study in this chapter, done in collaboration with Dr. Yoh Iwasa, was published in Journal of Theoretical Biology 498:110296 in 2020

Abstract

Many incurable diseases in humans are related to autoimmunity and are initially induced by a viral infection. Presumably, the virus has antigens with epitopes similar to those found in components of the host's body, thus allowing it to evade immune surveillance. Viral infection activates the immune system, which results in viral clearance. After infection, the enhanced immune system may begin to attack the host's cells, tissues, and organs. In this study, we developed a simple mathematical model in which we identify the conditions needed to trigger an autoimmune response. This model considers the dynamics of T helper (Th) cells, viruses, self-antigens, and memory T cells. Viral infection results in a temporal increase in viral abundance, which is suppressed by an increase in the number of Th cells. For the virus to be eliminated from the body, the level of Th cells must be maintained above a certain threshold to prevent viral replication, even in the absence of virus in the body. This role is realized by memory T cells produced during temporal viral infections. Thus, we investigated the conditions needed for the immune response to be enhanced after viral infection and concluded that cross-immunity must be weak for negative selection and T-cell activation but strong for antigen-suppressing reactions. We also discuss alternative models of cross-immunity and possible extensions of the model.

Key words: autoimmunity, molecular mimicry, immune memory.

1. Introduction

The immune system is designed to defend the body from pathogens, such as viruses, bacteria, and parasites. However, the immune system can sometimes attack the body, resulting in serious autoimmune disorders. In fact, many incurable diseases in humans have some elements of autoimmunity, including rheumatoid arthritis, systemic lupus erythematosus (SLE), scleroderma, multiple sclerosis, and myasthenia gravis.

To prevent autoimmunity, multiple mechanisms exist to distinguish between the body's own antigens and potentially harmful foreign antigens. Because of these mechanisms of immune tolerance that prevent the immune system from attacking self-antigens, autoimmunity is usually suppressed. Under normal conditions, when the body is infected by a virus or other pathogen, the immune system is activated in an attempt to eliminate the pathogen. However, after the pathogen is successfully cleared from the body, the immune system may start attacking the body, to which the immune system was tolerant before the infection.

The main mechanisms of autoimmunity have not yet been fully elucidated. Several studies suggest that autoimmunity is triggered by pathogen infection (Root-Bernstein & Fairweather 2014). Pender (2003) pointed out that Epstein-Barr virus (EBV) is associated with the development of various chronic autoimmune diseases and hypothesized that EBV has a unique ability to induce autoimmunity. Another possible scenario is known as "molecular mimicry," which is a mechanism whereby pathogens evade immune system surveillance by presenting antigens that are similar to the body's own antigens, leading to autoimmunity. Many models have been used to analyze the different aspects of molecular mimicry (Blyuss & Nicholson 2012, 2015; Delitala et al., 2013; Root-Bernstein & Fairweather 2014). Blyuss and Nicholson (2012, 2015) hypothesized that T cells with different activation thresholds to self-antigens exist, effectively simulating autoimmunity. Delitala et al. (2013) also modeled molecular mimicry but focused on comparing the effects between molecular mimicry and genetic alteration on the development of autoimmunity.

In the present study, we developed simple mathematical models for autoimmune disease after a viral infection event. The scenario we consider is as follows: two types of antigens, pathogenic (viral) antigens and host antigens (self-antigens), exist in large

quantities in the body. The immune system does not attack the self-antigens because of negative selection, which reduces the number of undifferentiated T cells reactive to self-antigens. At a certain timepoint, a pathogen invades the host body and quickly replicates and becomes abundant. This pathogen is subsequently suppressed by enhanced T helper cells (Th cells) that are reactive to the pathogen's antigens. Some naïve T cells become memory T cells, which persist in the host's body and continue to produce active Th cells at a threshold level, which is an amount high enough to eliminate the pathogen from the body. However, due to cross-immunity, these Th cells start to attack the self-antigens, resulting in autoimmunity. This scenario requires the following four key processes in the model:

[1] Immune tolerance: There must be mechanisms of immune tolerance. The most important among them is the negative selection of immune cells during selection in the thymus, i.e. when naïve immune cells are killed or inactivated when they encounter self-antigens present in the thymus (Takaba and Takayanagi, 2017). Additionally, naïve Th cells must be activated when they encounter a specific antigen in peripheral tissues, becoming fully effective in the presence of additional factors. In the absence of these factors, the immune response does not occur (i.e., anergy) (Appleman and Boussiotis, 2003). Finally, there are regulatory T cells that suppress T cell activation after encountering the antigen and Th cells in the peripheral tissues (Sakaguchi et al., 2008).

[2] Immune memory: After temporary abundance, the invading pathogen (virus) is eliminated from the body. This requires memory T cells or long-life immune cells (Wodarz & Nowak, 2000; Wodarz et al., 2000a, 2000b). Otherwise, the pathogen stays in the body, albeit at a low level.

[3] Cross-immunity: The immune reactions of Th cells to the self-antigen and to the virus are not perfectly independent, a process known as "cross-immunity." There are several forms of cross-immunity, each differing in outcome.

[4] Danger signal: In addition, the immune system tends to target antigens that are judged as likely to be pathogenic (Matzinger, 1994, 1998). For example, some pathogens have regions called "pathogen-associated molecular patterns (PAMPs)" and "damage-associated molecular patterns (DAMPs)," denoting proteins that immune cells are able to

recognize (Pradeu & Cooper, 2012). We referred to this as the “danger signal,” which warns the immune system of the potential pathogenicity of the focal antigen.

We considered a dynamic system of virus abundance, Th cells reactive to self-antigens, Th cells reactive to viruses (i.e. foreign antigens), and memory T cells that increase the number of Th cells reactive to the virus. Here, we investigated whether or not there exists a situation in which this scenario can be realized, and determined the parameter combinations required for this scenario to be likely to occur, investigating alternative modes of cross-immunity, parameter dependence, and extensions of the basic model. We aimed to develop a mathematical framework to understand the development of autoimmunity caused by molecular mimicry.

2. Model considering cross-immunity

We considered a scenario in which the immune response to self-antigens becomes inflated after a temporal event of viral infection. Because the virus and self-antigen are immunologically similar, the enhanced immune activity starts to attack the host self-antigen. We focused on situations in which, without viral infection, the immune system attacks the self-antigen at a very low level, that is, one that is tolerable for the host. The enhancement of the immune response of the host is caused by a temporary viral infection and results in autoimmunity.

To be specific, we considered two different antigens: viral particles and self-antigens. The former does not exist initially, but then it invades the host body in small quantities and proliferates within the host. In contrast, self-antigens exist in the body in large amounts, and this amount does not increase. We considered two different Th cells that react to the virus and to self-antigens, respectively. Let V be the abundance of the virus, H_v the number of Th cells reactive to the virus, H_s the number of Th cells reactive to the self-antigen, and M the number of memory T cells. Figure 1 illustrates the interaction between the variables considered in the model. The dynamics of these variables are given by the following equations:

2.1 Model equations

$$\begin{cases} \frac{dV(t)}{dt} = rTV(t) - kV(t)(H_v(t) + \beta_1 H_s(t)) \quad , & \text{(1a)} \\ \frac{dH_v(t)}{dt} = \alpha(V(t) + \beta_2 S) + qM(t) - d_h H_v(t) \quad , & \text{(1b)} \\ \frac{dH_s(t)}{dt} = \frac{\alpha}{1+hS_0^2}(\beta_2 V(t) + S) - d_h H_s(t) \quad , & \text{(1c)} \\ \frac{dM(t)}{dt} = \rho D_v V(t) \quad , & \text{(1d)} \end{cases}$$

$$[\text{Immune response}] = SH_s(t) + V(t)H_v(t) + \beta_3(V(t)H_s(t) + SH_v(t)) \quad . \quad \text{(1e)}$$

Equation (1a) represents viral dynamics. Virus abundance increases exponentially with the growth rate r. We assumed that the target cell abundance is a constant ($T = 0.1$). The second term on the right-hand side indicates the decay of virus due to immune reactions, with a rate proportional to the weighted sum of two types of Th cells $(H_v + \beta_1 H_s)$ with a k rate coefficient. β_1 denotes the strength of cross-immunity, indicating the degree to which Th cells specific to self-antigens (H_s) contribute to the removal of the virus from the body.

Equation (1b) represents the dynamics of Th cells reactive to virus. The first term on the right-hand side indicates the growth of H_v. α is the rate of supply of naive Th cells, which are activated in proportion to the virus abundance V. They are also activated by the self-antigen S multiplied by weight $\beta_2$because of the similarity between the two antigens. This is the second form of cross-immunity. The second term on the right-hand side represents the effect of memory T cells (discussed below). The third term denotes the decay of H_v with rate d_h.

Equation (1c) represents the dynamics of Th cells reactive to self-antigen S. Negative selection in the thymus suppresses the number of naive T cells, as indicated by $\alpha/(1 + hS_0^2)$, where S_0 is the abundance of self-antigen in the thymus during the T cell training stage. These naive T cells should be activated by contact with the self-antigen S and the virus abundance V, the latter being multiplied by weight β_2 for cross-immunity of the second type. The last term of Eq. (1c) denotes the decay of Th cells at a rate d_h.

Equation (1d) represents the dynamics of memory T cells that are specific to the virus. The number of memory T cells increases at a rate proportional to the abundance of virus within the body. Because memory T cells have a long lifetime, we assumed that their decay rate can be neglected.

The high number of memory T cells indicates the amplification of virus within the body. Once a particular viral strain becomes abundant, Th cells reactive to its antigen are produced, which are later converted into corresponding memory T cells, which remain active for the host's lifetime. These memory T cells produce Th cells reactive to the corresponding antigen, as indicated by qM, the second term on the right-hand side of Eq. (1b), and maintain helper T abundance at a positive level.

We assumed that memory T cell production depends on the danger factor D_v, a quantity suggesting that the virus is likely to be pathogenic and potentially harmful to the body (Pradeu & Cooper, 2012). D_v is inflated by signals given by natural immunity or by the body realizing the harmfulness of the antigens. Here, we consider D_v as a constant specific to each type of antigen, depending on their similarity to pathogenic proteins known to be dangerous. We did not consider memory T cells as Th cells reactive to self-antigens S, as they are non-pathogenic.

Equation (1e) represents the intensity of the total immune reaction. The total immune reaction can be obtained after calculating V, H_v, H_s and M, independent of the dynamics of these variables in Eq. (1a-1d). It includes a term corresponding to the third form of cross-immunity, in which the Th specific to self-antigen also causes harmful reactions to the host. The magnitude of this cross-immunity reaction β_3 may not be proportional to the cross-immunity reaction, indicating the effectiveness of removing the virus from the host body β_1, as shown in Eq. (1a), or the cross-immunity of activating the Th cells β_2, as included in Eqs. (1b) and (1c), respectively. In this study, the initial values were set to $\big(V(0), H_v(0), H_s(0), M(0)\big) = (0, 0, 0, 0)$. The timing of the viral infection was set at $t_I = 500$ and $V(t_I) = 0.01$.

2.2 Enhanced immune response after pathogen infection

In Appendix A, we derived the following conditions to characterize any equilibrium state for the system of Eq. (1):

$$\hat{V} = 0, \qquad \hat{H}_v = \frac{q\hat{M} + \alpha\beta_2 S}{d_h}, \text{and } \hat{H}_s = \frac{\alpha S}{d_h(1 + hS_0^2)}. \tag{2a}$$

.

Note that the dynamics in Eq. (1) have an infinite amount of equilibria, differing at the level of the memory T cells $\hat{M}$. As indicated by Eq. (1d), the memory T cells would not

decrease in abundance, and the final value of $\widehat{M}$ depends on the history of the system. According to the numerical analysis, the final value of $\widehat{M}$ increases with the speed of memory T cell formation ρ. When ρ is very small but positive, we can calculate the minimum value of $\widehat{M}$; $M^* = \frac{d_h}{q}\left[\frac{r}{k} - \alpha\beta_1\left(\frac{1}{d_h} + \frac{\beta_2}{d_s(1+hS_0^2)}\right)S\right]$ (see Appendix B for derivation). In general, the final value of M is larger than this.

In Appendix A, we derive the following formula for the magnitude of the total immune response given by Eq. (1e) at equilibrium, after the pathogen has been eliminated from the body by the immune system:

$$[\text{Immune response}] = \frac{\alpha S^2}{d_h(1+hS_0^2)} + \frac{\beta_3 S(q\widehat{M}+\alpha\beta_2 S)}{d_h}. \tag{2b}$$

Note that S denotes the abundance of self-antigens and is a constant. $\widehat{M}$ denotes the abundance of memory T cells reactive to the foreign antigen (virus). $\widehat{M}$ is zero before the infection but increases while V is growing. After V becomes zero, $\widehat{M}$ remains positive. The biological meaning is as follows: before infection, memory T cells are not produced without viruses. After the infection, memory T cells remain and constantly supply Th cells specific to the virus. Thus, the immune response to self-antigens by cross-immunity remains, and we assume that this is autoimmunity caused after infection.

3. Different modes of cross-immunity

Cross-immunity is vital to the scenario presented in this study. In Eq. (1), we consider three different ways in which cross-immunity works. First, the Th cells reactive to the self-antigen may also be partly reactive to the virus and may attack it, contributing to the removal of the virus from the body, although to a lesser extent than the Th cells intrinsically reactive to the virus, as shown in Eq. (1a). The effectiveness of cross-immunity of this type is denoted by β_1. Second, the Th cells reactive to the virus may also be activated by contact with the self-antigen in a manner less effective than by contact with the virus, as shown in Eq. (1b). Additionally, the Th cells reactive to the self-antigen may be activated by contact with the virus; this activation is less effective than

that caused by contact with self-antigen, as shown in Eq. (1c). The effectiveness of the cross-immunity of type 2 is indicated by β_2. Finally, the Th cells reactive to the virus may also be reactive to the self-antigen, resulting in an immune response. The effectiveness of this response has a weighing factor β_3, as shown in Eq. (1e).

Among the four terms of the total immune response in Eq. (1e), the first term SH_s is small because the Th cells reactive to self-antigens are suppressed to low levels by the negative reaction in the thymus. The terms VH_v and $\beta_3 VH_s$ can be neglected as the virus will eventually be cleared from the body. In contrast, the last term $\beta_3 SH_v$ is likely to be important in inducing autoimmunity, as the amount of self-antigen is abundant in the body, but also because the amount of Th cells reactive to the virus is maintained by memory T cells (i.e. immune memory).

A more quantitative argument is provided in Eq. (2b). The enhanced immune response is denoted by the second term on the right-hand side. Since this term is multiplied by β_3, the immune reaction is enhanced only when $\beta_3 > 0$. When $\beta_3 = 0$, there is no enhanced immune response. In contrast, the second term does not include β_1 explicitly, but β_1 may also have some effect on $\widehat{M}$. β_2 appears in the term explicitly and may, in addition, affect $\widehat{M}$.

3.1 Presence and absence of different modes of cross-immunity

We investigated the effect of different modes of cross-immunity by calculating the dynamics for eight different conditions, in which β_1 was either 0 or 0.3, β_2 was either 0 or 0.3, and β_3 was either 0 or 0.3 ($2^3 = 8$ cases).

Figure 2A illustrates the trajectories of the immune response level for different combinations of cross-immunity. Those with positive β_3 exhibit an immune response level after infection greater than the one before infection. In contrast, those with $\beta_3 = 0$ have a final immune response level that is exactly equal to the level before infection (labeled as V). This result is consistent with Eq. (2b), which states that enhancement of the immune response occurs only when $\beta_3 > 0$.

Among those with $\beta_3 > 0$, the case without the two other types of cross-immunity ($\beta_1 = 0,\ \beta_2 = 0,\ \beta_3 > 0.3$) developed the highest level of immune response (labeled as I), while the case with all three types of cross-immunity present ($\beta_1 = 0.3$,

$\beta_2 = 0.3,\ \beta_3 > 0.3$) achieved the lowest immune response level (labeled as IV). Two other cases are between these extremes, but the case of $\beta_1 = 0.3,\ \beta_2 = 0$, and $\beta_3 > 0.3$ (labeled as ii) had a slightly higher level of final immune reaction than the case with $\beta_1 = 0,\ \beta_2 = 0.3$, and $\beta_3 > 0.3$ (labeled as iii).

The immune response was slightly higher when $\beta_2 = 0$ (labeled as i and ii) than when $\beta_2 > 0$. The immune response directly increased with β_2 and indirectly decreased via reduction of $\widehat{M}$. These two effects canceled each other out and resulted in a small net effect of β_2 on the immune response. This result was similar to that obtained for Th cells specific to pathogens (H_v Fig. 4B in Appendix C).

Figure 2B illustrates the typical trajectories of M, the number of memory T cells reactive to viral proteins. Because β_3 has no effect on the dynamics, the trajectory of M should be independent of β_3. The final level of M decreased with β_1 and β_2. Cross-immunity including the virus and Th cells reduced the replication and spread of the virus, leading to a lower final level of memory T cells. The reductions of $\widehat{M}$ by β_1 and β_2 were very similar. The amount of induced memory T cells reflected the magnitude of the viral outbreak (V Fig. 4A in Appendix C).

We performed a similar analysis to the effect of different modes of cross-immunity on several different aspects of the dynamics (V, H_v, and H_s). Our results are explained in Appendix C.

3.2 Regression analysis

To understand the relative importance of the three modes of cross-immunity, we performed linear regression analysis using the values of the immune response and memory T cell levels in β_1, β_2, and β_3 (logarithmic scale). We generated 800 combinations of β_1, β_2, and β_3 randomly by choosing each β_i from a uniform distribution over $0 < \beta_i < 0.3$, with the other parameters fixed at the standard values ($r = 3, k = 0.1,\ D_v = 1, \alpha = 1,\ q = 1, h = 1,\ d_h = 0.1,\ S = 1,\ S_0 = 1,\ \rho = 1$). The values of the immune response and memory T cell at the steady state were calculated by multivariable regression analysis (Harrell, 2001) using the Linear Regression module of the Python package in StatsModels (Seabold and Perktold, 2010).

The estimated coefficients represent the effect of β_1, β_2, and β_3 on the immune response level after infection, as shown in Table 1A. β_3 had the largest positive coefficient (0.0741), which is consistent with the results in Fig. 2A, representing an immune response enhanced by β_3 after infection (Fig. 2A). β_1 had a negative coefficient (–0.0300), which is also consistent with the results in Fig. 2A, exhibiting an immune response suppressed by positive β_1. The effect of β_2 was smaller (–0.0460) than β_1 that of or β_3.

Next, we determined the effects on $\widehat{M}$, the levels of memory T cells after infection. The dependence of $\widehat{M}$ on β_1 and β_2 is shown in Table 1B. Since β_3 is not involved in the dynamics of memory T cells, it should not affect $\widehat{M}$. All of the coefficients had negative values, implying that the effects of cross-immunity suppress the accumulation of memory T cells. The estimated regression coefficients on β_1 (–0.2819) and on β_2 (–0.5985) were both negative.

In summary, a larger β_3 enhanced the immune response after infection (Table 1). In contrast, increased β_1 and β_2 reduced memory T cell accumulation (Table 1B), as β_1 reduces the immune response after infection (Table 1A). The immune response before infection is given by Eq. (2b) with $\widehat{M} = 0$, while the immune response after infection is given by Eq. (2b) with $\widehat{M} > 0$. Both increase with β_2. In addition, an enhanced β_2 reduces $\widehat{M}$, that is, the accumulation of memory T cells (see Table 1B).

4. Dependence of enhanced autoimmunity on other parameters

Next, we investigated the dependence of the system on parameters other than cross-immunity. We focused on cases with some cross-immunity ($\beta_1 = \beta_2 = \beta_3 = 0.3$). However, according to the numerical analyses, the qualitative nature of the parameter dependence of the model with cross-immunity was similar to that without cross-immunity.

We varied the parameters in Eq. (1a-1e) and calculated the time course of the virus abundance (V), Th cells specific to the virus (H_v), Th cells specific to self-antigen (H_s), and memory T cells (M).

We examined the parameter dependence of the dynamics, especially the magnitude of immune responses. For simplicity, we used standard parameters ($r = 3, k = 0.1,\ D_v = 1,\ \alpha = 1,\ q = 1,\ h = 1,\ d_h = 0.1,\ S = 1,\ S_0 = 1,\ \rho = 1$) and

examined the cases in which each parameter was changed to 25%, 50%, 100%, 200%, and 400% of the one in the standard parameter set, with the other standard values at fixed values.

4.1 Immune response after infection

Figure 3 illustrates the ratio of the immune response after infection if one of the parameters is modified from the standard value. The horizontal axis denotes the magnitude of change, represented as the ratio to the standard value. The immune response after infection increased with α (the rate of the supply of naive T cells) and S (the amount of self-antigen) (Fig. 3). When α (Th production rate) and S (self-antigen in peripheral organs) were higher, the production of Th cells and immune responses to the self-antigen were enhanced. D_v, ρ, and q, parameters related to memory T cell production and transition to Th cells have relatively small effects compared to other parameters, but if they were increased, the immune response was slightly enhanced. q, the

In contrast, the immune response directly decreased with d_h (decay rate of Th cells) and S_0 (self-antigens that induce negative selection in the thymus), as indicated by the negative slopes of the graph (Fig. 3). If the Th cells had a longer lifetime, more Th cells would be preserved after infection, resulting in a stronger immune response. As S_0 increased, the immune response decreased. If the negative selection of Th cells was more stringent, the less self-reactive T cells (H_s) would be released into the peripheral organs and the immune response to self-antigens would become milder.

4.2 Parameter dependence of the immune response

To elucidate the details of parameter dependence, we performed a multivariate analysis on the parameters in our model (Eq. 1). The estimated coefficients of the parameter dependence are summarized in Table 2. Here, 2,000 combinations of the parameters were randomly generated by setting each parameter as a value chosen from a uniform distribution between 0 and 10. We set β_1, β_2, and β_3 as 0.3. We calculated the immune response level using the parameter settings and estimated the coefficients of the

parameters (multivariate analysis and simultaneous linear regression of logarithmic response on a number of logarithmic values of parameters).

Table 2 shows how the immune response after infection changed with the different parameters, calculated using multivariate analysis. The immune response after infection dramatically increased with S and α (regression coefficients were 1.5321 for S; and 0.5382 for α); it also increased with r, q, D_v, and ρ (coefficient for r was 0.0365; for q was 0.0675; for D_v was 0.0506; for ρ was 0.0597). In contrast, increases in d_h, k, S_0, and h had a negative effect on the immune response (coefficients for d_h was –0.9105; for k was –0.3328; for S_0 was –0.4561; for h was –0.1902). The magnitude of each calculated coefficient corresponds to the effect of each parameter, as shown in section 4.1. These results could be interpreted as follows: As represented in Eq. (2b), the immune response was increased by increasing S, α, and q, and by decreasing d_h, h, and S_0, which is consistent with the results presented in sections 4.1 and 4.2. In addition, the other parameters, which are not included in Eq (2b), such as k, r, D_v, and ρ, had an effect on the immune response through $\widehat{M}$, that is, the amount of memory T cells. If r (viral growth rate) was higher or k (viral clearance rate) was lower, the virus could reproduce more successfully, resulting in the production of memory T cells until the virus was eliminated. If D_v (danger factor) and ρ (production rate of memory T cells) were higher, memory T cells would be more likely to be produced in response to the viral infection.

5. Discussion

Some autoimmune diseases are known to start after a viral infection is cleared, including systemic lupus erythematosus, multiple sclerosis, Sjogren's syndrome, rheumatoid arthritis, autoimmune thyroiditis, autoimmune hepatitis, cryptogenic fibrosing alveolitis, and pure red cell aplasia (Pender 2003). Viruses with antigen epitopes similar to those of the host's self-antigens are likely to escape immune surveillance, a phenomenon known as molecular mimicry (Albert and Inman 1999). However, once the virus begins to proliferate in the host, the immune system is activated and eventually kills off the virus. Once the infection is over, though, the activated immune system may begin

to attack the host because of the similarity of self-antigens and viral antigens, resulting in autoimmunity.

Here, we examined a simple dynamic model of Th cells, virus abundance, self-antigen, and memory T cells. We examined the conditions under which the total immune response was enhanced after viral infection. In this study, we determined the conditions under which cross-immunity has a large effect. To this end, we examined the role of memory T cells as well as other parameters, on the development of autoimmunity.

We found that cross-immunity takes several different forms. We focused on three different types: (1) Th cells are reactive to the self-antigen, which also suppresses viral growth, although less effectively than; (2) virus activates Th cells specific to self-antigen, where the presence of self-antigen may also activate the Th cells specific to the virus; (3) Th cells specific to viruses cause immune reaction symptoms in the host by cross-reacting with self-antigen. This cross reaction is very serious because of the persistence of Th cells specific to the virus due to the presence of memory T cells, formed during temporary viral infection, and the presence of abundant self-antigens in the host body. In contrast, the cross reaction of the opposite form, i.e. the immune reaction to virus by Th cells specific to self-antigen, is less problematic because it results in clearing the virus from the body.

We may then consider another form of cross-immunity. For example, the negative selection step may have cross-immunity. However, if the negative selection of Th cells includes cross-immunity, the abundant self-antigen would suppress the production of H_v, and hence the virus abundance V cannot be suppressed after infection. Hence, this does not realize the scenario studied in this work. Although we focused on the effect of cross-immunity on different stages of immune responses, we can also consider another model that captures cross-immunity more mechanistically. The strength of cross-immunity may depend on the binding affinity of T cells and antigens. Thus, different parameters of strength of cross-immunity can be considered for the interactions [1] between Th specific to virus and self-antigen, and [2] between Th specific to self-antigen and virus. Therefore, the parameter β_2 in Eq. (1b) and (1c) of the current model can be changed considering different degrees of binding affinity of Th and antigens.

We compared different combinations of the three types of cross-immunity and examined the conditions under which immune activity after temporal viral infection is likely to be enhanced. We found that cross-immunity on the inflated symptoms of the immune response is the key to enhanced immune activity (a large β_3 in Fig. 2A and Table 1A), which leads to autoimmunity. In contrast, cross-immunity of the other types (i.e., Th cells on removing viruses (β_1) and Th production (β_2)) had a tendency to suppress viral infection or the accumulation of memory T cells (Fig. 2A and Table 1B). From these results, we conclude that for this scenario to work, cross-immunity must be weak for negative selection and T-cell activation, but strong for antigen-suppressing reactions.

The conditions under which autoimmunity occurs after temporal viral infection most likely involve a high β_3 and a low β_1 and β_2. This suggests that autoimmunity is most likely caused by processes that do not suppress viral growth or activate Th cells but do induce exaggerated immune responses.

Memory T cells play an important role in the elimination of viruses from the body. Wodarz and Nowak (2000) found that immune cells need a very slow turnover in order to eliminate the pathogen. In the present study, we assumed that there is no turnover of memory T cells that are able to eliminate the virus from the body after temporal infection. However, after temporal infection, the host must form immunity to fight against the antigen immediately should re-infection occur. On the other hand, the formation of memory T cells for self-antigens must be suppressed; otherwise, the immune response would be activated even without viral infection, resulting in autoimmunity.

In the current model, parameter q represents the inflow rate from memory T cell to Th cell population (Eq. (1b)), which may result in the relatively small effect of q on immune responses (Fig. 3 and Table 2). A model including a migration term from memory T cells to Th cells (i.e. adding $-qM$ to Eq. (1d)) may exhibit a stronger effect of q on immune responses than the current model, assuming that the cell number of memory T cells decreases as they turn into Th cells. It will be an important future work to examine this alternative model.

Blyuss and Nicholson (2012) also discussed the development of autoimmunity using their mathematical model, considering T cell populations with different activation

levels to self-antigens, which roughly correspond to H_v and H_s in our model. However, there are several different assumptions between these two theories. First, Blyuss and Nicholson described the clearance of infection, chronic infection, and recurrent infections as different steady states. In our model, we do not consider chronic infection (equilibrium $V > 0$), and we assume that the virus will be cleared after infection. Second, Blyuss and Nicholson considered that T cells with a lower threshold to self-antigens (i.e., autoreactive T cells) were produced from the population of activated T cells. In our model, a change in the specificity of T cells did not occur.

Delitala et al. (2013) compared the effect of molecular mimicry using a mathematical model and that of genetic alteration on autoimmunity development. They demonstrated that molecular mimicry caused the over-proliferation of T cells and increased reactivity to host cells. However, this is in contrast to our conclusions. In our model, more T cells specific to pathogens (H_v) were produced in the absence of the cross-immunity of some modes ($\beta_1 = \beta_2 = 0$; Fig. 4B), leading to a large-scale viral outbreak ($\beta_1 = \beta_2 = 0$; Fig. 4A). The difference between the two models is a result of the dynamics of pathogen and memory T cells being considered in this work, unlike in Delitala et al. (2013) .

In contrast to these theories, which focus on cross-immunity, Pender (2003) noted that many autoimmune diseases are caused by the Epstein-Barr virus (EBV). Pender (2003) hypothesized that this is due to the unique abilities of EBV, which has been supported by subsequent studies (Harley et al., 2018). EBV infects B cells, including self-reactive B cells. Some of the infected B cells then help self-reactive T cells live longer and avoid being killed by apoptosis. The relationship between this hypothesis and the mechanism and theory discussed in our work needs to be examined carefully.

In our model, the Th cells specific to viruses are produced from memory T cells at all times (Eq. (1b) and (1c)). Therefore, the number of Th cells is maintained after viral infection, as seen in Fig. 4B, which causes stronger immune responses after the infection (Fig. 2A). However, 90-95% of effector T cells usually disappear after pathogenic infection (Mueller et al., 2013). It is most likely that differentiation into effector T cells from memory T cells occurs only when the viruses are in the body. If so, the Th cell level is maintained low in the absence of the virus and rises quickly after reinfection by the

same virus. In our current model, the immune responses after the infection are enhanced by Th cells produced from the memory T cell population, which does not reflect realistic Th dynamics. In the future, we need to formulate the degree of immune responses that can be enhanced after the infection, even if Th cells disappear.

The origin of memory T cells is now under discussion. In our study, we assumed that the number of memory T cells is independent of the Th population, increasing in response to the amount of virus. This is consistent with the hypothesis that memory T cells are derived from naïve T cells (Restifo and Gattinoni, 2013). However, an alternative hypothesis claims that memory T cells are produced by effector T cells (Akondy et al., 2017; Youngblood et al., 2017). The mathematical modeling of this second hypothesis and the differences between the two hypotheses should also be investigated in future works.

Since the model developed in the current study is very simplified, we may extend it by incorporating a number of aspects to obtain a more realistic model. For example, the number of antigen types can be greater than two, and can even be a continuous amount of antigen types, where the "distance" controls cross-immunity. However, a more important aspect is the incorporation of regulatory T cells, which are responsible for suppressing immune activity in peripheral tissues (Sakaguchi et al., 2008). Models for regulatory T cells in the context of autoimmunity require another set of analyses, which we will discuss in a separate paper. In this study, we focused on the case where the danger factor is constant D_v in Eq. (1d). Alternatively, information on the potential risk of a particular foreign antigen could be obtained from past abundance within the host, such as $D_v = \int_0^t V(t')dt'$. If the levels of an antigen increase in the host, this would be indicative of a potential risk, since this may represent behavior that is typical of a pathogenic agent, rather than a harmless agent.

Here, we provide a mathematical formalism to phenomenologically understand the autoimmunity development caused by molecular mimicry of pathogens. In the future, we will be able to provide quantitatively accurate predictions for autoimmunity development using variables measured by experimental researchers. This study is the first step to suggest which element should be focused on to test the theory of molecular mimicry, and the model needs to be tested using experimental data in the future.

Acknowledgments

This work was supported by the JSPS Research Fellowship (DC1) and Grant-in-Aid for JSPS Fellows to A.H (No. 18J20316). We would like to thank the members of the Mathematical Biology Laboratory at Kyushu University for their useful advice.

Appendix A

Equilibrium of Eq. 1

By allowing the right-hand side of Eq. (1d), we obtain $\hat{V} = 0$. Then, by allowing the right-hand side of Eq. (1c) combined with $\hat{V} = 0$, we obtained $\hat{H}_s = \alpha S/[d_h(1 + hS_0^2)]$. Combining the right-hand side of Eq. (1b), combined with $\hat{V} = 0$, we obtained $q\hat{M} = d_h\hat{H}_v - \alpha\beta_2 S$, which leads to $\hat{H}_v = \left(q\hat{M} + \alpha\beta_2 S\right)/d_h$. Thus, Eqs. (2a) in the text. Using these results, Eq. (1e) leads to Eq. (2b).

Appendix B

Fast-slow splitting of dynamics when the growth of memory T cells ρ is very small

Dynamics (Eq. (1)) have an infinite amount of different equilibria in memory cell abundance M. This is because the memory cell abundance does not change if the virus is cleared ($V = 0$). For any given value of M, Eq. (1) has a single equilibrium. Suppose that the initial population does not contain any virus or memory T cells ($V = M = 0$). At some point, a small amount of virus invades the host, temporarily increasing the level of pathogen, which is subsequently suppressed by the enhanced immune response. The final population contains some memory T cells $M > 0$, enough to prevent future invasion by the same virus. However, the level of memory T cells M can be calculated only by numerical analysis, using Eq. (1). We can, however, calculate the value in the limit when the speed of memory T cell production is very small (ρ is very small). The argument is as follows:

When ρ is positive but much smaller than all the other parameters, the dynamics can be analyzed by splitting fast and slow dynamics. We define fast dynamics as the dynamics where $\rho = 0$. Three other differential equations are given by Eq. (1a), (1b), and (1c). Then, from Eq. (1d), $M = \text{constant}$ holds. With M given as a positive value, Eqs. (1a, b, c) converges to a single equilibrium that is locally stable. For simplicity, we consider the case in which cross-immunity is not very strong.

For $M \leq \frac{d_h}{q}\left[\frac{r}{k} - \alpha\beta_1\left(\frac{1}{d_h} + \frac{\beta_2}{d_s(1+hS_0^2)}\right)S\right]$, the globally stable steady state is

$$\hat{V} = \frac{1}{\frac{\alpha}{d_h} + \frac{\alpha\beta_1\beta_2}{d_s(1+hS_0^2)}}\left[\frac{r}{k} - \frac{q}{d_h}M - \alpha\beta_1\left(\frac{1}{d_h} + \frac{\beta_2}{d_s(1+hS_0^2)}\right)S\right],$$

$$\hat{H}_s = \frac{\alpha}{d_h(1+hS_0^2)}\left(\beta_2\hat{V} + S\right), \text{and } \hat{H}_v = \frac{1}{d_h}\left(qM + \alpha\left(\hat{V} + \beta_1 S\right)\right). \qquad \text{(B. 1a)}$$

There is another equilibrium with $\hat{V} = 0$, which is unstable.

For $M > \frac{d_h}{q}\left[\frac{r}{k} - \alpha\beta_1\left(\frac{1}{d_h} + \frac{\beta_2}{d_s(1+hS_0^2)}\right)S\right]$, the globally stable equilibrium is:

$$\hat{V} = 0, \hat{H}_s = \frac{1}{d_h(1+hS_0^2)}\alpha S, \text{and } \hat{H}_v = \frac{1}{d_h}[qM + \alpha\beta_2 S]. \qquad \text{(B. 1b)}$$

Note that for a given M there is a single equilibrium of fast dynamics. We may consider a curve that constitutes Eq. (B.1a) and (B.1b) $M > 0$ in a four-dimensional space.

Slow dynamics describe a slow movement caused by $\rho > 0$. Then, the value M increases according to Eq. (1d): $dM/dt = \rho D_v V$. This does not stop while $V > 0$, but ceases when $V = 0$. With slow dynamics, three variables are given by Eq. (B.1a) and (B.1b) as functions of M. Hence, the time change of M is given by

$$dM/dt = \rho D_v \frac{1}{\frac{\alpha}{d_h} + \frac{\alpha\beta_1\beta_2}{d_s(1+hS_0^2)}}\left[\frac{r}{k} - \frac{q}{d_h}M - \alpha\beta_1\left(\frac{1}{d_h} + \frac{\beta_2}{d_s(1+hS_0^2)}\right)S\right]. \qquad \text{(B. 2)}$$

This provides the differential equation for the slow dynamics. Starting from $M(0) = 0$, $M(t)$ slowly increases following (B.2) and converges to the following value:

$$M^* = \frac{d_h}{q}\left[\frac{r}{k} - \alpha\beta_1\left(\frac{1}{d_h} + \frac{\beta_2}{d_s(1+hS_0^2)}\right)S\right]. \qquad \text{(B. 3a)}$$

Using this expression, Eq. (B.2) becomes

$dM/dt = \rho D_v \frac{q/\alpha}{1+\frac{\alpha d_h\beta_1\beta_2}{d_s(1+hS_0^2)}}[M^* - M]$, resulting in

$$M(t) = M^*\left(1 - \exp\left[-\rho D_v \frac{q/\alpha}{1 + \frac{\alpha d_h\beta_1\beta_2}{d_s(1+hS_0^2)}}t\right]\right) \qquad \text{(B. 3b)}$$

The other variables are given by

$$V^* = 0, H_s^* = \frac{1}{d_h(1 + hS_0^2)}, \text{and } \alpha S H_v^* = \frac{r}{k} + \left(\beta_2 - \frac{\beta_1}{d_h} - \frac{\beta_1\beta_2}{d_s(1 + hS_0^2)}\right)\alpha S. \quad \text{(B. 3c)}$$

When ρ is not very small, the level of memory T cells at the final equilibrium is larger than (B.2a), according to the numerical analysis. We may conclude that (B.2a) is the minimum possible amount of memory T cells that are produced by a very small but positive ρ.

Appendix C

Trajectories of the dynamics with different combinations of cross-immunity modes

We explained the results for the level of immune reaction and the level of memory T cells in the text (Fig. 2A and 2B). Here, we show other aspects of the dynamics.

C.1. Viral abundance

In Fig. 4A, the viral abundance is shown. The horizontal axis denotes time t. The virus peak abundance was the highest for $\beta_1 = \beta_2 = 0$ (labeled as I), intermediate for $\beta_1 = 0.3, \beta_2 = 0$ or $\beta_1 = 0, \beta_2 = 0.3$ (labeled as II and III, respectively), and the lowest for $\beta_1 = \beta_2 = 0.3$ (labeled as IV). Cross-immunity of type 1 and type 2 suppressed the peak virus abundance to a similar magnitude.

C.2. Th cells specific to the virus.

In Fig. 4B, Th cells specific to the virus are shown. The horizontal axis denotes time t. The lowest level of Th cells specific to the virus was achieved when $\beta_1 = \beta_2 = 0.3$ (labeled as IV) and the highest level was achieved when $\beta_1 = \beta_2 = 0$ (labeled as I). Another two cases resulted in intermediate levels of Th cells specific to the virus, in which either β_1 or β_2 was 0.3 and the other was 0. If we compare the two cases, the case with cross-reactivity on Th cell activation ($\beta_2 = 0.3$) (i.e., self-antigen can stimulate Th cells specific to virus) resulted in a lower number of Th cells specific to the virus remaining after infection (labeled as III) compared to the case with cross-reactivity on attacking self-antigen by Th cells specific to the virus ($\beta_1 = 0.3$) (labeled as II). Eq. (2a) indicates that $\widehat{H}_v$ was affected β_1 indirectly through $\widehat{M}$ and β_2 both directly and indirectly through $\widehat{M}$, which is similar to the result of the immune response (see section 3.1 and Fig 2A).

C.3. Th cells specific to self-antigens

In Fig. 4C, we show the trajectory of Th cells specific to self-antigens. If $\beta_2 = 0$, the dynamics of the Th cells specific to self-antigens were independent of viral infection (labeled as V). The peaks observed in the dynamics correspond to the Th cells specific to self-antigens, which are the cases considering the cross-reactivity of the different types

of Th activation ($\beta_2 = 0.3$). The peak was lower with $\beta_1 = 0.3$ (labeled as IV) than $\beta_1 = 0$ (labeled as III). This is because when $\beta_1 = 0.3$, the peak of the virus load is more effectively suppressed, as shown in Fig. 4A. Fewer Th cells specific to self-antigens were produced due to cross-reactivity.

References

Akondy, R. S., Fitch, M., Edupuganti, S., Yang, S., Kissick, H. T., Li, K. W., Youngblood, B. A., Abdelsamed, H. A., McGuire, D. J., Cohen, K. W., Alexe, G., Nagar, S., McCausland, M. M., Gupta, S., Tata, P., Haining, W. N., McElrath, M. J., Zhang, D., Hu, B., Greenleaf, W. J., Goronzy, J. J., Mulligan, M. J., Hellerstein, M., Ahmed, R., 2017. Origin and differentiation of human memory CD8 T cells after vaccination. Nature 552, 362-367, doi:10.1038/nature24633.

Albert, L. J., Inman, R. D., 1999. Molecular Mimicry and Autoimmunity. New England Journal of Medicine 341, 2068-2074, doi:10.1056/nejm199912303412707.

Appleman, L. J., Boussiotis, V. A., 2003. T cell anergy and costimulation. Immunological Reviews 192, 161-180, doi:10.1034/j.1600-065X.2003.00009.x.

Blyuss, K. B., Nicholson, L. B., 2012. The role of tunable activation thresholds in the dynamics of autoimmunity. Journal of Theoretical Biology 308, 45-55, doi:https://doi.org/10.1016/j.jtbi.2012.05.019.

Blyuss, K. B., Nicholson, L. B., 2015. Understanding the roles of activation threshold and infections in the dynamics of autoimmune disease. Journal of Theoretical Biology 375, 13-20, doi: 10.1016/j.jtbi.2014.08.019.

Delitala, M., Dianzani, U., Lorenzi, T., Melensi, M., 2013. A mathematical model for immune and autoimmune response mediated by T-cells. Computers & Mathematics With Applications 66, 1010-1023, doi:10.1016/j.camwa.2013.06.026.

Harley, J. B., Chen, X., Pujato, M., Miller, D., Maddox, A., Forney, C., Magnusen, A. F., Lynch, A., Chetal, K., Yukawa, M., Barski, A., Salomonis, N., Kaufman, K. M., Kottyan, L. C., Weirauch, M. T., 2018. Transcription factors operate across disease loci, with EBNA2 implicated in autoimmunity. Nature Genetics 50, 699-707, doi:10.1038/s41588-018-0102-3.

Harrell F. E. Jr. 2001. Regression modeling strategies – With Applications to Linear Models, Logistic Regression, and Survival Analysis. Springer, New York, NY. 572 pp. doi: 10.1007/978-1-4757-3462-1

Matzinger, P., 1994. Tolerance, Danger, and the Extended Family. Annual Review of Immunology 12, 991-1045, doi:10.1146/annurev.iy.12.040194.005015.

Matzinger, P., 1998. An innate sense of danger. Seminars in Immunology 10, 399-415, doi:

10.1006/smim.1998.0143.

Mueller, S. N., Gebhardt, T., Carbone, F. R., Heath, W. R., 2013. Memory T Cell Subsets, Migration Patterns, and Tissue Residence. Annual Review of Immunology 31, 137-161, doi:10.1146/annurev-immunol-032712-095954.

Pender, M. P., 2003. Infection of autoreactive B lymphocytes with EBV, causing chronic autoimmune diseases. Trends in Immunology 24, 584-588, doi:10.1016/j.it.2003.09.005.

Pradeu, T., Cooper, E. L., 2012. The danger theory: 20 years later. Frontiers in Immunology 3, doi:10.3389/fimmu.2012.00287.

Restifo, N. P., Gattinoni, L., 2013. Lineage relationship of effector and memory T cells. Current Opinion in Immunology 25, 556-563, doi:10.1016/j.coi.2013.09.003.

Root-Bernstein, R., Fairweather, D., 2014. Complexities in the relationship between infection and autoimmunity. Current Allergy and Asthma Reports 14, 407-407, doi:10.1007/s11882-013-0407-3.

Sakaguchi, S., Yamaguchi, T., Nomura, T., Ono, M., 2008. Regulatory T cells and immune tolerance. Cell 133, 775-787, doi:10.1016/j.cell.2008.05.009.

Seabold, S., Perktold, J., 2010. Statsmodels: Econometric and Statistical Modeling with Python. Proceedings of the 9th Python in Science Conference 2010.

Takaba, H., Takayanagi, H., 2017. The Mechanisms of T Cell Selection in the Thymus. Trends in Immunology 38, 805-816, doi:10.1016/j.it.2017.07.010.

Wodarz, D., Nowak, M. A., 2000. CD8 memory, immunodominance, and antigenic escape. European Journal of Immunology 30, 2704-2712, doi:10.1002/1521-4141(200009)30:9<2704::AID-IMMU2704>3.0.CO;2-0.

Wodarz, D., May, R. M., Nowak, M. A., 2000a. The role of antigen-independent persistence of memory cytotoxic T lymphocytes. International Immunology 12, 467-477, doi:10.1093/intimm/12.4.467.

Wodarz, D., Page, K. M., Arnaout, R. A., Thomsen, A. R., Lifson, J. D., Nowak, M. A., 2000b. A new theory of cytotoxic T-lymphocyte memory: implications for HIV treatment. Philosophical Transactions of the Royal Society of London. Series B, Biological Sciences 355, 329-343, doi:10.1098/rstb.2000.0570.

Youngblood, B., Hale, J. S., Kissick, H. T., Ahn, E., Xu, X., Wieland, A., Araki, K., West, E. E., Ghoneim, H. E., Fan, Y., Dogra, P., Davis, C. W., Konieczny, B. T., Antia, R., Cheng,

X., Ahmed, R., 2017. Effector CD8 T cells dedifferentiate into long-lived memory cells. Nature 552, 404-409, doi:10.1038/nature25144.

Tables

Table 1 Dependence on the modes of cross-immunity: β_1, β_2 and β_3.

Dependence on the modes of cross-immunity: β_1, β_2 and β_3. Quantities to explain were the immune response after the infection in column A and the memory T cell level in column B. Quantities and variables were all converted to logarithmic scale (natural logarithm), and then multi-variate analysis was performed. These numbers indicate how each mode of cross-immunity contributes in predicting the respective quantity (Seabold and Perktold, 2010). All coefficients were significantly away from zero (i.e. P-values were all smaller than 0.001).

	Quantities to predict	
	(A) Immune response	(B) Memory T cells
	Coefficient	Coefficient
β_1	–0.0300	–0.2819
β_2	–0.0460	–0.5985
β_3	0.0741	---
Intercept	1.7693	–3.0067
R^2 score	0.730	0.724

Table 2 Parameter dependence of immune response after infection.

Parameter dependence of immune response after infection. The numbers represent regression coefficients for multivariate analysis. Quantity to predict represents the immune response after infection, where the predictor variables are parameters in the model. Quantities and variables were all converted into the logarithmic scale (natural logarithm), followed by multivariate analysis. The coefficients indicate how each parameter contributes to the quantity predicted (Seabold and Perktold, 2010). All coefficients were significantly away from zero ($P<0.001$ except for r, for which $P = 0.004$)

Quantities to predict	Coefficient
d_h	–0.9105
S_0	–0.4561
k	–0.3328
h	–0.1902
r	0.0365
D_v	0.0506
ρ	0.0597
q	0.0675
α	0.5382
S	1.5321
Intercept	0.4732
R^2 score	0.927

Figures

Figure 1

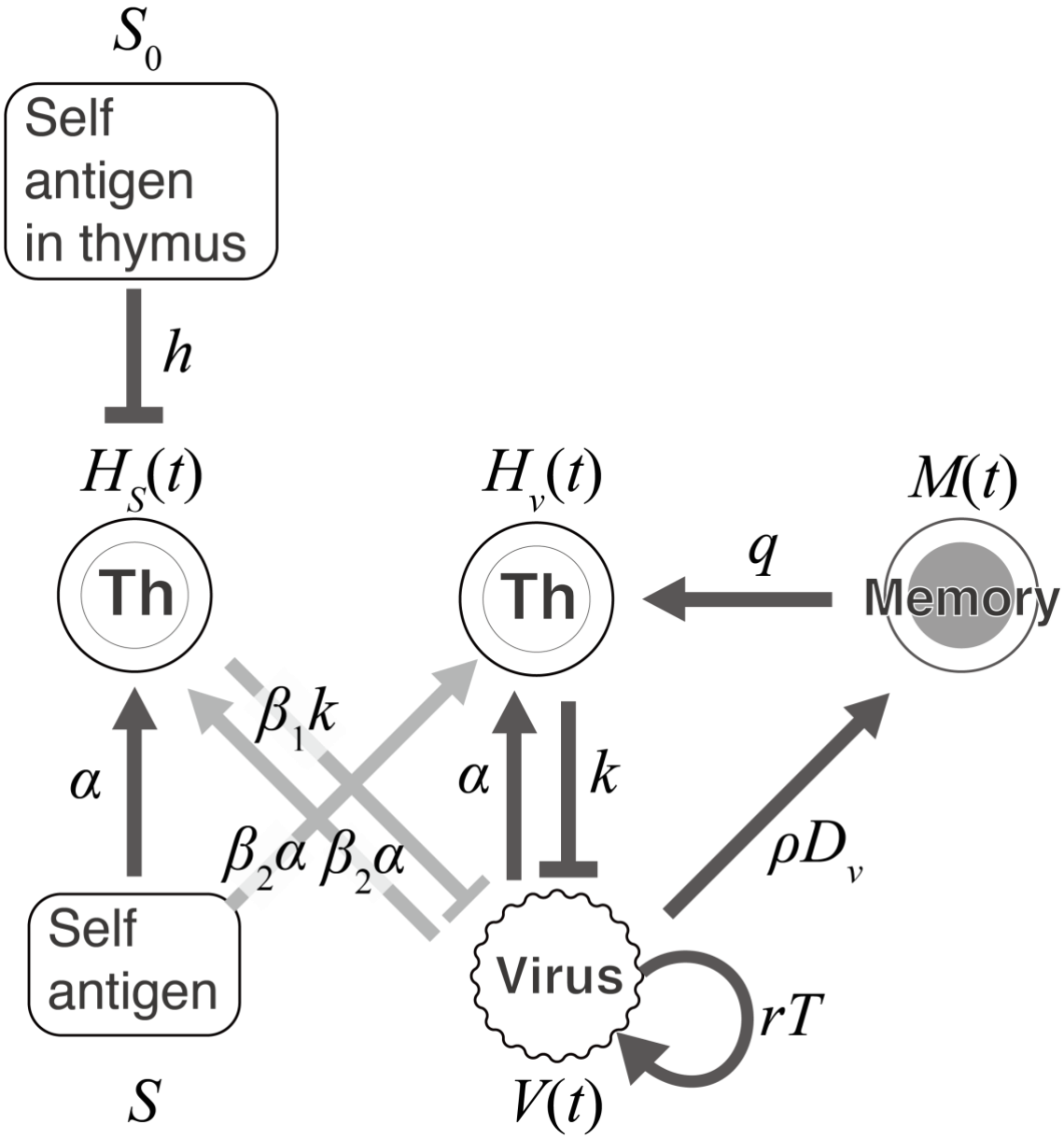

Schematic representation of the model, representing how the variables affect each other.

Figure 2

A. Immune response $\left(\boldsymbol{SH_s + VH_v + \beta_3(VH_s + SH_v)}\right)$

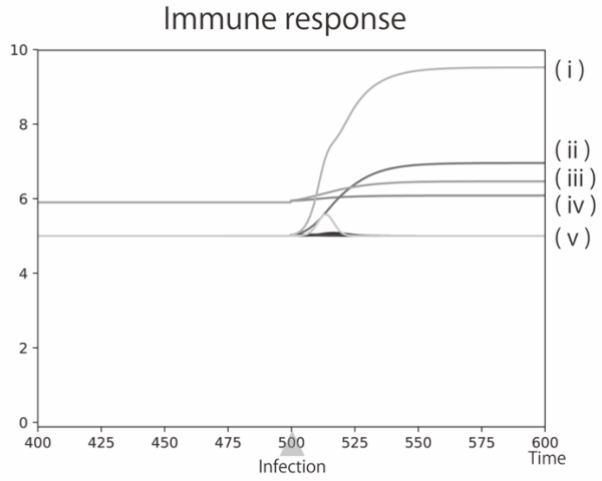

B. Memory T cell ($\boldsymbol{M(t)}$)

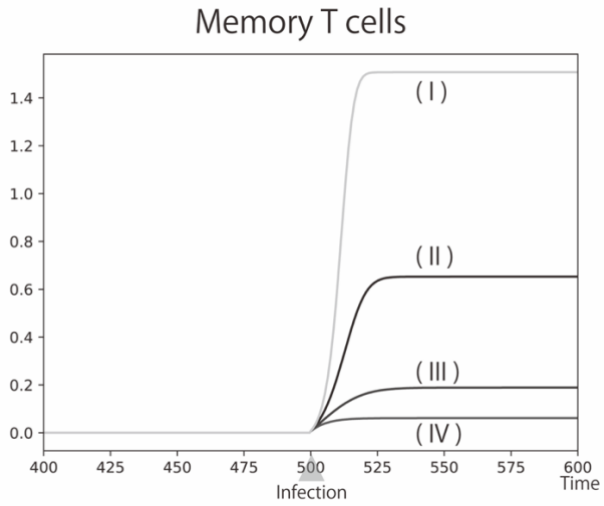

Trajectories of the model with different combinations of β_1, β_2, and β_3. The horizontal axis represents time t. (A) Immune response. The different curves are: (i),$\beta_1 = \beta_2 = 0, \beta_3 = 0.3$ (ii), $\beta_1 = 0.3, \beta_2 = 0, \beta_3 = 0.3$ (iii), $\beta_1 = 0, \beta_2 = 0.3, \beta_3 = 0.3$ (iv), $\beta_1 = \beta_2 = 0.3, \beta_3 = 0.3$ and (v) $\beta_3 = 0$. (B) Number of memory T cells. In (B), β_3 has no effect on the results. (I), $\beta_1 = \beta_2 = 0$ (II),$\beta_1 = 0.3, \beta_2 = 0$ (III),$\beta_1 = 0, \beta_2 = 0.3$ and (IV) $\beta_1 = \beta_2 = 0$.. Other parameters are: $r = 3, k = 0.1, D_v = 1, \alpha = 1,\ q = 1, h = 1, d_h = 0.1, S = 1, S_0 = 1, \rho = 1$.

Figure 3

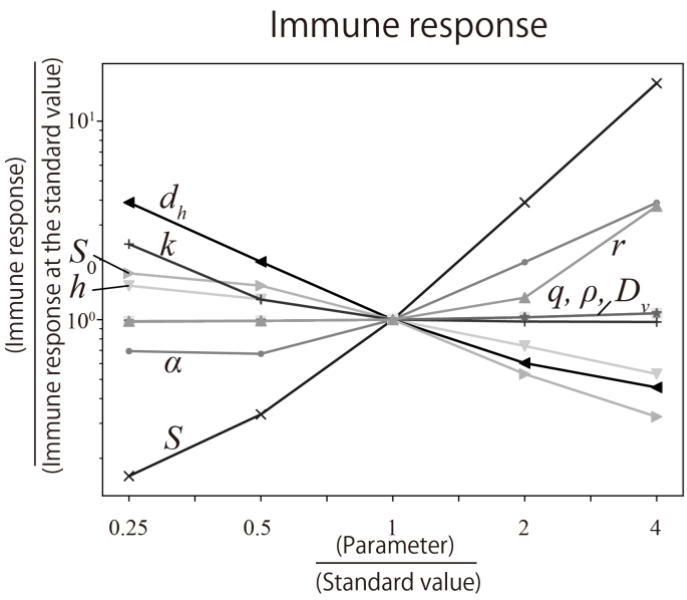

Parameter dependence of immune response after infection. One parameter is shifted by multiplying the factor indicated in the horizontal axis. Other parameters are: $r = 3, k = 0.1, D_v = 1, \alpha = 1,\ q = 1, h = 1, d_h = 0.1, S = 1, S_0 = 1, \rho = 1.$

Figure 4

A. Virus ($V(t)$)

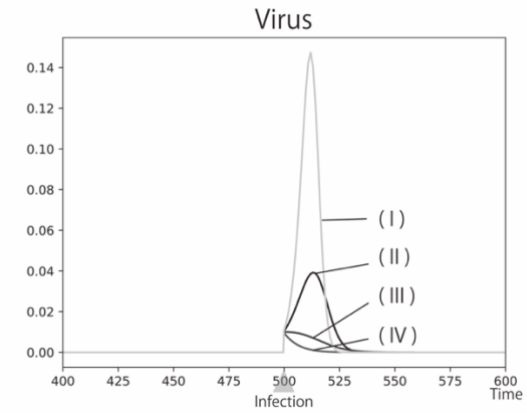

B. Th cells specific to the virus ($H_v(t)$)

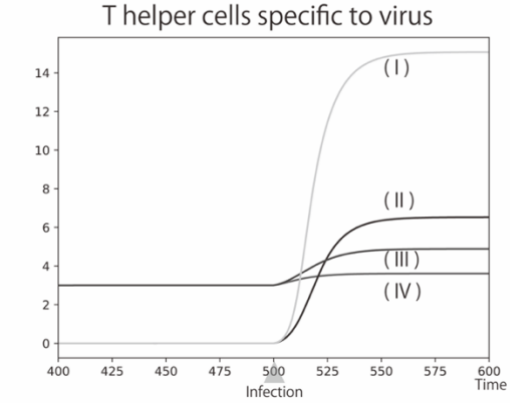

C. Th cells specific to the self-antigen ($H_s(t)$)

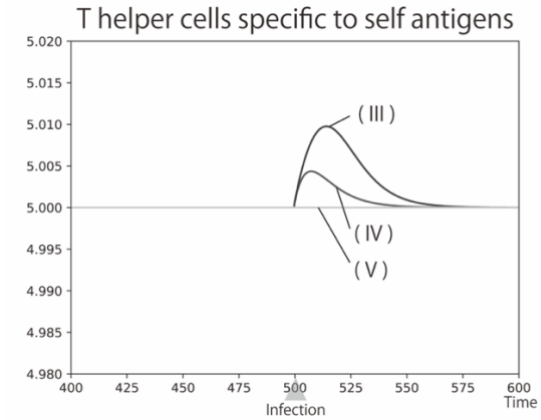

Trajectories of the model with different combinations of β_1 and β_2The horizontal axis represents time t. Different curves were calculated under the following conditions: (I) $\beta_1 = \beta_2 = 0$, (II) $\beta_1 = 0.3, \beta_2 = 0$, (III) $\beta_1 = 0, \beta_2 = 0.3$, (IV) $\beta_1 = \beta_2 = 0.3$, and (V) $\beta_2 = 0$. (A) Virus abundance (V). (B) Th cells specific to the virus (H_v). (C) Th cells specific to the self-antigen (H_s). Other parameters are: $r = 3, k = 0.1, D_v = 1, \alpha = 1, q = 1, h = 1, d_h = 0.1, S = 1, S_0 = 1, \rho = 1$.

Chapter 4 Why meals during resting time cause fat accumulation in mammals: Mathematical modeling of circadian regulation on glucose metabolism

The study in this chapter, done in collaboration with Dr. Akiko Satake,
in preparation for submission in 2021

Abstract

Meal timing and the dysregulation of metabolic systems are closely associated, which relationship has been observed as metabolic syndromes such as obesity caused by irregular meal timings among shift workers. To reveal how meal timings affect the metabolic system, the circadian regulation of nutrient metabolic systems in animals needs to be taken into account. As revealed by previous experimental studies, several pathways in glucose metabolism have been suggested to be regulated by circadian clocks. It has also been observed that food intake during the resting period compared to during the active period causes excess fat accumulation phase in rodent models. To understand the diurnal pattern of glucose metabolism formed by circadian regulation and interventions by food intake, we developed a mathematical model of glucose metabolism in the liver. This mathematical model describes the process of glucose allocation into glycogen and fat (triglyceride), considering the circadian regulation of glycogenesis, glycogenolysis, and fat synthesis. Changing peak phases of glycogenesis and fat synthesis, we calculated two types of possible metabolic dysfunctions: (1) high blood glucose and (2) energy exhaustion. We found that excess fat accumulation from irregular food intake is likely to be a byproduct of preventing energy exhaustion, not high blood glucose. It is suggested that energy depletion has been a problem in mammals from ancient times and that the condition of the circadian regulation has been optimized to avoid the problem. Our model is the first step in understanding the dynamic circadian regulation of glucose metabolism and will be useful to propose an optimal meal schedule to prevent metabolic diseases caused by irregular meal timing in modern society.

1. Introduction

Almost all animals on the earth have a circadian clock, which allows living organisms to synchronize their metabolic, physiological, and behavioral activities with day and night cycles. In mammals, the central clock is located in the suprachiasmatic nucleus (SCN) and regulates behavioral rhythms of sleep/wake and fasting/feeding cycles in response to cyclic environmental changes. Regardless of the rhythmic changes in behavioral aspects, the energy status of cells tends to be homeostatic because of the need to produce a constant supply of energy and derive the precursors necessary for the synthesis of nucleic acids, proteins, carbohydrates, and lipids, even in fluctuating environments. For example, the plasma glucose has a clear circadian rhythm regulated by SCN, which has rising patterns before the onset of the active periods independent of food intake patterns (la Fleur, 2003).

This energy homeostasis is maintained by the orchestration of a multitude of metabolic pathways stimulated by energy intake and expenditure (Inoki et al., 2012; Kumar Jha et al., 2015). Circadian clock regulation is essential for maintaining nutrient homeostasis in response to fluctuating food intake (Asher and Sassone-Corsi, 2015). When food intake occurs during the active period, it ensures the uptake and storage of energy substrates necessary to maintain a high metabolic rate, while during the resting period, stored substrates, such as glycogen and fat, are metabolized to maintain basal energy expenditure. Alterations in feeding timing can desynchronize metabolic rhythms and eventually disturb energy homeostasis (Wang et al., 2011). The synchronization of feeding behaviors and metabolism is therefore critical to ensure the energy supply and maintain internal homeostasis.

With the advancement of civilization, individuals are increasingly working in a manner that is desynchronized with the activities of their biological clock. The misalignment of biological and social time could disrupt the clock, and thus energy homeostasis. Previous studies have suggested that shift workers have an increased risk of metabolic diseases, including obesity, diabetes, metabolic syndromes, and cardiovascular diseases (Shan et al., 2018; Vetter et al., 2018; Wang et al., 2011). As a model of shift work, rodent systems have been used to demonstrate that the dysregulation of the feeding rhythm without an increase in total food intake can lead to obesity (Arble et al., 2009;

Fonken et al., 2010; Hatori et al., 2012; Masaki et al., 2004; Salgado-Delgado et al., 2010; Stucchi et al., 2012). Previous studies have shown that the restriction of food availability only to the light phase (resting period in nocturnal rodents) induces accelerated obesity in mice compared to mice with access to food only during the night that consume the same number of calories (Arble et al., 2009). Furthermore, the correction of the irregular feeding rhythm by scheduled feeding rescues the onset of obesity in mice (Hatori et al., 2012; Stucchi et al., 2012).

The liver is mostly responsible for maintaining energy homeostasis through the coordinated regulation of metabolic pathways, especially those controlling the synthesis and metabolism of glucose, lipids, cholesterol, and bile acids (Bass and Takahashi, 2010). Serum glucose levels remain relatively constant throughout the day by storing glucose as glycogen during feeding and to produce glucose from glycogen breakdown or gluconeogenic precursors during fasting (Rosen and Spiegelman, 2006). Many genes associated with glucose metabolism in the liver exhibit robust circadian regulation (Miller et al., 2007; Panda et al., 2002; Ueda et al., 2002). Activities of rate-limiting enzymes for glycogen accumulation (glycogen synthase) and breakdown (glycogen phosphorylase) occur in cycles under control of the circadian clock in mouse liver, with glycogen levels peaking near the end of the active period (Ishikawa and Shimazu, 1976; Ishikawa and Shimazu, 1980; Roesler and Khandelwal, 1985). Moreover, the core clock component CLOCK directly binds to the promoter of hepatic Gys2, which encodes glycogen synthase 2 (Gys2), the rate-limiting enzyme for glycogenesis, and drives its rhythmic activity, which peaks during the active period in mice (Doi et al., 2010). Like glucose, lipid metabolism also shows clear daily rhythms. Lipogenic genes involved in the process of converting glucose to fatty acids, such as triglycerides for storage, are regulated by the circadian clock and are repressed by Rev-erba/b, the main repressor of the core clock component BMAL1, during the day (Bass and Takahashi, 2010). Adamovich et al. (2014) reported that wild-type mice fed *ad libitum* show circadian expression of liver enzymes that participate in triglyceride biosynthesis, including glycerol-3-phosphate acyltransferase (GPAT), 1-acylglycerol-3-phosphate acyltransferase (AGPAT), lipin (LPIN), and diacylglycerol acyltransferase (DGAT), most of which showed peaks in the active period.

Despite numerous experimental findings on the involvement of circadian regulation of glucose and lipid metabolism in the liver, the optimal regulatory strategy of genes associated with these two different pathways for the maintenance of energy homeostasis remains poorly defined. A mathematical framework is useful to assess the circadian regulation of glycogen production/breakdown and *de novo* lipogenesis/repolysis by evaluating the contribution of time of the day-dependent activation or the repression of each metabolic process in the maintenance of energy homeostasis. Here, we present a mathematical model that describes the dynamics of glycogen and triglyceride contents, two major forms of energy storage in the body that provide the fuel needed during different phases of food deprivation.

Analyses of our model demonstrate that circadian regulation in mammals is optimized to ensure a constant supply of energy. We formulated two types of metabolic risks: energy depletion and high blood glucose. By calculating the optimal phase set of triglycerides and glycogen production for the minimization of each of these risks, we propose that an increased fat accumulation by food intake in the resting period is the byproduct of minimizing either or both energy homeostasis and hyperglycemia risks in the synchronized feeding schedule that animals adopt in nature.

2. Material and methods

2.1 A mathematical model of glucose metabolism

To explore the effect of feeding timing on fat accumulation, we developed a mathematical model that describes the processes of glucose input, consumption, and allocation to glycogen and fat (Fig. 1A). We assume that fat represents triglycerides, which is the main constituent of body fat in humans and other vertebrates. Let x_G, x_F, and x_L be the amount of glucose, fat, and glycogen in the liver, respectively. The amount of glucose (x_G) in the liver is formalized as follows:

$$\dot{x_G} = aL(t) - d_G(t)x_G - (\gamma_L(t)x_G + \gamma_F(t)x_G) + \beta(t)x_L. \quad (1)$$

The amount of glucose increases with food intake $aL(t)$ at time *t* and decreases with consumption at a rate $d_G(t)$. Glucose also decreases with the use of glycogen and fat synthesis. Glycogen, a glucose polymer that functions as

energy storage, is assumed to be synthesized at a rate of $\gamma_L(t)x_G$. Triglyceride synthesis in the liver is stimulated by glycolysis and lipogenesis that enhance glucose flux for the production of precursors for lipid biosynthesis, such as acetyl-CoA. A series of processes for lipid biosynthesis are assumed to occur at a rate $\gamma_F(t)x_G$. The amount of glucose also increases by the breakdown of glycogen at a rate of $\beta(t)$.

We considered two situations for the timing of food intake: (1) a synchronized food schedule in which feeding takes place in the active period and (2) a desynchronized food schedule in which feeding takes place in the resting period (Fig. 1B). We assumed that the resting and active periods occur from zeitgeber time (ZT) 0-11 and from ZT 12-23 of the day, respectively. Based on this assumption, feeding in the active period was formalized by representing $L(t)$ in equation (1) as follows:

$$L(t) = \begin{cases} 0 & 0 \leq t \bmod 24 \leq 12 \\ 1 & 12 < t \bmod 24 \leq 24 \end{cases}. \quad (2a)$$

Similarly, feeding in the resting period was formalized by representing $L(t)$ as follows:

$$L(t) = \begin{cases} 1 & 0 \leq t \bmod 24 \leq 12 \\ 0 & 12 < t \bmod 24 \leq 24 \end{cases}. \quad (2b)$$

Because the metabolic rate decreases in the resting period, we assume that the consumption rates of glucose ($d_G(t)$) and fat ($d_F(t)$) are reduced α in the resting period as follows:

$$d_G(t) = \begin{cases} \alpha d_{GA} & 0 \leq t \bmod 24 \leq 12 \\ d_{GA} & 12 \leq t \bmod 24 \leq 24 \end{cases}, \quad (3a)$$

and

$$d_F(t) = \begin{cases} \alpha d_{FA} & 0 \leq t \bmod 24 \leq 12 \\ d_{FA} & 12 \leq t \bmod 24 \leq 24 \end{cases}, \quad (3b)$$

where $0 < \alpha < 1$.

Three processes in the glucose dynamics in the model are assumed to be regulated by the circadian clock. Doi et al. (2010) reported that *Clock* gene mutation in mice damped the circadian oscillation of hepatic glycogen and glycogen synthase 2 (Gys2), suggesting that the rate of glycogenesis indicated

$\gamma_L(t)$ in equation (1) is influenced by the circadian clock. A previous study showed that a lack of a functional PER2 protein (*Per2*^{Brdm1}) results in increased glycogen phosphorylase activity during the fasting phase in mice (Zani et al., 2013). This finding implies that the glycogenolysis rate, $\beta(t)$, is also regulated by the circadian clock. Moreover, the rate of triglyceride production $\gamma_F(t)$ is suggested to be regulated by the circadian clock, as Clock-disrupted (*Per1/2* -/-) mice showed a phase shift of hepatic triglyceride levels (Adamovich et al., 2014).

We incorporated the circadian regulation of the rate of fat synthesis ($\gamma_F(t)$), glycogenesis ($\gamma_L(t)$) and glycogenolysis $\left(\gamma_\beta(t)\right)$ into the model by introducing a sinusoidal function with a period of 24 h ($\tau = 24$) for each as follows:

$$\gamma_i(t) = \frac{(a_i - b_i)\left(cos\left(\frac{2\pi(t-\varphi_i)}{\tau}\right)+1\right)}{2} + b_i, \tag{4}$$

where $i = F, L,$ and β. a_i, b_i, and φ_i correspond to the upper limit, lower limit, and phase of each process.

The amount of fat and glycogen, x_F, and x_L, are formalized as;

$$\dot{x_F} = \gamma_F(t)x_G - d_F x_F, \tag{5}$$

$$\dot{x_L} = \gamma_L(t)x_G - \gamma_\beta(t)x_L. \tag{6}$$

The amount of fat (x_F) is increased by the production from glucose at a rate of $b\gamma_F(t)$ and consumed as an energy source at a rate of d_F (Eq. (5)). The amount of glycogen (x_L) is increased by the production of glucose at a rate of $b\gamma_L(t)$ and decomposed into glucose at a rate of $\gamma_\beta(t)$ (Eq. (6)). Note that x_F and x_L are normalized variables indicating the relative amount of fat and glycogen formed by a single molecule of glucose.

2.2 Risks of energy depletion and hyperglycemia

Based on the above model, next, we examined the optimal phase set for glycogen and fat synthesis that minimizes two different risks: energy homeostasis and hyperglycemia. We assumed that increased fat accumulation by food intake in the resting period could be the byproduct of minimizing either energy

homeostasis or hyperglycemia risks in the synchronized feeding schedule that animals adopt in nature. If this is true, organisms employing the optimal phase set for minimization of these risks should reveal increased fat accumulation when they feed in the desynchronized feeding schedule. We tested this prediction for the two different types of risks using our model.

The first is the risk of energy depletion caused by disruption of energy homeostasis. To define the energy level at time t ($E(t)$), we focused on ATPs, the source of energy in many living organisms, which are produced from glucose and fat.

$$E(t) = f_G d_G(t) x_G + f_F d_F(t) x_F. \tag{7a}$$

f_G and f_F indicate the number of ATPs produced from glucose and fat, respectively. From one molecule of glucose, about 30 ATPs were obtained as a result of aerobic respiration and $f_G = 30$. On the other hand, from one molecule of palmitic acid, 106 ATPs were produced through β-oxidation. If we consider that one molecule of triglyceride consists of three palmitic acids, $f_F = 106 \times 3 = 318$. Thus, the relative ATP production efficiency is $f = f_F / f_G$, represented by E^*, as follows:

$$E^* = \frac{E(t)}{f_G} = d_G(t) x_G + f d_F(t) x_F. \tag{7b}$$

The risk of energy depletion is defined as the cumulative sum of $E(t)$ below a certain threshold, as follows:

$$C_E = \int_n^{n+48} \{\max\{(E_L - E^*), 0\}\} dt, \tag{8a}$$

where E_L is the lower threshold above which there is no damage to energy exhaustion. To examine the phase combination that optimizes energy homeostasis, we evaluated $E(t)$ the $24 \times 24 = 576$ combinations of φ_F and φ_L by changing each phase by 1 h.

The second risk is hyperglycemia, which is a major problem in diabetes, with the potential to cause neuropathy (Albers and Pop-Busui, 2014) and retinopathy (Antonetti et al., 2012). The level of hyperglycemia can be defined as the cumulative sum of the glucose level above a certain threshold, as follows:

$$C_G = \int_n^{n+48} \{\max\{(x_G(t) - x_G^U), 0\}\} dt\,, \qquad (8b)$$

where x_G^U is the upper threshold of glucose level below which there is no risk of organ damage. Examples of the cost of high glucose level and energy exhaustion are presented in Figure 2A and 2B, respectively. C_E and C_G are calculated under the condition of a synchronized food schedule (Fig. 1B(I)).

2.3 Index to measure an increased fat accumulation by food intake in the resting time

To study the phase combinations of glycogenesis (φ_L) and fat synthesis (φ_F), in which increased fat gain from food intake in the resting periods was achieved (Salgado-Delgado et al., 2010), we calculated the index measuring the difference in daily triglyceride accumulation between synchronized and desynchronized food schedules. The index, denoted as Δfat, is provided as follows:

$$\Delta fat = \int_m^{m+120} \{x_F^D(t) - x_F^S(t)\} dt\,, \qquad (9)$$

where $x_F^D(t)$ and $x_F^S(t)$ represent the level of fat accumulated at time *t* under desynchronized and synchronized food schedules, respectively. Δfat is calculated over 120 h from the starting time m. For our calculation, we examined $24 \times 24 = 576$ combinations of φ_F and φ_L by changing each phase by 1 h.

2.4 Parameter values used for numerical calculation of the model

The parameter values used in the model are listed in Table 1. Some parameters were fixed to focus on the effects of circadian phases of fat synthesis (φ_L) and glycogenesis (φ_F) on glucose metabolism. The peak time of glycogenolysis was fixed at $\varphi_\beta = 6$, namely at the middle of the resting time, because the rate-limiting enzyme of glycogenolysis, such as glycogen phosphorylase (Pygl), showed peak expression levels during the early resting period (Greenwell et al., 2019; Kim et al., 2017).

Other parameters associated with the period and amplitude of oscillation were also fixed (Table 1). We fixed $x_G^U = 2$ and $E_L = 4$ on the cost calculations and chose two cycles, starting from $n = 60$ in Eq. (9a) and (9b),

respectively. The threshold dependences on the costs are discussed in Appendix A. Our conclusion did not depend on x_G^U but depended on E_L, as discussed in Appendix A. We also fixed the relative ATP production efficiency $f = 10.6$ (section 3.2), and discuss the f dependence on cost calculation in section 4 (Discussion) and Appendix B.

3. Results

3.1. Minimizing the risk of energy depletion

The risk of energy depletion (C_E) (Eq. (8a)) was minimized when the peak time of fat synthesis (φ_F) was set at the end of the resting period and that of glycogen synthesis was set at the end of the active period (minimum risk (35.33) was realized at $(\varphi_F, \varphi_L) = (11,22)$) (Fig. 3A, 3B).

This desynchronized timing of fat and glycogen synthesis is effective for a continuous supply of energy, resulting in a reduced risk of energy depletion that is most likely to occur at the end of the resting period ($t = 12$) in all combinations of phases for glycogen and fat synthesis (Fig. 3B) because of the absence of glucose inputs during the resting period under a synchronized food schedule (Fig. 1B(I)). The risk of energy depletion decreased when fat synthesis peaked during the resting period, and the peak of glycogen production was set at the end of the active period (e.g. $(\varphi_F, \varphi_L) = (6,0)$ or $(12,0)$; Fig. 3C) due to the continuous supply of energy mainly from fat at the end of the resting period (dotted lines in $(\varphi_F, \varphi_L) = (6,0)$ or $(12,0)$) (Fig. 3D).

When the phase of fat synthesis (φ_F) was set during the resting period, the energy supply from glucose in the active period and that from fat in the resting period was balanced for a continuous supply of energy regardless of circadian time. The energy supply from glucose was high during the active period and low during the resting period regardless of the phase of glycogen synthesis, due to food intake during the active period in the synchronized food schedule (solid lines in Fig. 3D). On the contrary, energy supply from fat significantly depended on the phase of fat synthesis (dotted lines in Fig. 3D). When the peak of fat synthesis was set during the resting periods, energy supply

from fat peaked during the resting periods, which compensated for the lack of energy at the end of resting periods due to no food intake (dotted lines in Fig. 3D).

When the peak phase of glycogen production (φ_L) was set at the end of the active periods ($\varphi_L = 0$), a low risk of energy depletion was achieved (Fig. 3A and 3C). This is because the energy depletion due to the lack of glucose at the end of the resting periods ($t = 12$) was moderated ($\varphi_L = 0$) (Fig. 3B). If $\varphi_L = 0$, the glucose allocation rate to glycogen was minimized at the end of the resting period ($t = 12$), which resulted in low glucose consumption when a lack of glucose was likely to occur.

3.2. The risk of hyperglycemia was low at the peak of fat synthesis during the active period

The risk of hyperglycemia (C_G) (Eq. (8b)) was low when fat synthesis peaked during the active periods, as well as when glycogen synthesis peaked at the end of the active periods (minimum risk (255.29) is shown $(\varphi_F, \varphi_L) = (18,1)$ in Fig. 3E; the time course of the risk is shown in 3F). This result indicates that glucose allocation to both glycogen and fat during the feeding phase and preventing excess levels of glucose are key to realizing the low risks of hyperglycemia.

The risk of hyperglycemia depends mainly on the peak time of glycogen synthesis (Fig. 3F). When the peak time was set around the end of the active periods ($\varphi_F = 23\ or\ 0$) (Fig. 3E), the glycogen production rate increased with time during the active period, which contributes to avoiding excess glucose by allocating glucose to glycogen during the feeding phase.

When the peak phase of fat synthesis (φ_F) was shifted from that of glycogen synthesis (φ_L), the risk of hyperglycemia became low (e.g. $(\varphi_F, \varphi_L) = (18,0), (18,6), (0,12), (0,18)$ in Fig. 3G). Glucose allocation to fat contributed to reducing the amount of glucose leftover when glycogen was inactively produced. As mentioned above, low hyperglycemia risks were achieved when the glycogen synthesis peak occurred at the beginning of the

resting period ($\varphi_L = 0$) and the fat production peak in the middle of the active periods ($\varphi_F = 18$), further reducing the excess glucose during the feeding phases (Fig. 3G).

3.3 Fat synthesis synchronized with glucose input causes increased fat accumulation with food intake in the resting period

Next, we examined whether the fat accumulation from food intake during the resting periods observed in rodents (Arble et al., 2009; Salgado-Delgado et al., 2010) was reproduced at the optimal conditions to prevent energy depletion or hyperglycemia. Increased fat accumulation by food intake in the resting period, represented by positive Δfat, was achieved when the peak time of fat synthesis (φ_F) ranged from the resting period to the beginning of the active period, regardless of the phase of glycogen synthesis (Fig. 4). This result indicates the importance of synchrony between fat synthesis peak and the timing of glucose input for the realization of increased fat accumulation by food intake in the resting period. The phase of glycogen synthesis has almost no effect on Δfat.

The phase combination optimal for preventing energy depletion, $(\varphi_F, \varphi_L) = (11,22)$, was within the parameter region in which positive Δfat was realized (Fig. 4). However, the phase combination optimal for preventing high blood glucose, $(\varphi_F, \varphi_L) = (18,1)$, was out of the parameter region. Thus, this result suggests that increased fat accumulation by food intake in the resting period could be the byproduct of the optimization of phases for minimizing the risk of energy depletion.

Circadian regulation of glycogen, and fat production rates and glycogenolysis rate (γ_F, γ_L, and γ_β) contributed to the reduction of the risks of energy depletion and hyperglycemia. Without the circadian oscillation of the production rates (i.e. when γ_F, γ_L, and γ_β are fixed at mean values of the maximum and minimum levels in Table 1), the two types of risks were larger than the minimum risks achieved at the optimal phase conditions: $(\varphi_F, \varphi_L) = (11,22)$ and $(18,1)$ (Appendix C). In addition, the circadian oscillation realized robust rhythmicity of the supply of glucose, glycogen, and fat

independent from the fluctuation of feeding timings. Without circadian oscillation of the production rates, the peak time of the abundance of glucose, glycogen, and fat were shifted by 12 h, changing the feeding schedule represented by Eq. (2a) and (2b). In contrast, with the circadian oscillation, the shift of peak phases of the abundance caused by the change in the feeding schedule (Eq. (2a) and (2b)) was moderated (Appendix C).

4. Discussion

In this study, we aimed to understand the circadian regulation of glucose metabolism, that is, the mechanism behind phenomena such as the accumulation of excess fat as a result of irregular meal timings. Using a mathematical model, we described the processes of glucose allocation to glycogen or triglycerides regulated by the circadian clock. As a result, we confirmed the optimal phases that minimized two risks: (1) energy depletion, an important factor for animals to reduce to prepare for urgent demand of energy, and (2) hyperglycemia, a key health problem in modern society. Both risks were calculated considering the case of nocturnal animals under a 12/12 h light (resting)/dark (active) cycle. Both risks were found to be minimized when the peak of glycogen synthesis was set at the end of the active period. On the other hand, the optimal peaks of fat (triglyceride) synthesis were different between the two risks; ZT11, the end of the resting period was optimal to prevent energy depletion, while ZT18 in the middle of the active period was optimal to prevent hyperglycemia. Secondly, increased fat accumulation from food intakes during resting periods, as observed in rodents (Arble et al., 2009; Salgado-Delgado et al., 2010), was realized under optimal conditions for preventing energy depletion, but not for hyperglycemia. This suggests that the circadian regulation of glucose metabolism in mammals may be optimized to prevent energy depletion, and the observed dysregulation of fat metabolism in our society may be a byproduct of an adaptation to food shortage that animals have faced in their evolutionary history. This adaptive response in the past environments can result in a mismatch in the dietary habits in modern society in which humans can obtain food anytime they need.

We assumed that the processes of glucose allocation into glycogen and

triglycerides were regulated by the circadian clock in our model, as elucidated in experimental studies. In particular, recent studies have suggested that the core component genes of the circadian clock are important factors for regulating glucose and lipid metabolism in the liver (Adamovich et al., 2014; Doi et al., 2010; Liu et al., 2013; Zani et al., 2013), although the downstream molecular targets of these genes remain to be identified.

Recent studies have investigated the mechanism of regulation of Gys2 expression by core clock components. PER2 binds to the gene binding sites of Gys2 and some negative regulators of glycogenolysis (Zani et al., 2013), while CLOCK activates Gys2 expression via two E-boxes (Doi et al., 2010). Our current model simplified the process by focusing on oscillations that emerged from the gross effect of all components of glycogen and triglycerides production, represented by cosinusoidal curves. The model can be extended to incorporate the regulation of circadian clock components in the molecular metabolic networks related to glycogen and fat synthesis in future studies.

We demonstrated that the risk of energy depletion was minimized when the peak phases of glycogen (φ_L) and fat production (φ_F) were set at the end of the active (around ZT0) and resting periods (around ZT12), respectively. The optimal phase set was consistent with the peak phases of hepatic glycogen and triglycerides in rodents. The level of hepatic glycogen peaked at the beginning of the resting period (Doi et al., 2010), and triglycerides peaked around the end of the resting period (ZT8; Adamovich et al., 2014). We considered fast reaction in the transcription, translation processes of multiple rate-limiting enzymes and resultant production glycogen and fat, and thus the peaks in abundances of transcripts, proteins, and glycogen and fat are synchronized in the model. However, these processes are not synchronized and there are delays at least several hours in real liver systems. Incorporation of delayed metabolic reaction will enable the direct comparison of the predicted optimal peak phases of glycogen (φ_L) and fat production (φ_F) and observed peak phases of rate-limiting enzymes for glycogen and fat synthesis, respectively.

In fact, when we compared the peak time of the enzyme or protein abundance associated with glycogen and fat synthesis, discrepancies were observed between the

model prediction and the data. In glycogenesis, Gys2 (glycogen synthase 2) gene expression peaked at the beginning of the active period (ZT=12), while GYS2 protein peaked in the middle of the active periods (ZT=20; Doi et al., 2010), which are both different from the optimal φ_L (ZT $= 22$). In lipogenesis, there are several pathways, such as *de novo* lipogenesis, where fatty acids are produced from citrate (intermediate of the TCA cycle), and glycerol-3-phosphate pathway, where glycerol-3-phosphate and fatty acids are transformed into triglycerides (Saponaro et al., 2015). The peak phase of ACC1, the rate-limiting enzyme of *de novo* lipogenesis, occurred at the end of the resting period (ZT=12; Liu et al., 2013), while the peak phase of *Gpat2* expression, the rate-limiting enzyme of the glycerol-3-phosphate pathway in lipogenesis, occurred at the beginning of the resting time (ZT=0; Adamovich et al., 2014). The phase of ACC1 was close to the optimal φ_F (ZT $= 11$), but varied from the *Gpat2* expression phase by 12 h.

In our model, φ_L and φ_F represent the phases of the total production processes of glycogen and triglycerides, respectively, and not the phase of a particular pathway. To compare the optimal φ_L and φ_F with the experimental data, we estimated the peak phases of the most rate-limiting pathways of glycogen and triglyceride production. Here, we did not consider the time delay of each process in the model, which may have caused a mismatch between the optimal phases derived by our calculation and the peak phases of gene expression and enzymes.

The combination of the optimal phases of fat and glucose production (φ_F, φ_L) depended on the parameter f, the relative efficiency of fat, as an energy resource. The optimal (φ_F, φ_L) did not change when f increased from 10.6 to 15.0. However, when f was 5.0, the optimal phase of fat production (φ_F) was synchronized with that of glycogen production rate (φ_L), while the optimal phases of fat and glycogen production shifted at f above 10.6. When fat is about 10 times more efficient as an energy resource than glucose ($f = 10.6$), fat can compensate for the lack of glucose during fasting phases, and the shifted timing of fat and glycogen production may be a good strategy. This is discussed in detail in Appendix B.

The fluctuation of meal timings has a large effect on metabolic homeostasis. Considering the case in humans, food intake can be divided into three main time points,

namely breakfast, lunch, and dinner. Delaying the timings of the three meals causes a delay in the plasma glucose rhythm and peripheral clock gene expression (Wehrens et al., 2017). Moreover, specific patterns of the dietary contents of breakfast, lunch, and dinner have been associated with risks for hyperglycemia (Shi et al., 2017). These phenomena related to meal timings and nutrient content could be explained by extending the model considering food intake divided into several timings and different amounts of glucose and other nutrients in each meal.

The length of light and dark phases is also an environmental fluctuation factor in regions other than the tropical area. The length of the active and resting periods is fixed at 12/12 h in this study, and the patterns can be varied to examine the schedule of shift workers. Epidemiological studies have found that shift workers are likely to experience obesity (Di Lorenzo et al., 2003). Tsai et al. (2005) shifted the light-dark cycle of rats 12 h for three days in a week and found that the shifted light exposure enhanced weight gain.

The entrainment of the circadian clock is also an important factor for nutrient homeostasis. Studies have revealed that the peripheral clock in the liver is modulated by food factors (Kuroda et al., 2012; Oike, 2017; Shimizu et al., 2018; Stokkan et al., 2001). Shimizu et al. (2018) revealed that delaying breakfast altered the phases of Clock genes, lipid metabolism-related genes, and glucose metabolism-related genes in the liver. Similarly, Kuroda et al. (2012) examined multiple conditions mimicking human meal timings in mice and found that the meal after the longest interval has the largest effect on the phase of PER2 in the liver. Moreover, insulin plays an important role in the regulation of blood glucose and the entrainment of the circadian clock (Crosby et al., 2019). In the delayed breakfast mouse model, serum insulin levels were also delayed (Shimizu et al., 2018). The flexible adjustment of the peripheral clock to a fluctuating environment is important for nutrient homeostasis. To understand the mechanism of entrainment by meal timings, it is necessary to develop a multi-scaled mathematical model that consists of the gene network and the metabolite dynamics responding to glucose input occurring at different times. Moreover, the entrainment of the circadian clock is also influenced by exercise (Tahara et al., 2017; Tahara and Shibata, 2018). This suggests that the activity pattern of individuals may have an effect

on entrainment and nutrition homeostasis, which is important for predicting optimal meal schedules. Our model could also be used as a basic framework to understand the necessity of flexible entrainment of the circadian clock in mammals by considering nutrient homeostasis, by which we may elucidate the reasons for the circadian clock in mammals being partly independent and the adaptation of this clock to environmental perturbation.

Acknowledgments

This work was done by the JSPS Research Fellowship (DC1) and Grant-in-Aid for JSPS Fellows to A.H (18J20316). We are grateful to Camila Caldana, Yusuke Nakane, and Shigenobu Shibata for their helpful advice from the point of view of experimental research. We also thank Shingo Gibo, Hiroshi Ito, Gen Kurosawa, and Motohide Seki for their useful comments on mathematical modeling.

References

Adamovich, Y., Rousso-Noori, L., Zwighaft, Z., Neufeld-Cohen, A., Golik, M., Kraut-Cohen, J., Wang, M., Han, X., Asher, G., 2014. Circadian clocks and feeding time regulate the oscillations and levels of hepatic triglycerides. Cell Metab. 19(2), 319–330. https://doi.org/10.1016/j.cmet.2013.12.016.

Albers, J.W., Pop-Busui, R., 2014. Diabetic neuropathy: Mechanisms, emerging treatments, and subtypes. Curr. Neurol. Neurosci. Rep. 14(8), 473. https://doi.org/10.1007/s11910-014-0473-5.

Antonetti, D. A., Klein, R., Gardner, T. W., & Antonetti. (2012). Diabetic retinopathy. *The New England Journal of Medicine*, *366*(13), 1227–1239. https://doi.org/10.2174/157339909787314130

Arble, D.M., Bass, J., Laposky, A.D., Vitaterna, M.H., Turek, F.W., 2009. Circadian timing of food intake contributes to weight gain. Obesity 17(11), 2100–2102. https://doi.org/10.1038/oby.2009.264.

Asher, G., Sassone-Corsi, P., 2015, March 26. Time for food: The intimate interplay between nutrition, metabolism, and the circadian clock. Cell 161(1), 84–92. https://doi.org/10.1016/j.cell.2015.03.015.

Bass, J., Takahashi, J.S., 2010. Circadian integration of metabolism and energetics. Science 330(6009), 1349–1354 LP – 1354. https://doi.org/10.1126/science.1195027.

Crosby, P., Hamnett, R., Putker, M., Hoyle, N.P., Reed, M., Karam, C.J., Maywood, E.S., Stangherlin, A., Chesham, J.E., Hayter, E.A., Rosenbrier-Ribeiro, L., Newham, P., Clevers, H., Bechtold, D.A., O'Neill, J.S., 2019. Insulin/IGF-1 drives PERIOD synthesis to entrain circadian rhythms with feeding time. Cell 177(4), 896–909.e20. https://doi.org/10.1016/j.cell.2019.02.017.

Di Lorenzo, L., De Pergola, G., Zocchetti, C., L'Abbate, N., Basso, A., Pannacciulli, N., Cignarelli, M., Giorgino, R., Soleo, L., 2003. Effect of shift work on body mass index: Results of a study performed in 319 glucose-tolerant men working in a Southern Italian industry. Int. J. Obes. 27(11), 1353–1358. https://doi.org/10.1038/sj.ijo.0802419.

Doi, R., Oishi, K., Ishida, N., 2010. CLOCK regulates the circadian rhythms of hepatic glycogen synthesis through transcriptional activation of Gys2. J. Biol. Chem. 285(29), 22114–

22121. https://doi.org/10.1074/jbc.M110.110361.

Fonken, L.K., Workman, J.L., Walton, J.C., Weil, Z.M., Morris, J.S., Haim, A., Nelson, R.J., 2010. Light at night increases body mass by shifting the time of food intake. Proc. Natl Acad. Sci. U. S. A. 107(43), 18664–18669. https://doi.org/10.1073/pnas.1008734107.

Gómez-Ulla, F., 2009. Diabetic retinopathy. Curr. Diabetes Rev. 5(1), 1–2. https://doi.org/10.2174/157339909787314130.

Greenwell, B.J., Trott, A.J., Beytebiere, J.R., Pao, S., Bosley, A., Beach, E., Finegan, P., Hernandez, C., Menet, J.S., 2019. Rhythmic food intake drives rhythmic gene expression more potently than the hepatic circadian clock in mice. Cell Rep. 27(3), 649–657.e5. https://doi.org/10.1016/j.celrep.2019.03.064.

Hatori, M., Vollmers, C., Zarrinpar, A., DiTacchio, L., Bushong, E.A., Gill, S., Leblanc, M., Chaix, A., Joens, M., Fitzpatrick, J.A.J., Ellisman, M.H., Panda, S., 2012. Time-restricted feeding without reducing caloric intake prevents metabolic diseases in mice fed a high-fat diet. Cell Metab. 15(6), 848–860. https://doi.org/10.1016/j.cmet.2012.04.019.

Inoki, K., Kim, J., Guan, K.L., 2012. AMPK and mTOR in cellular energy homeostasis and drug targets Annu. Rev. Pharmacol. Toxicol. 52(1), 381–400. https://doi.org/10.1146/annurev-pharmtox-010611-134537.

Ishikawa, K., Shimazu, T.,1976. Daily rhythms of glycogen synthetase and phosphorylase activities in rat liver: Influences of food and light. Life Sci. 19(12), 1873–1878’

Ishikawa, K., Shimazu, T., 1980. Circadian rhythm of liver glycogen metabolism in rats: Effects of hypothalamic lesions Am. J. Physiol. 238(1), E21–E25.

Kim, H., Zheng, Z., Walker, P.D., Kapatos, G., Zhang, K., 2017. CREBH maintains circadian glucose homeostasis by regulating hepatic glycogenolysis and gluconeogenesis. Mol. Cell. Biol. 37(14). https://doi.org/10.1128/MCB.00048-17.

Kumar Jha, P., Challet, E., Kalsbeek, A., 2015. Circadian rhythms in glucose and lipid metabolism in nocturnal and diurnal mammals Mol. Cell. Endocrinol. 418(1), 74–88. https://doi.org/10.1016/j.mce.2015.01.024.

Kuroda, H., Tahara, Y., Saito, K., Ohnishi, N., Kubo, Y., Seo, Y., Otsuka, M., Fuse, Y., Ohura, Y., Hirao, A., Shibata, S., 2012. Meal frequency patterns determine the phase of mouse peripheral circadian clocks. Sci. Rep. 2, 711. https://doi.org/10.1038/srep00711.

la Fleur, S.E., 2003. Daily rhythms in glucose metabolism: Suprachiasmatic nucleus output to peripheral tissue. J. Neuroendocrinol. 15(3), 315–322. https://doi.org/10.1046/j.1365-2826.2003.01019.x.

Liu, S., Brown, J.D., Stanya, K.J., Homan, E., Leidl, M., Inouye, K., Bhargava, P., Gangl, M.R., Dai, L., Hatano, B., Hotamisligil, G.S., Saghatelian, A., Plutzky, J., Lee, C.H., 2013. A diurnal serum lipid integrates hepatic lipogenesis and peripheral fatty acid use. Nature 502(7472), 550–554. https://doi.org/10.1038/nature12710.

Masaki T, Chiba S, Yasuda T, Noguchi H, Kakuma T, Watanabe T, Sakata T, Yoshimatsu H, 2004. Involvement of the hypothalamic histamine H1 receptor in the regulation of feeding rhythm and obesity Diabetes 53(9), 2250–2260. https://doi.org/10.2337/diabetes.53.9.2250.

Miller, B.H., McDearmon, E.L., Panda, S., Hayes, K.R., Zhang, J., Andrews, J.L., Antoch, M.P., Walker, J.R., Esser, K.A., Hogenesch, J.B., Takahashi, J.S., 2007. Circadian and CLOCK-controlled regulation of mouse transcriptome and cell proliferation. Proc. Natl Acad. Sci. U. S. A. 104(9), 3342–3347. https://doi.org/10.1073/pnas.0611724104.

Oike, H., 2017. Modulation of circadian clocks by nutrients and food factors Biosci. Biotechnol. Biochem. 81(5), 863–870. https://doi.org/10.1080/09168451.2017.1281722.

Panda, S., Antoch, M.P., Miller, B.H., Su, A.I., Schook, A.B., Straume, M., Schultz, P.G., Kay, S.A., Takahashi, J.S., Hogenesch, J.B., 2002. Coordinated transcription of key pathways in mice by the circadian clock. Cell 109(3), 307–320. https://doi.org/10.1016/S0092-8674(02)00722-5.

Roesler, W. J., Khandelwal, R. L., 1985. Diurnal variations in the activities of the glycogen metabolizing enzymes in mouse liver Int. J. Biochem. 17(1), 81–85.

Rosen, E.D., Spiegelman, B.M., 2006. Adipocytes as regulators of energy balance and glucose homeostasis Nature 444(7121), 847–853. https://doi.org/10.1038/nature05483.

Salgado-Delgado, R., Angeles-Castellanos, M., Saderi, N., Buijs, R.M., Escobar, C., 2010. Food intake during the normal activity phase prevents obesity and circadian desynchrony in a rat model of night work. Endocrinology 151(3), 1019–1029. https://doi.org/10.1210/en.2009-0864.

Saponaro, C., Gaggini, M., Carli, F., Gastaldelli, A., 2015. Subtle balance between lipolysis and lipogenesis: A critical point in metabolic homeostasis. Nutrients 7(11), 9453–9474.

https://doi.org/10.3390/nu7115475.

Shan, Z., Li, Y., Zong, G., Guo, Y., Li, J., Manson, J.E., Hu, F. B., Willett, W. C., Schernhammer, E. S., Bhupathiraju, S.N., 2018. Rotating night shift work and adherence to unhealthy lifestyle in predicting risk of type 2 diabetes: Results from two large US cohorts of female nurses. BMJ 363, k4641. https://doi.org/10.1136/bmj.k4641.

Shi, Z., Riley, M., Taylor, A., Noakes, M., 2017. Meal-specific food patterns and the incidence of hyperglycemia in a Chinese adult population. Br. J. Nutr. 118(1), 53–59. https://doi.org/10.1017/S000711451700174X.

Shimizu, H., Hanzawa, F., Kim, D., Sun, S., Laurent, T., Umeki, M., Ikeda, S., Mochizuki, S., & Oda, H. (2018). Delayed first active-phase meal, a breakfastskipping model, led to increased body weight and shifted the circadian oscillation of the hepatic clock and lipid metabolism-related genes in rats fed a high-fat diet. *PLoS ONE*, *13*(10), 1–17. https://doi.org/10.1371/journal.pone.0206669

Stokkan, K.A., Yamazaki, S., Tei, H., Sakaki, Y., Menaker, M., 2001. Entrainment of the circadian clock in the liver by feeding. Science 291(5503), 490–493. https://doi.org/10.1126/science.291.5503.490.

Stucchi, P., Gil-Ortega, M., Merino, B., Guzmán-Ruiz, R., Cano, V., Valladolid-Acebes, I., Somoza, B., Le Gonidec, S., Argente, J., Valet, P., Chowen, J.A., Fernández-Alfonso, M., Ruiz-Gayo, M., 2012. Circadian feeding drive of metabolic activity in adipose tissue and not hyperphagia triggers overweight in mice: Is there a role of the pentose-phosphate pathway? Endocrinology 153(2), 690–699. https://doi.org/10.1210/en.2011-1023.

Tahara, Y., Aoyama, S., Shibata, S., 2017. The mammalian circadian clock and its entrainment by stress and exercise J. Physiol. Sci. 67(1), 1–10. https://doi.org/10.1007/s12576-016-0450-7.

Tahara, Y., Shibata, S., 2018. Entrainment of the mouse circadian clock: Effects of stress, exercise, and nutrition. Free Radic. Biol. Med. 119(December 2017), 129–138. https://doi.org/10.1016/j.freeradbiomed.2017.12.026.

Tsai, L.L., Tsai, Y.C., Hwang, K., Huang, Y.W., Tzeng, J.E., 2005. Repeated light-dark shifts speed up body weight gain in male F344 rats. Am. J. Physiol. Endocrinol. Metab. 289(2), E212–E217. https://doi.org/10.1152/ajpendo.00603.2004.

Ueda, H.R., Chen, W., Adachi, A., Wakamatsu, H., Hayashi, S., Takasugi, T., Nagano, M., Nakahama, K.I., Suzuki, Y., Sugano, S., Iino, M., Shigeyoshi, Y., Hashimoto, S., 2002. A transcription factor response element for gene expression during the circadian night. Nature 418(6897), 534–539. https://doi.org/10.1038/nature00906.

Vetter, C., Dashti, H.S., Lane, J.M., Anderson, S.G., Schernhammer, E.S., Rutter, M.K., Saxena, R., Scheer, F.A.J.L., 2018. Night shift work, genetic risk, and type 2 diabetes in the UK Biobank. Diabetes Care 41(4), 762–769. https://doi.org/10.2337/dc17-1933.

Wang, X.S., Armstrong, M.E.G., Cairns, B.J., Key, T.J., Travis, R.C., 2011. Shift work and chronic disease: epidemiological evidence. Occup. Med. 61(2), 78–89. https://doi.org/10.1093/occmed/kqr001.

Wehrens, S.M.T., Christou, S., Isherwood, C., Middleton, B., Gibbs, M.A., Archer, S.N., Skene, D.J., Johnston, J.D., 2017. Meal timing regulates the human circadian system Curr. Biol. 27(12), 1768–1775.e3. https://doi.org/10.1016/j.cub.2017.04.059.

Zani, F., Breasson, L., Becattini, B., Vukolic, A., Montani, J.P., Albrecht, U., Provenzani, A., Ripperger, J.A., Solinas, G., 2013. PER2 promotes glucose storage to liver glycogen during feeding and acute fasting by inducing Gys2 PTG and GL expression. Mol. Metab. 2(3), 292–305. Available online: https://doi.org/https. https://doi.org/10.1016/j.molmet.2013.06.006.

Appendix A

Dependence of costs on the threshold of hyperglycemia and energy depletion

In this Appendix, we discuss the dependency of energy depletion costs on the values of thresholds x_G^U and E_L. In sections 3.2 and 3.3, we calculated the risks of energy exhaustion (C_E) and hyperglycemia (C_G) setting $x_G^U = 2.0$ and $E_L = 4.0$ in Eq. (9a) and (9b), based on the two regulations. First, we set thresholds that did not result in $C_E = 0$ or $C_G = 0$ in multiple conditions of (φ_F, φ_L) so as to choose one condition that achieves the lowest risk. Second, we did not consider the cases where the energy levels were below the threshold throughout the period. We considered that if a chronic lack of energy occurs, the animal cannot survive and the amount of food intake $L(t)$ will increase. Varying x_G^U and E_L, these regulations are violated under certain conditions as follows.

A.1 Threshold of energy exhaustion

We calculated the risks of energy exhaustion by varying the threshold to $E_L = 2.0,\ 4.0,\ 8.0$ (Fig. A.1). The result of $E_L = 4.0$ was the same as the result shown in section 3.1.

When we set $E_L = 2.0$, the threshold was too low to evaluate the best conditions. This is because some conditions of (φ_F, φ_L) resulted in $C_E = 0$ (black cells in Fig. A.1) and we could not find the optimum (φ_F, φ_L).

In contrast, when we set $E_L = 8.0$, the threshold was too high because the peaks of energy levels were below the threshold $E_L = 8.0$ in some (φ_F, φ_L). Furthermore, energy exhaustion occurred throughout the day, even in the feeding phases. Under such conditions, the lowest risk was achieved $(\varphi_F, \varphi_L) = (0,21)$ in the condition where φ_F was during the active period, which is differs from $E_L = 4.0$. Therefore, the threshold of energy exhaustion has an effect on the result of searching for the condition of lowest risks.

A.2 Threshold of hyperglycemia

We calculated the risks of hyperglycemia by varying the threshold to $x_G^U = 1.0,$

$2.0,\ 4.0$ (Fig. A.2). The result of $x_G^U = 2.0$ is shown in section 3.2 (the lowest risk was achieved in $(\varphi_F, \varphi_L) = (18,1)$).

When we set $x_G^U = 1.0$, the condition of lowest risk was achieved at $(\varphi_F, \varphi_L) = (19,4)$. When we set $x_G^U = 4.0$, many conditions of (φ_F, φ_L) achieved $C_G = 0$ (Fig. A.2) and the threshold was too low to find the best condition for the lowest C_G. The conclusion did not depend on x_G^U much compared to E_L. This is because the glucose levels declined to near zero during fasting phases, and the lack of glucose occurred in all of the conditions during the resting periods. Then, chronic hyperglycemia did not occur where $x_G^U = 1.0,\ 2.0,\ 4.0$, unlike in the case of varying E_L.

Appendix B

Dependence of costs on relative ATP production efficiency

In this Appendix, we discuss the dependency of energy depletion costs on the relative ATP production efficiency, denoted by f in Eq. (8b). A larger f represents a higher fat efficiency as an energy resource compared to the efficiency of glucose. We calculated the costs for energy depletion to vary $f = 5.0, 10.6,$ and 15.0 (Fig. B). In section 3.1, we set $f = \frac{f_F}{f_G} = \frac{318}{30} = 10.6$ as a basal value (Fig. B(ii)), where f_F and f_G are the number of ATPs produced from one molecule of triglyceride and glucose. We examined the smaller value $f = 5.0$ (Fig. B(i)) and the larger value $f = 15.0$ (Fig. B(iii)).

The optimal timing of glycogenesis (φ_L) did not depend on f and the risks of energy depletion were minimum around $\varphi_L = 23$ (Fig. B(i), (ii), and (iii)). To maintain the glycogen level during the resting periods, the peaks at the end of the resting periods were optimal, as explained in section 3.2.

The optimal conditions for fat production (φ_F) were varied f. If $f = 5.0$, the value of risk did not depend on φ_F so much (Fig. B(i)), and increasing f, the optimal conditions became dependent on φ_F (Fig. B(ii, iii)), since fat had a greater impact on the energy level, and the production phase became more important with increasing f. The φ_F minimum risk was achieved at the end of the active periods when $f = 5$ (Fig. B(i)), but the optimal φ_F was shifted to the end of the resting period when $f = 10.6$

and $f = 15.0$ (Fig. B(ii, iii)).

As discussed in section 3.1, fat can compensate for the lack of glucose at the end of the resting periods when the efficiency of fat as an energy resource is large enough (e.g. $f = 10.6$ and $f = 15.0$). Thus, producing fat at the end of the resting period can be an optimal strategy. However, when f is small ($f = 5.0$), the fat is unable to overcome the lack of glucose and energy depletion tends to occur when either fat or glucose is at a low level. Therefore, synchronized production of both fat and glycogen was a better strategy than shifted production timing.

Appendix C

Circadian oscillation is necessary to maintain robust peak phases of substances against timings of food intakes

The equilibria of the model (Eq. 1, 5, and 6) can be derived by calculating x_G^*, x_F^*, and x_L^* that satisfy $\dot{x_G} = \dot{x_F} = \dot{x_L} = 0$, as follows:

$$x_G^* = \frac{aL(t)}{\overline{\gamma_F} + d_G}, x_F^* = \frac{\overline{\gamma_F}}{d_F}\frac{aL(t)}{\overline{\gamma_F} + d_G}, x_L^* = \frac{\overline{\gamma_L}}{\overline{\gamma_\beta}}\frac{aL(t)}{\overline{\gamma_F} + d_G}, \quad (C1)$$

where circadian oscillation is not considered, $\overline{\gamma_F}$, $\overline{\gamma_L}$, and $\overline{\gamma_\beta}$ can be assumed as constant values. The equilibria change in response to $L(t)$, represented in Eq. (2a) and (2b), d_G and d_F are represented in Eq. (3a) and (3b), respectively. There are two equilibria corresponding to the feeding ($L(t) = 1$) and fasting ($L(t) = 0$) periods as follows:

$$x_G^* = x_F^* = x_L^* = 0, \qquad where\ L(t) = 0\ (i.e.\ fasting\ period), \quad (C2)$$

and

$$x_G^* = \frac{a}{\overline{\gamma_F} + d_G}, x_F^* = \frac{\overline{\gamma_F}}{d_F}\frac{a}{\overline{\gamma_F} + d_G}, x_L^* = \frac{\overline{\gamma_L}}{\overline{\gamma_\beta}}\frac{a}{\overline{\gamma_F} + d_G}, where\ L(t) = 1\ (i.e.\ feeding\ period). \quad (C3)$$

Without the circadian oscillation of γ_F, γ_L, and γ_β, the peak time of x_G, x_F, and x_L in the two schedules were shifted by 12 h (lower row in Fig. C), and the timings of the food intakes were directly reflected in the peak times of glucose, fat, and glycogen. In contrast, the peak phases did not dramatically shift depending on the two feeding schedules when the circadian oscillation was considered, where $\varphi_F = 6, \varphi_L = 18$ (upper row in Fig. C). Considering the circadian regulation of the production rates, the peak

times of glucose, fat, and glycogen were robust to changes of the timing of food intake. Circadian regulation on the production rates also contributed to reduction of the risks of energy depletion and hyperglycemia. With the production rates fixed at the mean values of the maximum and minimum levels ($\gamma_F = 0.11$, $\gamma_L = 1.025$, and $\gamma_\beta = 0.25$), the risks of energy depletion and high glucose level were 289.90 and 369.60, respectively, which were larger than the minimum risks under the optimal phase conditions: 35.33 at $(\varphi_F, \varphi_L) = (11,22)$ and 255.29 at $(\varphi_F, \varphi_L) = (18,1)$.

Tables

Table 1. Fixed parameter values in the calculations

Description	Symbol	Value
Efficiency of obtaining glucose from food intake	a	5.0
Maximum rate of triglyceride production	a_F	0.17
Minimum rate of triglyceride production	b_F	0.05
Maximum rate of glycogenesis	a_L	2.0
Minimum rate of glycogenesis	b_L	0.05
Maximum rate of glycogenolysis	a_β	0.5
Minimum rate of glycogenolysis	b_β	0
Peak time of glycogenolysis	φ_β	6.0
Time period	τ	24.0
Glucose consumption rate in the active period	d_{GA}	1.0
Fat consumption rate in the active period	d_{FA}	0.5
Relative glucose/fat consumption rate in the resting period	α	0.8

Figures

Figure 1

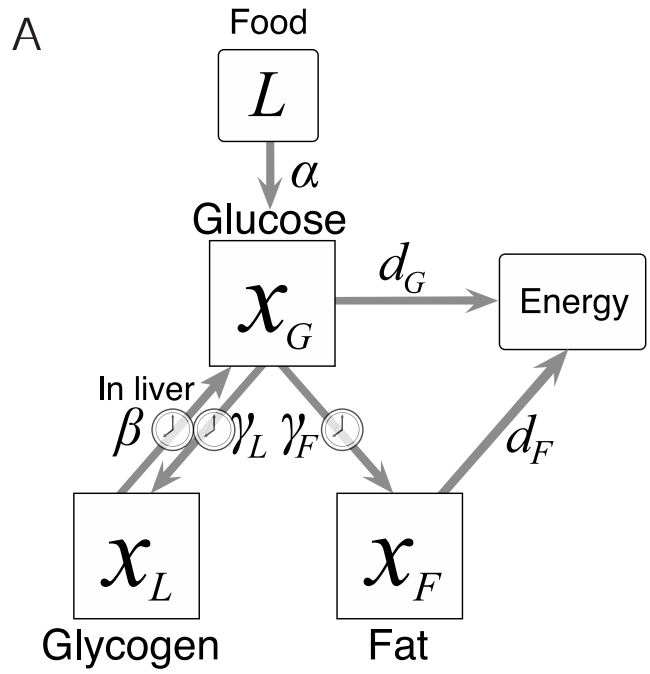

Glucose allocation model. The amount of glucose, glycogen, and fat are represented by x_G, x_L, and x_F. Glucose is obtained at the rate of α $L(t)$ food intake depending on the food schedules described in Fig. 1B. Glucose is allocated into glycogen and fat at rates of γ_L and γ_F, respectively. Glycogen is degraded into a glycose at the rate of γ_β. Glucose and fat are consumed as energy resources at the rates of d_G and d_F, respectively. d_G is high during the active period and low during the resting period (Eq. 3). γ_L, γ_F, and γ_β are regulated by the circadian clock and represented by the cosine curves in Eq. 4.

Figure 1

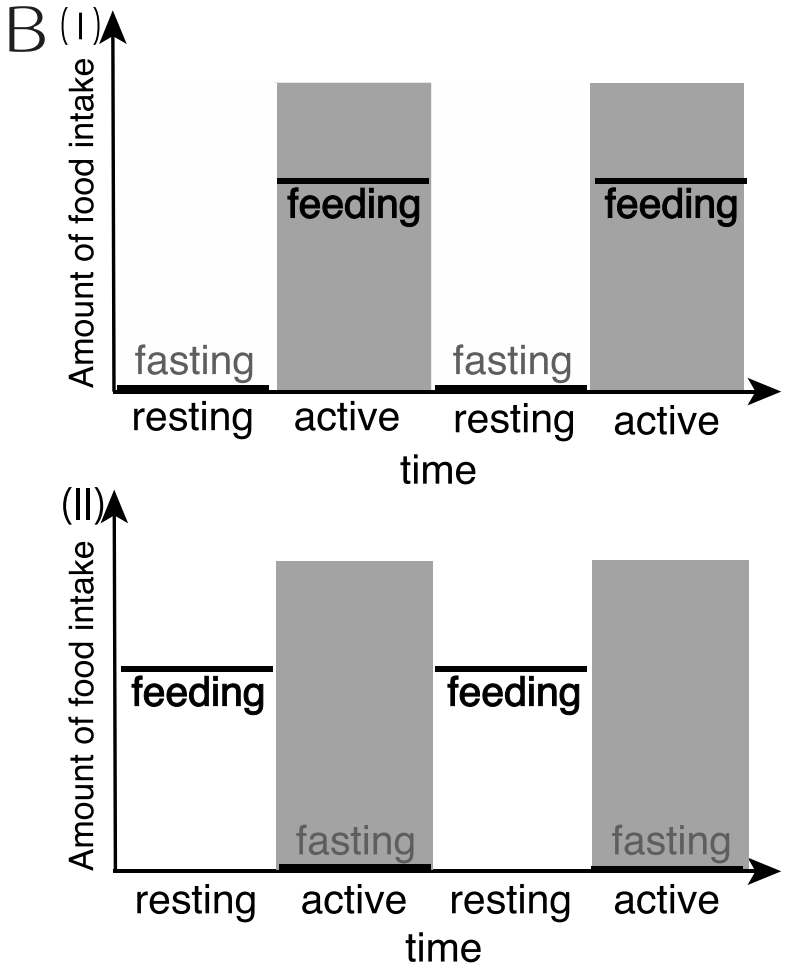

Two schedules of food intakes. (I) *Synchronized food schedule*. The active periods and feeding periods are synchronized. We assume that this schedule is natural for mammals, assuming that most mammals obtain food during the active periods. (II) *Desynchronized food schedule*. The active periods and feeding periods are desynchronized. This schedule is assumed to be abnormal habits and similar to the situation of shift workers.

Figure 2

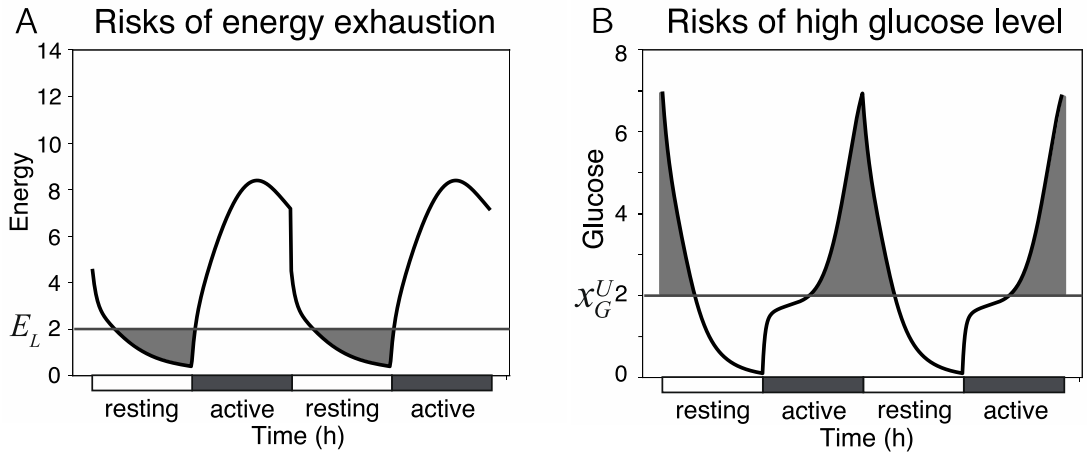

Two types of risks for nutrient homeostasis. We consider the risks of (A) high glucose level and (B) energy exhaustion as possible elements behind the nutrient homeostasis. The white and black bars on the time axis represent resting and active periods, respectively. (A) *The risks of energy exhaustion.* The damages of energy exhaustion occur when the $E(t)$ is below the threshold $E_L = 4.0$. The risks of energy exhaustion are calculated as the integrated value of $E_L - E^*$ (Eq. 9a) and represented as the grey area. (B) *The risks of high glucose level.* The damages occur when the glucose level exceeds the threshold $x_G^U = 2.0$. The integrated value of the damage $(x_G(t) - x_G^U)$ is calculated as the risks of high glucose level, described as grey area (Eq. 9b).

Figure 3

(A, E) *Risks for nutrient homeostasis.* We calculated two possible risks for nutrient homeostasis based on Eq. (9b) and (9c) for $24 \times 24 = 576$ combinations of (φ_F, φ_L). The light-colored cells represent the higher level of risks, as shown in the scales next to the heat maps. Here, we search for the condition of (φ_F, φ_L) that realizes a low risk. The condition that achieved the lowest risk is highlighted by a white frame. The white and black bars along the axis represent the resting and active time, respectively.

(B, D, F) *Daily patterns of variables representing metabolic profiles.* The bold lines show the dynamics of each valuable for two periods for 16 combinations of (φ_F, φ_L) ($\varphi_F = 0, 6, 12, 18$ and $\varphi_L = 0, 6, 12, 18$). The white and black bars in the vertical axis represent the resting and active periods, respectively.

(C, G) *The level of risk for nutrient homeostasis.* The values of the risks of energy exhaustion and hyperglycemia shown in (A) and (E) corresponding to each of the 16 phase combinations in (B, D, F) ($\varphi_F = 0, 6, 12, 18$ and $\varphi_L = 0, 6, 12, 18$).

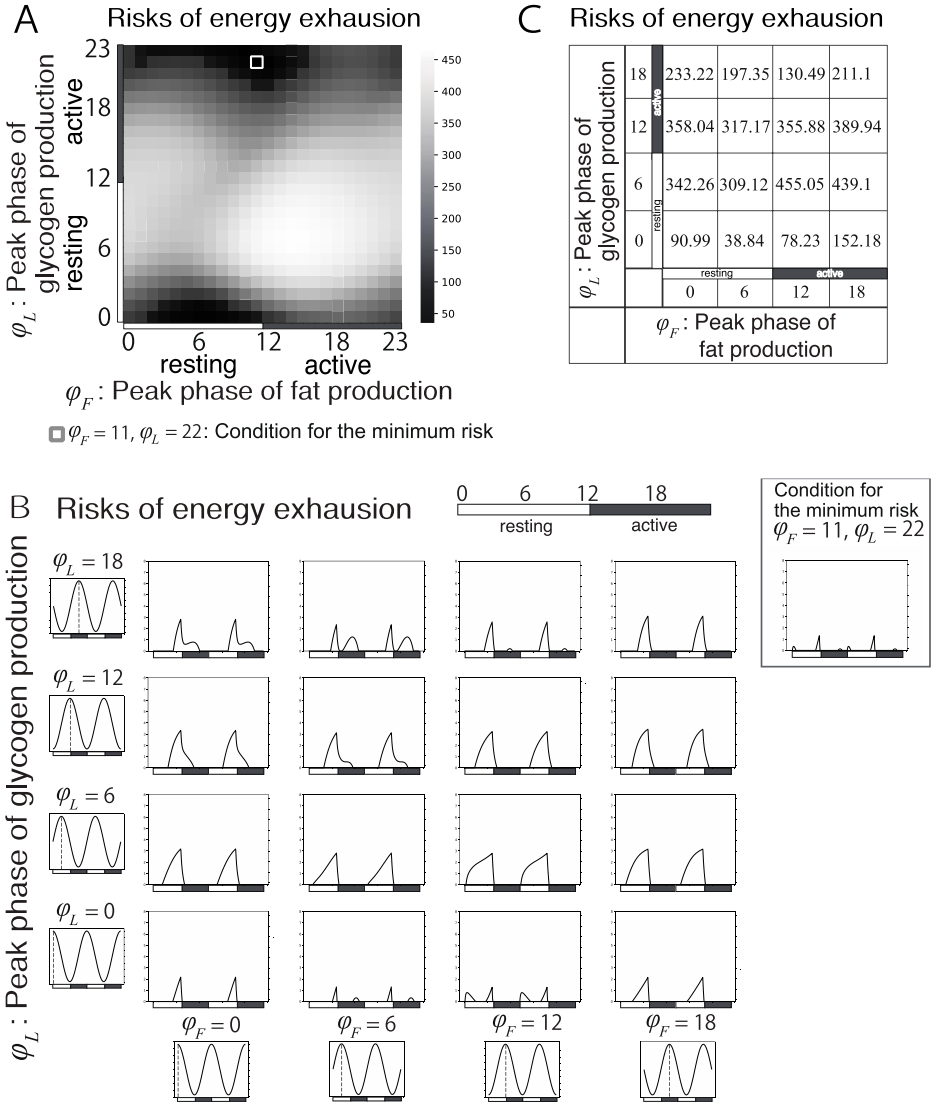

(A) *Risk of energy exhaustion.* Low risks (dark-colored cells) are achieved φ_F during the resting period and at the beginning of the active period and φ_L during the active period. The lowest risk is at $(\varphi_F, \varphi_L) = (11, 22)$. (B) *The levels of energy exhaustion.* The bold solid lines show the time series of energy level below the threshold ($\max\{(E_L - E(t)), 0\}$). The case in the condition for the minimum risk $(\varphi_F, \varphi_L) = (11, 22)$ is represented in the upper right side. (C) *Values of level of energy exhaustion.* The values correspond to the level of energy exhaustion shown in (A) for each (φ_F, φ_L).

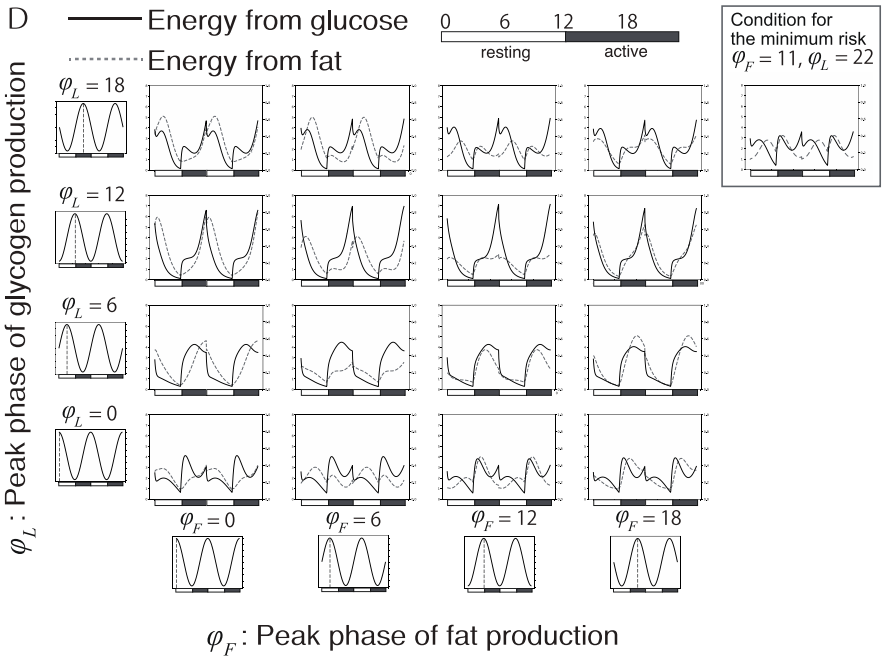

(D) *The energy levels obtained from the two resources.* The solid and dotted lines show the energy obtained from fat ($d_F x_F$) and glucose ($d_G x_G$), respectively. The case in the condition for the minimum risk $(\varphi_F, \varphi_L) = (11, 22)$ is represented in the upper right side.

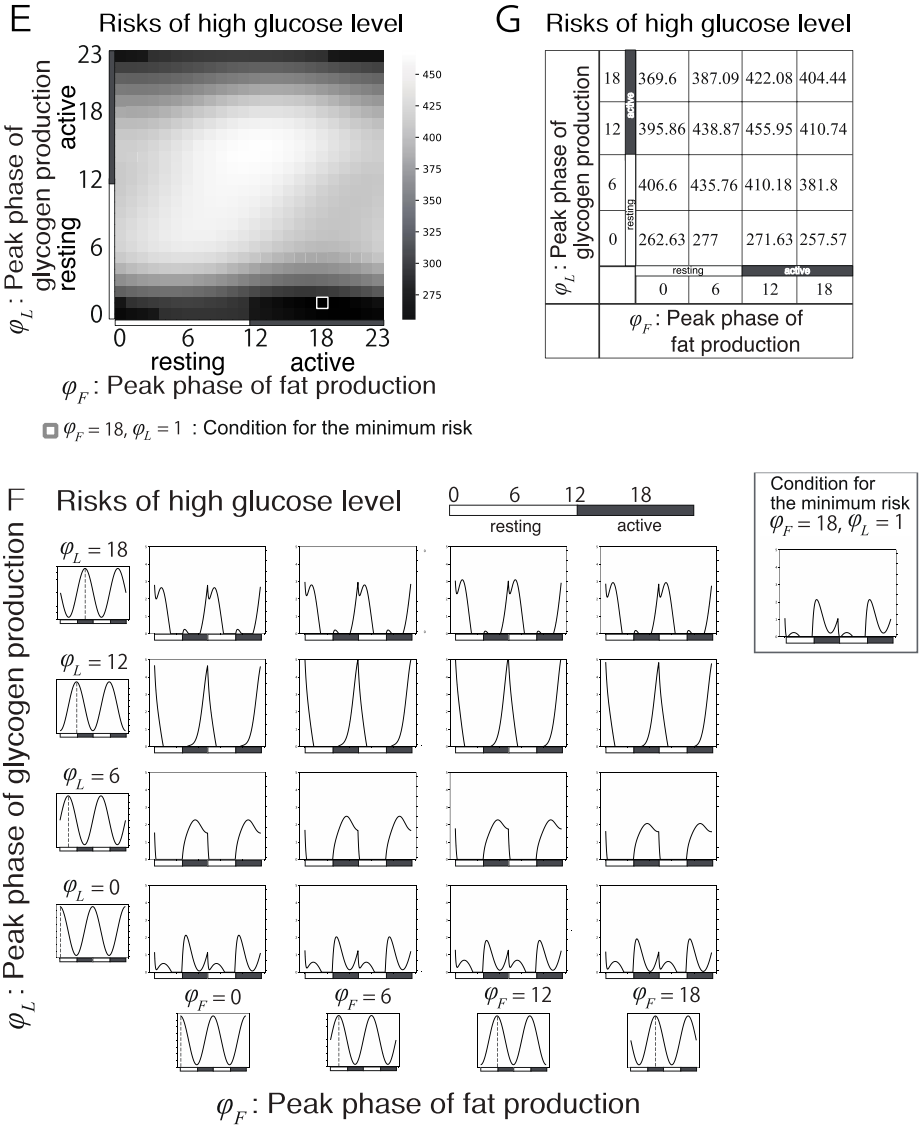

(E) *The risk of hyperglycemia.* A low risk was achieved φ_F during the active period. The lowest risk was achieved at $(\varphi_F, \varphi_L) = (18, 1)$. (F) *Levels of excess glucose.* The solid lines show the level of glucose that exceeds the threshold of damage ($\max\{(x_G(t) - x_G^U), 0\}$). The case in the condition for the minimum risk $(\varphi_F, \varphi_L) = (18, 1)$ is represented at the upper right side. (G) *The level of hyperglycemia.* The values correspond to the level of energy exhaustion shown in (A) for each (φ_F, φ_L).

Figure 4

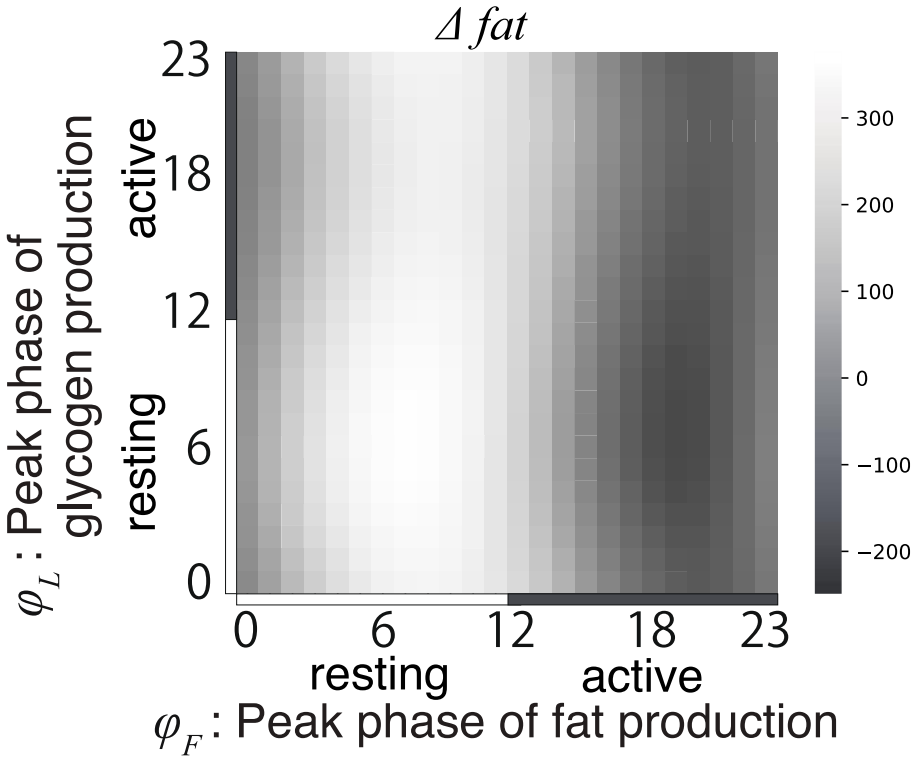

Difference in fat accumulation between food intake in the resting period and active period. Δfat, the integrated difference of fat between desynchronized and synchronized schedule (Eq. 8), is calculated for each combination of (φ_F, φ_L). The white and black bars below the axis represent the resting and active periods. The scale next to the heat map denotes the value of Δfat. In the heat map, the light-colored cells correspond to the condition of higher Δfat, which suggests that fat is more likely to accumulate under the desynchronized food schedule conditions. The higher Δfat is observed when φ_F is in the resting period and at the beginning of active period.

Figure A

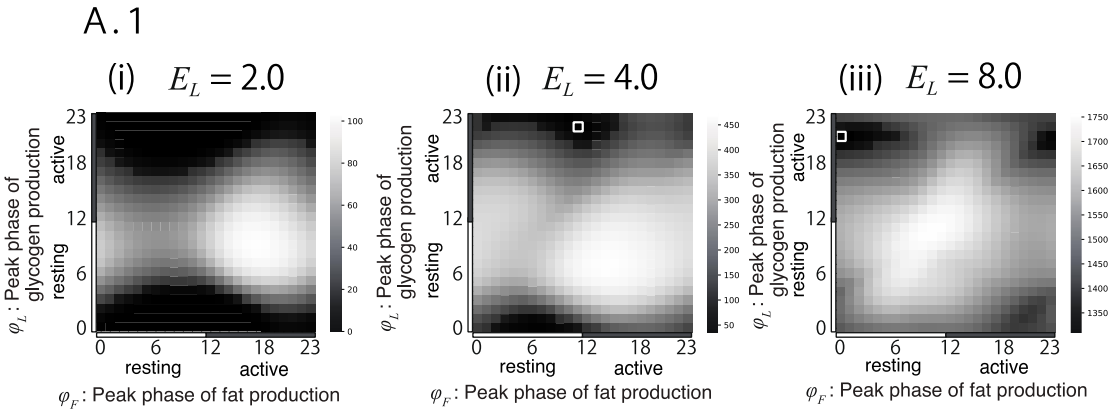

Threshold dependences of risks of energy exhaustion and excess glucose levels. We calculated two possible risks, denoted by Eq. (9b) and (9c) for $24 \times 24 = 576$ combinations of (φ_F, φ_L). The light-colored cells represent a higher level of risk, as shown in the scales. The condition achieved the lowest risk in the white frames. The white and black bars along the axis represent the resting and active times, respectively. (A.1) *Risk of energy exhaustion.* (i) $E_L = 1.0$. The risks become zero in the multiple conditions represented by the black area. (ii) $E_L = 2.0$. The lowest risk is achieved at $(\varphi_F, \varphi_L) = (9, 23)$. (iii) $E_L = 4.0$. The lowest risk is achieved at $(\varphi_F, \varphi_L) = (1,0)$.

A.2

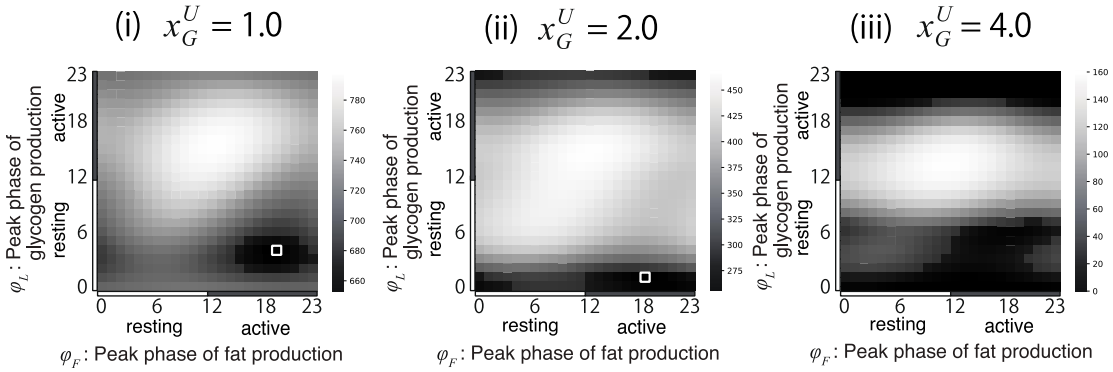

(A.2) *The risk of hyperglycemia.* (i) $x_G^U = 1.0$. The lowest risk is achieved at $(\varphi_F, \varphi_L) = (19,3)$. (ii) $x_G^U = 2.0$. The lowest risk is achieved at $(\varphi_F, \varphi_L) = (19, 0)$. (iii) $x_G^U = 4.0$. The risks become zero in the black area.

Figure B

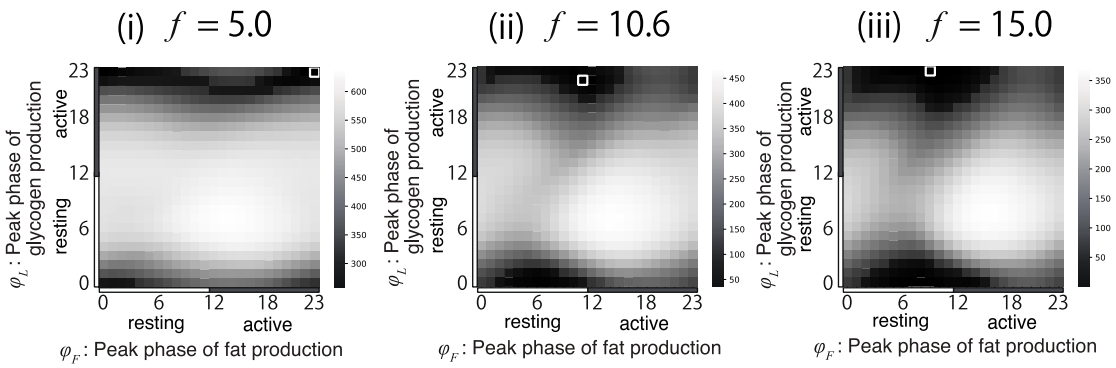

Relative ATP production efficiency depends on the risk of energy depletion. We calculated the risks of energy depletion, denoted by Eq. (8a) for $24 \times 24 = 576$ combinations of (φ_F, φ_L) changing the relative ATP production efficiency (f). The light-colored cells represent a higher level of risk, as shown in the scales. The condition achieved the lowest risk in the white frames. The white and black bars along the axis represent the resting and active times, respectively. (i) $f = 5.0$. The lowest risk is achieved at $(\varphi_F, \varphi_L) = (23, 23)$. (ii) $f = 10.6$.The lowest risk is achieved at $(\varphi_F, \varphi_L) = (11, 22)$. (iii) $f = 15.0$. The lowest risk is achieved at $(\varphi_F, \varphi_L) = (9,23)$.

Figure C

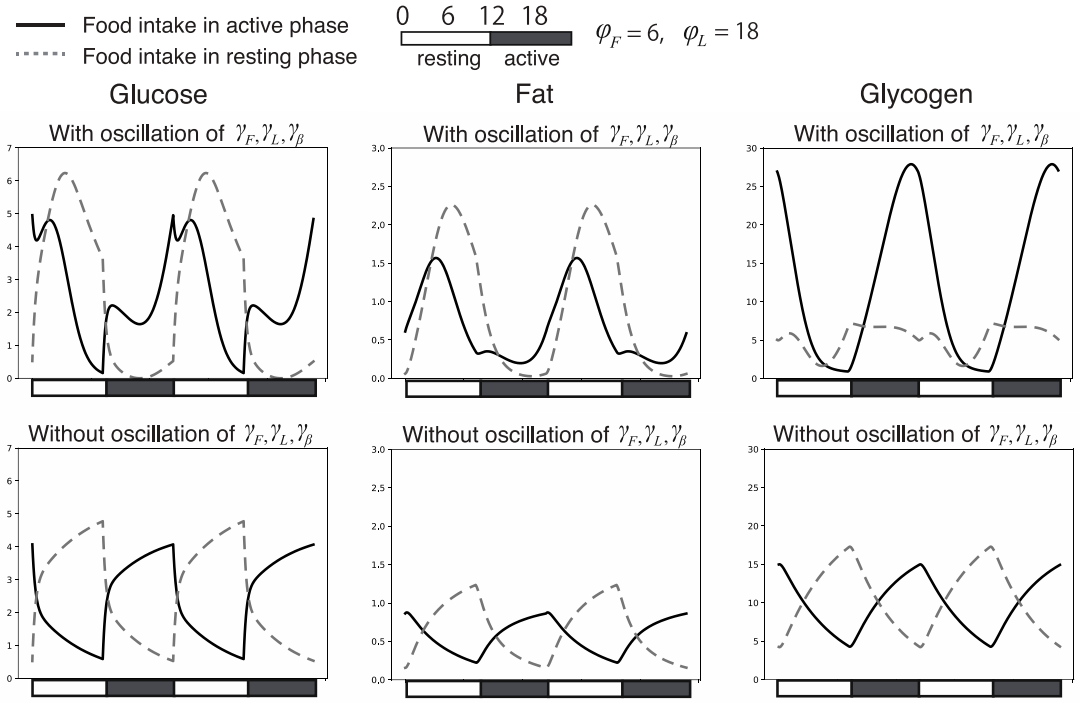

Daily patterns of variables with and without circadian oscillation of γ_L, γ_F, *and* γ_β. Upper row: dynamics of glucose, fat, and glycogen with circadian oscillation, where $\varphi_F = 6$ and $\varphi_L = 18$. Lower row: dynamics without circadian oscillation, where the production rate of fat, glycogen, and glycogenolysis are fixed at the mean values of the maximum and minimum levels of the production rates ($\gamma_F = 0.11$, $\gamma_L = 1.025$, and $\gamma_\beta = 0.25$; the maximum and minimum levels are shown in Table 1). The white and black bars along the axis represent the resting and active periods, respectively. The bold and dotted lines show the dynamics of food intake in the active period and in the resting period, respectively.